

UNIVERSITA' DEGLI STUDI DI BOLOGNA

FACOLTA' DI SCIENZE MATEMATICHE
FISICHE NATURALI

Dottorato di Ricerca in Geofisica - XVII ciclo

***THE MECHANICS OF SEISMIC SOURCE:
DYNAMICALLY CONSISTENT MODELS OF
EARTHQUAKE RUPTURE***

Ph.D. Thesis of:

Elisa Tinti

Tutor: Dr.

Massimo Cocco

Relator: Dr.

Maria Elina Belardinelli

Coordinator: Prof.

Maurizio Bonafede

March 2005

*A babbo Giovanni e
a mamma Carolina*

Contents

Introduction

Part I: Dynamic modeling of extended seismic source

1-Theoretical 2D dynamic modeling of seismic source	
1.1 Introduction	1
1.2 Theoretical source representation	2
1.2.1 Kinematic and dynamic source models	3
1.3 Dynamic modeling	4
1.3.1 Constitutive laws	7
1.4 Methodology	9
1.5 Slip weakening in the R&S formulation	10
1.5.1 The cohesive zone	14
2. Physical interpretation of the breakdown process using R&S constitutive laws	
2.1 The evolution law and the dynamic rupture growth	24
2.2. The direct effect of friction	26
2.3. The evolution law and the healing mechanisms	29
2.4. Discussions	36
3. Heterogeneous faults modelled with R&S law	
3.1 The velocity-weakening frictional regime	40
3.1.1 Strong velocity-weakening fault	41
3.1.2 Weak velocity-weakening fault	44
3.2 Numerical representation if frictional heterogeneities	45
3.2.1 Heterogeneous distribution of the L parameter	46
3.2.2 Heterogeneous distribution of the (B-A) parameter	51
3.3 Implications for slip duration	53
3.4 Implications for fracture energy	54
3.5 Conclusive remarks	56
4. Estimates of slip weakening distance for different dynamic rupture models	
4.1 Simulations with a slip weakening law	60
4.2 Simulations with rate and state laws	62
4.2.1 The direct effect of friction	62
4.2.2 Friction behavior at high slip rates	64
4.3 Conclusive remarks	65

Part II: Link between dynamic and kinematic representations of earthquake rupture

5. Inference of dynamic parameters from kinematic models	
5.1 Background	69
5.2 Methodology	71
5.3 Dependence of traction evolution on earthquake source time function adopted in kinematic rupture models	72
5.3.1 Adopted source time functions	72
5.3.2 Simulations with a uniform slip model	74
5.3.3 Simulations with a heterogeneous slip model	77
5.3.4 Discussion	79
5.4 A kinematic source time function compatible with earthquake dynamics	80
5.4.1 Analytical form if the new kinematic source time function	83
5.4.2 Parameterization of source time function	86
5.4.3 Kinematic relations	87
5.4.4 Deriving dynamic rupture parameters from kinematic models	90
5.4.5 Relation between kinematic and dynamic source parameters	93
5.4.6 Discussions	97
6. Earthquake fracture energy inferred from kinematic rupture models on extended faults.	
6.1. Introduction	101
6.2 Methodology	103
6.2.1 Computation method	103
6.2.2 Interpolation and Smoothing	104
6.3. Kinematic Models	108
6.4. Breakdown work estimates	115
6.5. The choice of the initial stress	118
6.6. Results	120
6.6.1 The inferred constitutive behavior	120
6.6.2 Breakdown work density distributions	126
6.7. Scaling relations between W_b and kinematic parameters	130
6.8. Discussion	138
6.9. Conclusive remarks	141
Conclusions	143
Appendix	149
References	153

Introduction

A seismic event is associated to a fracture propagation on the earth crust and is an effect of a local instability of the slowly and continuously tectonic deformation process. This sudden instability causes a displacement of two adjacent volumes, called faults. When the maximum tectonic stress is reached, the stored elastic energy is rapidly released causing fracture propagation (i.e., dislocation). The resulting motion on the fault is related to a drop in shear stress. Tectonic strain can be divided into elastic and nonelastic components. No potential energy is associated with nonelastic strain. Consequently, an earthquake occurs as a result of elastic strain drop. The potential energy is dissipated on heat, radiated through elastic waves and spent to create the fracture. That is, the elastic component of strain is transformed on plastic component. In terms of crustal deformation the storage and release of stress can be described through four phases: pre-seismic, co-seismic, post-seismic and inter-seismic. The co-seismic phase, containing the seismic event, is characterised by high rupture velocity and seismic waves emission. One of the major goals of the seismology is to study the stress condition on the active fault before, during and after an earthquake rupture.

The dynamic description of seismic source originates from the mechanic fracture theory. It describes the seismic source with a propagating shear fracture that radiates seismic waves caused by an initial stress field. The earth is considered a continuum and elastic medium holding fault surfaces. The displacement on the fault is the solution of the fundamental elastodynamic equation. Others equations, setting up the conditions of instability and the evolution of the dynamic traction during the rupture on the fault plane, are implemented to solve the dynamic problem. In the literature these equations are called *constitutive laws*. By means of constitutive laws it is possible to describe the whole duration of co-seismic phase. The co-seismic phase of a fault seismic cycle is described with three distinct parts: nucleation, propagation and arrest. The nucleation phase contains all mechanisms foregoing the release of seismic energy (pre-seismic); the dynamic propagation phase is characterized by the emission of seismic waves and high rupture velocity on the fault plane and, finally, the arrest

phase determines the end of the rupture process (i.e., the end of the co-seismic phase) and it is locally described with the healing phase (that is, the local duration of the dislocation). One of the basic unresolved issues of earthquake dynamics is the duration of particle displacement at each point on a finite fault. Indeed it is still an important task to distinguish between different slip models characterized by a crack-like rupture growth in which the local duration is similar to the total duration of the seismic event or by a propagating slip pulse in which the local duration is shorter than the total duration of the rupture.

My work (in collaboration with other researchers of INGV- Rome, USGS-Menlo Park and NIED-Tzukuba) is focused on the dynamic modelling of the coseismic process. In this description the dislocation is caused by the drop of the stress after it has reached the maximum static strength of the fault. The release of the dynamic stress occurs on a zone located close the rupture front (just behind the front) and is called *breakdown zone* or *cohesive zone*. This zone is responsible of fracture energy absorption, radiated seismic energy and slip acceleration.

In the context of this study, earthquakes are considered as instabilities of a complex dynamic system governed by assigned frictional laws (constitutive laws). We address the study of constitutive response of fault materials (i.e., the dynamics of earthquake rupture) into necessarily simplified computational models. Besides, most of the dynamic problems in fracture mechanics proved to be unsolvable analytically by means of classical methods: The equations governing the rupture dynamics have to be treated numerically. In the present work we use the finite difference numerical technique (in 2-D as well as 3D dimension).

In the first chapter we review the theoretical modeling of a dynamic rupture propagation governed by friction processes. We introduce two of the most commonly used constitutive laws in the literature: slip weakening law and rate and state law. We present the analytical expressions of these frictions laws and we discuss the different competing physical mechanisms which contribute to dynamic fault weakening during earthquakes. In particular, we describe the dynamic

traction and the slip velocity evolution within the cohesive zone during a 2-D in-plane dynamic rupture using rate and state dependent constitutive laws.

In the second chapter we show how the rate and state constitutive laws allow a quantitative description of the dynamic rupture growth. These modeling results help understanding the physical interpretation of the breakdown process and the weakening mechanisms. We compare the time histories of slip velocity, state variable and total dynamic traction to investigate the temporal evolution of slip acceleration and stress drop during the breakdown time. Because the adopted analytical expression for the state variable evolution controls the slip velocity time histories, we test different evolution laws to investigate slip duration and the healing mechanisms. We will discuss how the direct effect of friction and the friction behavior at high slip rates affect the weakening and healing mechanisms.

In the third chapter we investigate the effects of non-uniform distribution of constitutive parameters of rate and state laws on the 2D dynamic rupture propagations. We use the characterization of different frictional regimes proposed by Boatwright and Cocco (1996), which is based on different values of the constitutive parameters a , b and L (these are the parameters defining rate and state constitutive laws). The results involve interesting implications for slip duration and fracture energy.

In the fourth chapter we check the possibility to constrain and to estimate the critical slip weakening distance from slip velocity functions, following a recent idea of Mikumo et al. (2003). Because of the poor knowledge of the scaling relation between dynamic parameters inferred from laboratory experiments and from real faults, it is still open to debate the actual dimensions of physical parameters characterizing the seismic source. Particularly, the range of real D_c values is still unknown. We model the dynamic propagation of a 2-D in-plane crack obeying to either slip weakening (SW) or rate- and state-dependent friction laws (R&S). Therefore we compare the value of slip weakening distance (D_c), adopted or estimated from the traction versus slip curves, with the critical slip distance measured as the slip at the time of peak slip velocity (D_c').

In the fifth chapter we compute the temporal evolution of traction by solving the elasto-dynamic equation and by using the slip velocity history as a

boundary condition on the fault plane. We employ a 3D finite difference algorithm. In this chapter we do not consider a fully dynamic model because we do not assume any constitutive law, but we infer the dynamic parameters and the traction evolution from kinematic models. We use different source time functions to derive a suite of kinematic source models to image the spatial distribution of dynamic and breakdown stress drop, strength excess and critical slip weakening distance (D_c). Therefore we compare the inferred dynamic parameters trying to answer the following questions: Can we constrain the actual values of fundamental dynamic parameters from kinematic models? If the kinematic slip velocity histories affect the inferred dynamic parameters, is it still possible to constrain the dynamic source parameters of real earthquakes?

We suggest that source time functions compatible with earthquake dynamics have to be used to infer the traction time history. For this reason, we propose a new source time function to be used in kinematic modelling of ground motion time histories, which is consistent with dynamic propagation of earthquake ruptures and makes feasible the dynamic interpretation of kinematic slip models. This function is derived from a source time function first proposed by Yoffe (1951), which yields a traction evolution showing a slip-weakening behavior. In order to remove its singularity we apply a convolution with a triangular function and obtain a regularized source time function called "regularized *Yoffe*" function. Using this analytical function we examine the relation between kinematic parameters, such as peak slip velocities and slip duration, and dynamic parameters, such as slip weakening distance and breakdown stress drop.

In the sixth chapter we estimate fracture energy on extended faults for several recent earthquakes (having moment magnitudes between 5.6 and 7.2) by retrieving dynamic traction evolution at each point on the fault plane from slip history imaged by inverting ground motion waveforms. We define the breakdown work (W_b) as the excess of work over some minimum traction level achieved during slip. W_b is equivalent to "seismological" fracture energy (G) in previous investigations. We employ a 3-D finite difference algorithm to compute the dynamic traction evolution in the time domain during the earthquake rupture. We estimate W_b by calculating the scalar product between dynamic traction and slip

Introduction

velocity vectors. Finally we compare our inferred values with geologic surface energies.

The contents of this Ph.D. Thesis have been recently published (or submitted) in the following papers:

Cocco M., A. Bizzarri, E. Tinti, 2004, Physical interpretation of the breakdown process using a rate- and state-dependent friction law, *Tectonophys. “ Physics of Active Faults “*, 378, 241–262

Piatanesi, A., E. Tinti, M. Cocco and E. Fukuyama, 2004, The dependence of traction evolution on the earthquake source time function adopted in kinematic rupture models, *Geophys. Res. Lett.*, 31, doi:10.1029/2003GL019225.

Tinti, E., A. Bizzarri, A. Piatanesi, and M. Cocco, 2004, Estimates of slip weakening distance for different dynamic rupture models, *Geophys. Res. Lett.*, 31, L02611, doi: 10.1029 / 2003GL018811

Tinti E., A. Bizzarri, and M. Cocco, 2005, Modeling the dynamic rupture propagation on heterogeneous faults with rate- and state- dependent friction, submitted to *Annals of Geophys.*

Tinti, E., E. Fukuyama, A. Piatanesi and M. Cocco, 2005, A kinematic source time function compatible with earthquake dynamics, submitted to *Seismol. Soc. Am. Bull.*

Tinti E., P. Spudich, M. Cocco 2005, Earthquake fracture energy inferred from kinematic rupture models, submitted to *J. Geophys. Res.*

Part I:

Dynamic modeling of extended seismic source

Chapter 1

Theoretical 2D dynamic modeling of seismic source

1.1 Introduction

Earthquake source dynamics provides basis for understanding the physics of earthquake initiation, propagation and arrest. Seismic source theory assumes that the earth is an elastic and continuum medium containing several fractures. These fractures (called fault planes) are surfaces of weakness where the elastic conditions have been overcome (failure of Hooke's law) and which some previous displacement has occurred.

The stress rises in the source region due to tectonic processes: consequently, the capacity of frictional stress to resist the growing shearing stress might be exceeded. This is the critical condition that has to be satisfied to nucleate an earthquake and cause a releasing of accumulated strain energy. Most of the rocks in the first 10 kilometers of the lithosphere have brittle reology due to temperature and pressure conditions, i.e. they have frictional behavior.

A seismic event occurs as a propagating fracture in a continuum medium or as a relative sliding of surfaces that have already broken in the past. In particular, the pre-existing fault surfaces could fail rather than another unbroken surface, because the faults are relatively weak. Therefore, fault mechanics is governed by friction processes.

In order to formulate laws governing fracture propagation at the earthquake source, it is necessary to consider the mechanics of brittle fracture. The material surrounding the fracture surface remains linearly elastic. This assumption implies that the inelastic zone is sufficiently small to be considered physically infinitesimal and to be incorporated into the fracture surface. Anyway, many recent geological

investigations have shown the complexity of the region bordering the slipping zone and the significant thickness of the seismogenic zone. This assumption can affect the way the failure actually takes place. The definition of fault zone model and the understanding of the dominant physical processes during dynamic rupture are extremely important tasks of the current scientific research.

1.2 Theoretical source representation

The description of fault mechanics is based on the solution of the fundamental elasto-dynamic equation derived from classical Newtonian representation. This fundamental equation, underlying the theory of seismology, relates forces in the medium to measurable displacements. It is inferred from the *Second Law* of dynamic for continuum media:

$$\rho \ddot{u}_i = f_i + \sigma_{ij,j} \quad (1.1)$$

coupled with the linear elastic relation for isotropic elastic medium:

$$\sigma_{ij} = \lambda e_{kk} \delta_{ij} + 2\mu e_{ij} \quad (1.2)$$

In equation (1.1) ρ is the density of the solid body, u_i are the components of the displacement field that describe the deformation of the body, f_i is the i -component of the applied external body force density acting per unit volume, \ddot{u}_i is the second time derivative of the displacement, and σ_{ij} the component of the stress tensor; in equation (1.2) λ and μ are the Lamé constants, δ_{ij} is the dimensionless Kronecker delta function and e_{ij} is the component of the strain tensor. In the equation (1.1) the Einstein summation convention is assumed. The equation (1.2) is valid when the elastic properties are independent of the orientation in the body (i.e., isotropic medium).

The representation theorem defines the elastic displacement (solution of equations 1.1 and 1.2) inside a volume V with surface S due to the sum of three double integrals over space and time functions (see equation 2.41 of Aki and Richard, 2002). The first constituent is a volume integral over body forces multiplied by the Green's function of the system; the second and the third are surface integrals:

over stress times the Green's function minus the displacements times derivatives of the Green's. The Green function is the solution of the equation of motion (1.1) for special impulsive single point forces, termed *Dirac*, which act inside the body.

The representation theorem can be a powerful aid in seismic source theory if the surface S (i.e. the surface of the Earth) is chosen to include an internal surface Σ across which discontinuities may arise (the displacements on the Σ^+ side of Σ and on the Σ^- side are different). The equation motion is still satisfied throughout the interior of the surface $S+\Sigma^+ +\Sigma^-$ (Aki and Richard, 2002). Assuming on the S surface that u and G satisfy the same homogeneous boundary conditions, the integral equation results:

$$u_i(x, t) = \int d\tau \int_V G_{in} f_i dV + \int d\tau \int_{\Sigma} [C_{ijkl} G_{nk,l} u_i n_j] dS - \int d\tau \int_{\Sigma} [G_{ni} T_i] dS \quad (1.3)$$

where the square brackets are used for the difference between values of the functions on Σ^+ and Σ^- . In equation (1.3) G_{in} is the Green tensor, C_{ijkl} the moduli tensor of elastic deformation, T_i traction and n_j the unit normal to dislocation surface Σ . The solution of (1.3) gives the displacement caused by the dislocation on the fault plane. For the uniqueness of the equations' system, initial and boundary conditions on Σ are necessary.

1.2.1 Kinematic and dynamic source models

The most widely used models are dislocation models in which the earthquake is conceived of a displacement discontinuity along a fault plane. This representation defines a *kinematic source model*, in which the deformations on the earth are derived from a given/known/assumed slip vector that represents the inelastic displacement of the two sides of a fault. Using as boundary conditions the continuity of traction and the discontinuity of displacement on the fault surface, the equation (1.3) results:

$$u_i(x, t) = \int d\tau \int_{\Sigma} C_{jkpq} G_{ip,q} \Delta u_j n_k dS \quad (1.4)$$

where Δu_j represents the discontinuity of the displacement on the fault plane. The slip vector Δu_j (i.e., the non-elastic displacement on the faults) is enough to determine displacement everywhere (i.e., the elastic displacement u_i). In a kinematic model the slip Δu_j is assumed to be known. The kinematic approach is very useful to

estimate source parameters and to interpret the observables. The set of kinematic source parameters are: seismic moment, fault dimension, displacement, rise time (which characterizes the time taken for the slip vector, at a particular point on the fault, to reach its final value) and rupture velocity on the fault plane. Anyway, this approach is inadequate for understanding the physical processes actually occurring on the source region.

On the contrary, the *dynamic source model* describes the seismic source as a propagating shear fracture due to an initial stress field. In the dynamic approach the dislocation is the consequence of the stress condition and the strength of the rocks on the seismogenic earth crust. Therefore, when the strength of material is exceeded, one can study the way in which the material failure nucleates and rapidly spreads.

Let σ_{ij}^0 be the initial stress tensor and σ_{ij}^p the dynamic stress perturbation due to the dynamic propagation of the crack. The integral solution of the dynamic problem [derived from equation (1.3)] is:

$$\mathbf{u}_n(\mathbf{x}_1, \mathbf{x}_2, \mathbf{t}) = \int_0^t d\tau \int_{\Sigma(\tau)} \mathbf{G}_{n\alpha} \sigma_{\alpha 3}^p dS \quad (1.5)$$

where $\Sigma(\tau)$ is the fractured region at $t=\tau$ and \mathbf{u}_n is the displacement on the fault plane. The solution is found exploiting the antisymmetries of the problem (Kostrov and Das, 1988).

The main assumption in the dynamic description of seismic source is that traction across the fault is related to slip at the same point through a friction law (because the elastic condition fails on the fault plane). Friction laws allow us to model the whole failure process, from the nucleation to the arrest of the fracture.

1.3 Dynamic modeling

The modeling of earthquake nucleation and the subsequent dynamic propagation requires the adoption of a fault constitutive law that controls the traction evolution and the slip acceleration and allows the absorption of finite fracture energy at the crack tip. A constitutive relation (*friction law*) represents the governing

equation of the failure process and specifies the dependence between the components of stress tensor and other physical variables.

A number of factors can control friction: temperature, slip rate, slip history, characteristic length of asperity contacts, fault gouge, fluid pressure... That is, different competing physical mechanisms contribute to dynamic fault weakening during earthquakes. In order to have a complete description of a fault zone we need to understand the spatial and temporal scale dependence of relevant physical processes. The scale dependence is extremely important because it allows us to establish a hierarchy to characterize where and when the different physical processes govern the crustal faulting (Rice and Cocco, 2005).

Several constitutive laws have been proposed in the literature. They can be grouped in two main classes: (1) slip-dependent and (2) rate- and state- dependent laws. The former, the slip weakening law (SW), is one of the simplest and most widely used constitutive equation. This law assumes that friction (i.e., total dynamic traction) is a function of slip only (Ida, 1972; Palmer and Rice, 1973; Andrews, 1976-a, b; Ohnaka and Yamashita, 1989). This constitutive relation is completely characterized by initial stress τ_o , yield stress τ_y , dynamic frictional stress τ_f , and slip-weakening distance D_c [see equation (1.8)]. In this model the fault begins to rupture when the yield stress is exceeded. As the slip grows to the critical slip-weakening distance D_c , the traction of the fault decreases to the dynamic frictional level. The strength excess, $\tau_y - \tau_o$, is the difference between the yield stress and the initial stress. The stress drop is $\tau_o - \tau_f$. Figure 1 shows all these dynamic parameters. Besides, the breakdown stress drop $\Delta\sigma_b$ is defined as difference between the yield stress and the frictional stress level. The slip weakening law involves a finite fracture energy G and prescribes the traction evolution within the cohesive zone (Barenblatt, 1959).

In the following of the thesis, we refer to the *cohesive zone* (or *breakdown zone*) as the zone of shear stress degradation near the tip of a propagating dynamic rupture front. The breakdown processes are those phenomena occurring within the cohesive zone responsible for the fracture energy absorption and the slip acceleration (see paragraph 1.5.1).

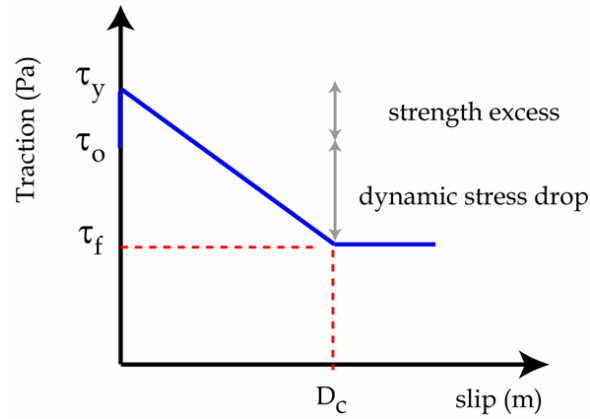


Figure 1: Graphic representation of the slip weakening law. The analytical expression is defined on Equation (1.8).

An alternative constitutive formulation, represented by the rate and state dependent (R&S) laws, considers that friction depends on slip velocity and state variable. The rate- and state- dependent friction laws (R&S) derived from laboratory experiments (Dieterich, 1979a, 1979b; Ruina, 1983) have been widely used in numerical simulations of earthquake ruptures, both at the laboratory scale (Bizzarri and Cocco, 2003 and reference therein) and for real-world faults (Guatteri et al., 2001; Guatteri et al., 2003). This class of constitutive relations includes an evolution law for the state variable that involves a friction dependence on time. Since R&S laws account for fault restrengthening after dynamic failure, they can be used to simulate repeated seismic events (Tse and Rice, 1986; Rice, 1993). Furthermore, they have been applied to model preseismic and postseismic processes, such as earthquake nucleation (Dieterich, 1992; Lapusta and Rice, 2002) and afterslip (Marone et al. 1991). These two constitutive formulations are alternative only for the description of the nucleation process (see Dieterich, 1992; Ohnaka and Shen, 1999), but they both provide a physically correct description (and very similar) of the dynamic crack propagation (see Okubo, 1989; Bizzarri et al., 2001). The main difference between these two constitutive laws is that SW prescribes the traction evolution with slip, whereas R&S do not and traction spontaneously evolves with time and/or slip driven by the state variable evolution (Cocco et al., 2004). However, even for the latter law it is possible to infer the slip weakening parameters (τ_o , τ_y , τ_f , D_c ; see paragraph 1.5.1). These parameters are essential to completely describe the cohesive zone and to compute the fracture energy. It has to be pointed out that R&S

laws have been derived from laboratory experiments at low slip velocity ($< 1\text{cm/s}$) and are usually assumed (as in the present study) to be valid also at high slip velocities ($\sim 1\text{m/s}$), such as those observed during large earthquakes. However, although the properties of the contact surface play a relevant role in controlling dynamic slip episodes, other mechanisms might affect fault friction at high slip velocity such as frictional heat (see Fialko, 2004, and references therein), thermal pressurization (see Andrews, 2002 and references therein) or mechanical lubrication (Brodsky and Kanamori, 2001).

1.3.1 Constitutive laws

The analytical expression of the R&S friction laws is, as explained earlier, composed by two equations: the strength law (governing law) and the evolution law. The formulation proposed by Dieterich (1986) and Ruina (1983) is the “slowness” or “ageing” law:

$$\tau = \left[\mu_* - a \ln\left(\frac{V}{V_*} + 1\right) + b \ln\left(\frac{\Phi V_*}{L} + 1\right) \right] \sigma_n^{eff} \quad (1.6)$$

$$\frac{d}{dt} \Phi = 1 - \frac{\Phi V}{L}$$

Another formulation, among different ones in the literature, is the R&S law with the “slip” evolution equation proposed by Beeler et al., (1994),

$$\tau = \left[\mu_* + a \ln\left(\frac{V}{V_*}\right) + b \ln\left(\frac{\Theta V_*}{L}\right) \right] \sigma_n^{eff} \quad (1.7)$$

$$\frac{d\Theta}{dt} = -\frac{\Theta V}{L} \ln\left(\frac{\Theta V}{L}\right)$$

The analytical expression of the classical slip weakening law (Andrews, 1976a, b) is:

$$\tau = \begin{cases} \tau_y - (\tau_y - \tau_f) \frac{u}{D_c} & u < D_c \\ \tau_f & u \geq D_c \end{cases} \quad (1.8)$$

In (1.6) and (1.7) V is the slip velocity, Φ and Θ are the state variables, μ_* and V_* are arbitrary reference values for the friction coefficient and for the slip velocity, respectively. a , b , L are the constitutive parameters: a represents an instantaneous rate sensitivity, that is the direct frictional response to a change in slip velocity, L is the characteristic length that together with b control the evolution of state variable toward the steady state. σ_n^{eff} is the effective normal stress; in the literature the parameters $A=a\sigma_n^{eff}$ and $B=b\sigma_n^{eff}$ are also often used. In general, in this formulation the state variable has the physical meaning of an average contact time of asperities between the sliding surfaces (Dieterich, 1986; Ruina, 1983). The first equation in (1.6) and (1.7) is usually named in the literature the governing equation, while the second is called the evolution equation. The evolution law in equation (1.6) is the slowness law (Ruina, 1983; Beeler et al., 1994; Roy and Marone, 1996), and it includes true ageing, while the one in equation (1.7) is usually named the slip law. The first logarithmic term in (1.6) and (1.7) represents the direct effect of friction (Dieterich, 1979), while the second accounts for the evolution of the state variable. In equation (1.8) τ_y is the upper yield stress, τ_f is the final kinetic friction level, u is the slip and D_c is the characteristic slip–weakening distance. The traction evolution associated to equation (1.8) is characterized by constant and linear traction decay and by a constant kinetic friction level. The characteristic length scale parameters of these two constitutive formulations are the slip weakening distance D_c and the parameter L : the former represents the slip required for traction to drop, the latter is the characteristic length for the renewal of a population of contacts along the sliding surface and controls the evolution of the state variable. In two recent papers Cocco and Bizzarri (2002) and Bizzarri and Cocco (2003) have investigated the slip

weakening behavior of the rate and state dependent constitutive law (1.6) and have shown that these two length scale parameters are different. They propose a scaling law between D_c and L , which states that their ratio is nearly 15 (in agreement with Okubo, 1989, and Guatteri and Spudich, 2000) and found analytical relations to associate SW and R&S constitutive parameters. We further discuss these results in the present chapter, focusing our attention on R&S friction law models with the perspective to provide a physical interpretation of the breakdown processes.

1.4 Methodology

We solve the elastodynamic equation (1.5) for a 2-D in-plane shear crack for which the displacement and the shear traction depend on time and only one spatial coordinate. That is, the fault is described with a line. We assume that the crack propagates only in the x_1 -direction. The medium is supposed to be infinite, homogeneous and elastic everywhere except along the fracture line.

Because we consider the fully dynamic problem, we have to solve the equation (1.5) numerically. In all the computations of this Thesis we have adopted the finite difference approach (one of the most known in the literature). We solve the fundamental equation by using a finite difference method where the fault is simulated as a plane of split nodes in the grid (the Traction-at-Split-Nodes, TSN, numerical technique). The approach is described in Andrews (1973) and in Andrews (1999). An extensive presentation of the adopted numerical procedure can be found in Bizzarri et al. (2001) and Bizzarri and Cocco (2003), who also discuss the required stability and convergence criteria as well as resolution of the cohesive zone. The fault is described by a number of slip nodes coupled to each other by constitutive relations. The solutions of discretized equations of motion are stepped through time by calculating the net force acting on every node, by adjoining the velocities and displacements and by recalculating the internal force every element exercises on its nodes. The plane is discretized in equilateral triangles to increase the numerical efficiency.

In our procedure we can use either R&S laws (with slowness evolution equation or with slip evolution equation) or SW law. Besides, for the uniqueness of the dynamic problem, the collinearity between the slip velocity (derivative of the displacement) and the shear traction on the fault is imposed.

1.5 Slip weakening in the R&S formulation

We present in this section the simulation of the dynamic rupture propagation on a homogeneous fault model with R&S friction law defined in equation (1.6). We review and discuss results of previous works with a uniform distribution of constitutive parameters. Therefore we interpret the physical mechanisms controlling the breakdown process and the slip acceleration in the framework of a rate and state constitutive formulation. This fault model can be considered as a reference model for the discussion that will be presented in the following of this chapter and in the chapter 2. An example of dynamic modelling with the slip weakening law will be presented in the chapter 4. The parameters adopted for this simulation are listed in Table 1. The model represents a velocity weakening fault for which the value of $b - a$ is 0.004 (i.e., $B-A = 0.4$ MPa). The results of this simulation are shown in Figure 2 and they represent a good example to discuss the typical behavior of a spontaneous dynamic rupture governed by R&S.

These calculations have been performed using values typical of laboratory experiments: the medium surrounding the crack is linear elastic, homogeneous and Poissonian and the total fault length is equal to 20 m. After initiation, the crack propagates symmetrically with respect to $x_1 = 0$. At the initial stage the fault is at steady state, except in the nucleation region, which is 3 m wide. The nucleation strategy adopted for the simulations is a time weakening controlled by the state variable and it is described in Bizzarri et al. (2001); the nucleation patch is quite small and the nucleation stage is relatively short. The spatial discretization is $\Delta x = 0.01$ m, and Δt is fixed from the Courant–Friedrichs–Levy ratio w_{CFL} , defined as $v_s \Delta t / \Delta x$. The convergence and stability of numerical simulations are discussed in detail in Bizzarri and Cocco (2003).

Figure 2a shows the spatio-temporal evolution of slip velocity, while the bottom panels display the traction evolution for a target point P1 as a function of state variable (Figure2b), slip velocity (Figure2c) and slip (Figure2d). We summarize in the following the most relevant features emerging from this simulation:

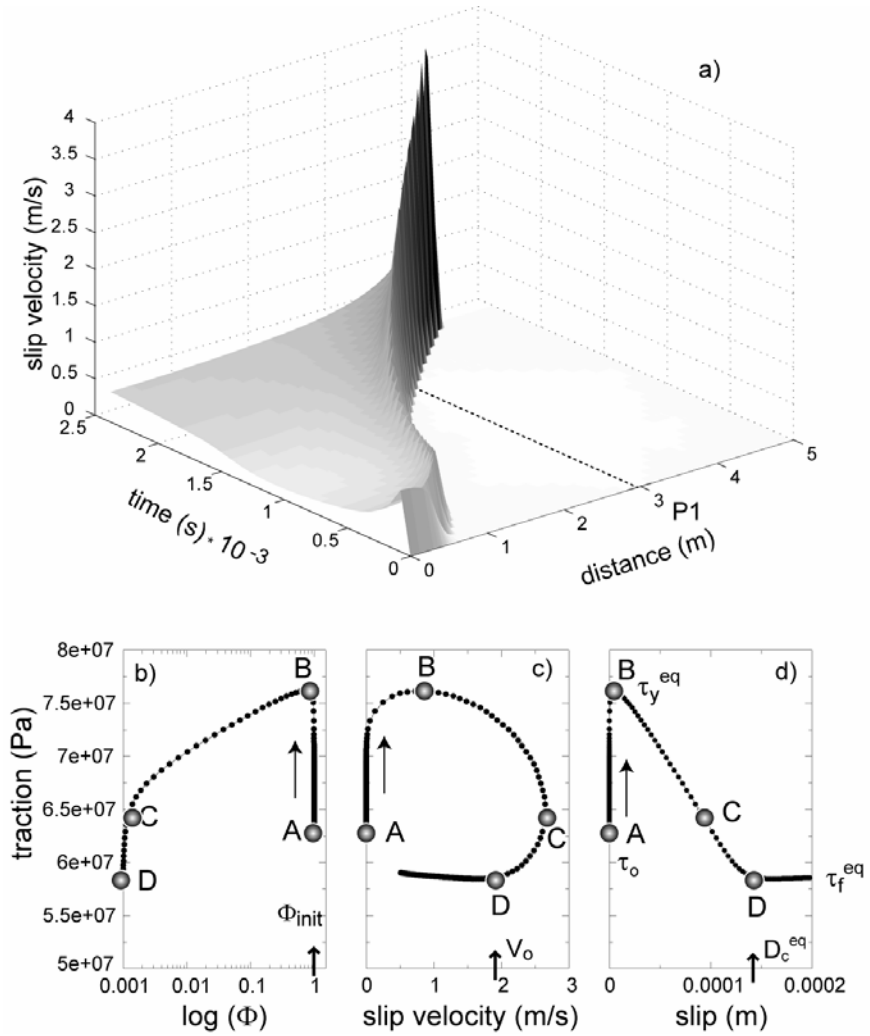


Figure 2: (a) The spatio-temporal evolution of slip velocity during the dynamic rupture propagation on a homogeneous fault. The initial and constitutive parameters used for these calculations are listed in Table 1. The bottom panels show the traction evolution as a function of state variable (b), slip velocity (c) and slip (d) for a target point P1. We indicate different stages of the dynamic rupture with letters (A – D).

1. The rupture speed increases during the dynamic propagation and remains for this configuration sub-shear ($v_{crack} \sim 2200$ m/s), although in general it might accelerate to a super-shear value, asymptotically approaching P-wave speed.

- Peak slip velocity increases during the dynamic propagation with an increasing spatial distance from the nucleation; the largest increase occur when the crack accelerates to higher rupture velocities (Figures 2a and 3).

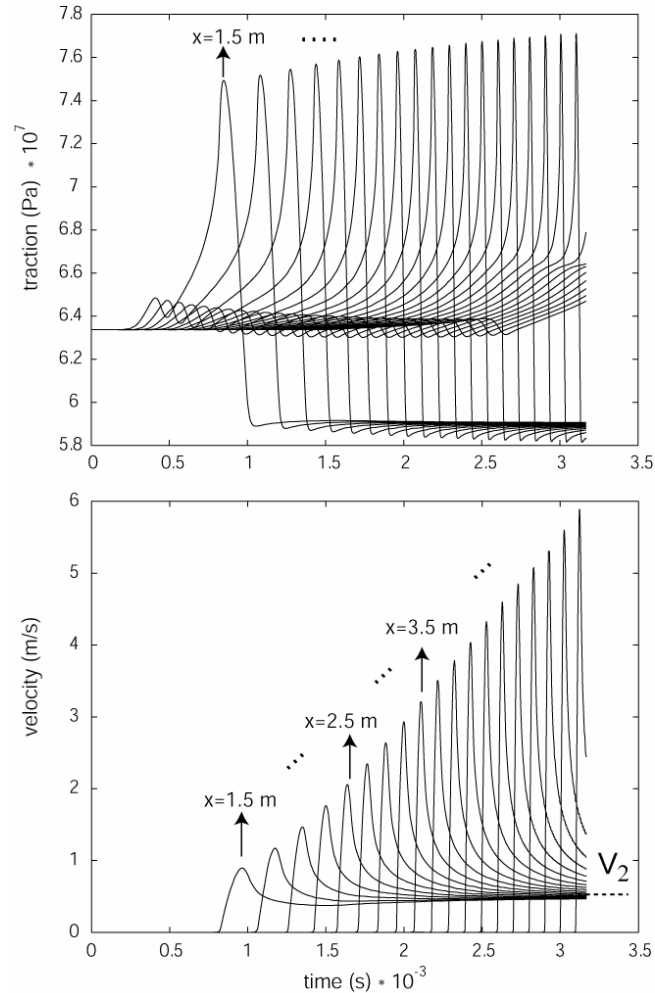


Figure 3: Temporal evolution of dynamic traction and slip velocity for several selected points located at different distances from the nucleation. The constitutive parameters are the same used for previous figure and are listed in Table 1.

- Simulations for a homogeneous configuration show no healing of slip: slip velocity does not drop to zero during the rupture propagation (Figures 2a and 3). All points have roughly the same final slip velocity value (v_2), which represents the velocity at the new steady state after the dynamic stress release (Figure 3).
- The dynamic traction evolution shows a characteristic slip-weakening behavior (Figure 2d for a target point P1). The weakening phase is denoted in

this figure by the labels B and D (the latter identifies the point in which dynamic traction reaches the kinetic stress value, τ_f^{eq} , see Figure 2d). According to Cocco and Bizzarri (2002) we call the slip required for traction to drop as “equivalent” slip weakening distance D_c^{eq} which does not coincide with the characteristic length scale parameter (L) of the R&S formulation (see also Gu 1984, and Gu and Wong, 1991; Nakatani, 2001).

5. The phase diagram shown in Figure 2c points out that the shear stress reaches the peak value (the yield maximum stress τ_y^{eq} indicated in Figure 2d and characterizing the point labeled B in the Figure 2) earlier than slip velocity (label C).
6. Figure 2b points out that during dynamic propagation the state variable evolves from the assumed initial steady-state value (Φ_{init}) to a new one ($\Phi^{ss} = L/v$). This represents the well-known self-damping behavior of the state variable. Bizzarri and Cocco (2003) and Cocco et al. (2004) have shown that it is the state variable evolution (line B-C in panel b) that drives the slip acceleration (same line in panel c) and most of the traction drop during the weakening phase (see panel d).
7. The duration of the weakening phase (line B-D in panels c and d) defines the breakdown zone duration T_c (see next section).
8. Simulations performed with a homogeneous configuration of R&S friction with a slowness evolution law (equation (1.6)) yield a constant weakening rate (see Figure 2d), provided that the spatial and temporal discretization is accurately selected to resolve the state variable evolution and the fast slip acceleration.

The considerations presented above are characteristic of the rupture propagation on a velocity weakening homogeneous fault. It is important to point out that the peak slip velocity, the yield stress, the dynamic stress drop, the rupture velocity, the slip weakening distance are strongly affected by the values of a and b .

Elastic moduli (Lamé constants)	$\lambda = \mu = 27 \text{ GPa}$
P and S wave velocities	$V_p = 5196 \text{ m/s}, V_s = 3000 \text{ m/s}$
Effective normal stress	$\sigma_n^{eff} = 100 \text{ MPa}$
R&S constitutive parameters	$a = 0.012, b = 0.016, L = 1 \cdot 10^{-5} \text{ m}$
Reference value for the friction coefficient	$\mu_* = 0.56, V_* = 1000 \text{ m/s}$
Initial values of the state variable within the nucleation zone and outside	$\Phi(x_i, t=0) = \begin{cases} \Phi_{nuc} = 1 \cdot 10^{-4} \text{ s} & , x_i \in [-1.5 \text{ m}, 1.5 \text{ m}] \\ \Phi^{ss}(v_{init}) & , \text{elsewhere} \end{cases}$
Fault discretization: spatial and temporal time steps	$\Delta x = 0.01 \text{ m}; \Delta t = 1.58e-6 \text{ s};$

Table 1. Model and Constitutive parameters adopted for the numerical computation of reference model.

1.5.1 The cohesive zone

The concept of cohesive zone has been originally introduced by Barenblatt (1959a, 1959b) for a tensile crack and subsequently by Ida (1972) for shear cracks in order to remove the physically unrealistic singularity of dynamic stress at the crack tip and to avoid an unbounded energy flux at the rupture front. The cohesive zone is the region of shear stress degradation near the crack tip; it is located just behind the rupture front and it is also named breakdown zone (Ohnaka and Yamashita, 1989). Different physical processes can be responsible of the shear stress degradation within the cohesive zone, and we refer to them as breakdown processes. The most important physical quantity that characterizes the breakdown process is the characteristic slip-weakening D_c . This parameter represents the amount of slip required to drop the dynamic traction from the upper yield stress (τ_y^{eq}) to the kinetic friction level (τ_f^{eq}) and to absorb fracture energy (see Figure 2d). D_c is an input parameter imposed *a priori* in the well known SW constitutive law (Andrews, 1976a and 1976b).

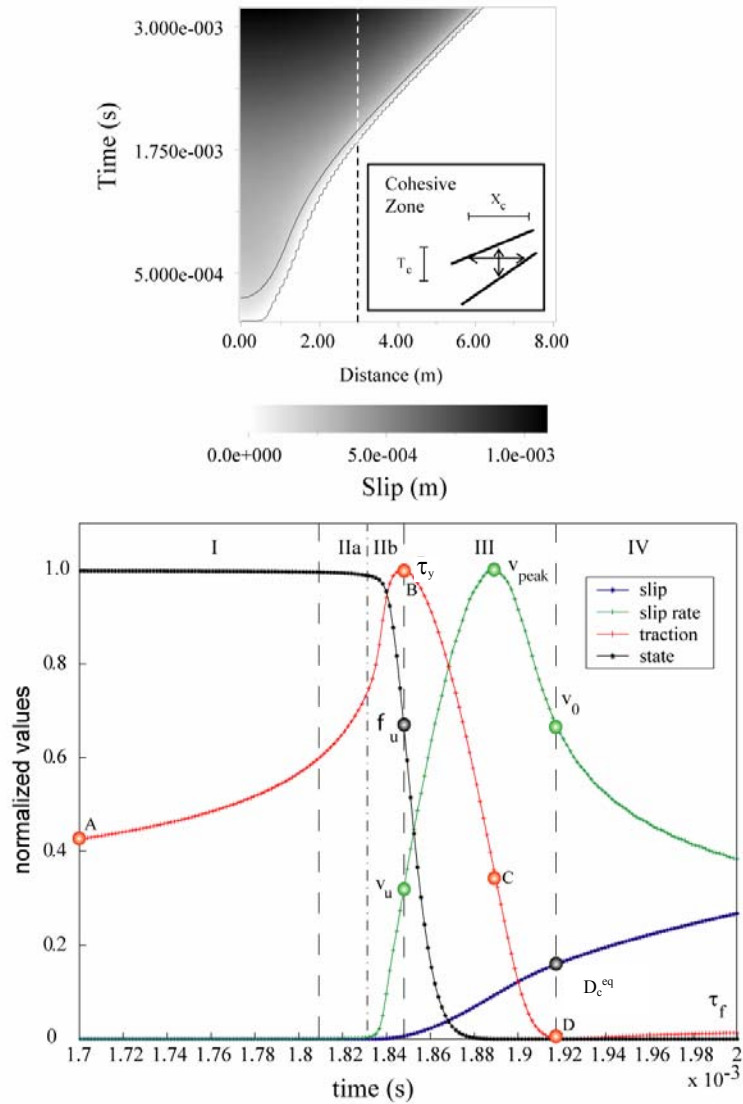


Figure 4: (a) Spatio-temporal evolution of slip for a 2D in-plane crack obeying to a slowness constitutive law (eq. 1.6). Slip amplitudes are shown with the grey scale. The black lines depict the cohesive zone where the total dynamic traction drops from the maximum yield stress (τ_y^{eq}) to the kinetic friction (τ_f^{eq}). The box inserted in panel (a) depicts a zoom of the cohesive zone: T_c is the duration and X_c is the spatial extension of the cohesive zone. (b) Time histories of slip, slip velocity, state variable and total dynamic traction at the fault point $x_1 = 3.0$ m. The amplitudes of each time history are normalized to its peak value to allow the comparison. The amplitude of peak slip velocity for this simulation is 2.65 m/s (at $1.95 \cdot 10^{-3}$ s), while peak value of traction is $7.62 \cdot 10^7$ Pa occurring at $1.85 \cdot 10^{-3}$ s. The residual stress amplitude at $1.92 \cdot 10^{-3}$ s is equal to $5.85 \cdot 10^7$ Pa. The value of the equivalent slip weakening distance is $1.6 \cdot 10^{-4}$ m. The stages of the dynamic failure process shown in Figure 2 are reproduced here for comparison. The slip velocity values at particular stage of the breakdown process are indicated and they are associated to the values of the other physical quantities. We indicate different stages with roman numbers (I – IV) as well as with letters (A – D). Initial and constitutive parameters are the same of previous figure.

As briefly mentioned above, numerical simulations performed by adopting R&S constitutive laws display a slip-weakening behavior of dynamic traction (see Figure

2d). Figure 4a shows the spatio-temporal evolution of slip for the same simulation illustrates in Figure 2. The drop of the stress occurs during a breakdown time T_c and over a breakdown distance X_c . This figure is useful to depict the cohesive zone, its dimension and duration during the crack propagation.

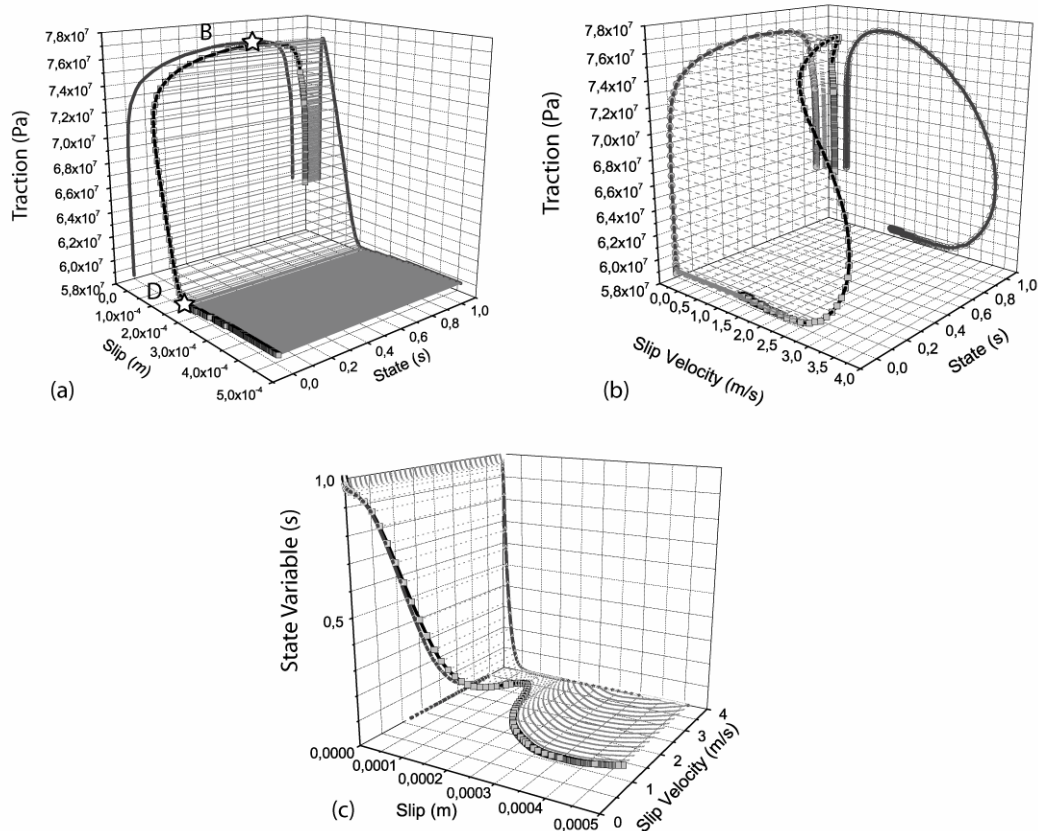


Figure 5: 3-D phase trajectories illustrating total dynamic traction as a function of slip and state (a) or slip velocity and state (b). (c) shows the state variable as a function of slip and slip velocity. The state evolves from the initial steady state (L/V_i) up to the final, new steady state. These calculations have been performed with the same constitutive parameters and at the same fault position as in previous figures. Letters B and D depict the same points as in previous figures.

In Figure 4b we compare the time histories of total traction, slip, slip velocity and state variable, normalized in amplitude and calculated for the same model parameters used in Figure 2 in the same fault position ($x_1 = 3.0$ m, i.e. outside the nucleation region). We have subdivided the time window shown in Figure 4b in five distinct stages, which comprise the duration of the whole breakdown process, and that are

associated with particular values of the slip velocity in Figure 2c (see corresponding letter A-D).

Figure 5 shows the 3-D plots of the relevant physical parameters: (a) and (b) illustrate the total dynamic traction as a function of state variable and slip or slip velocity, respectively; (c) shows the state variable as a function of slip and slip velocity. These figures highlight several important conclusions. First, the state variable evolution drives the slip acceleration and the traction drop during the weakening phase. This is evident in Figures 4b and 5c: the state variable evolves from its initial to the new steady state value during phase II and the beginning of phase III. The slip velocity reaches its peak when the state variable has already reached the final steady-state value (see Figures 4b and 5b, c). The traction increase during phase II is associated with this evolution. We emphasize that the traction does not reach its maximum simultaneously with to the peak of the slip velocity.

Slip weakening (phase III) begins when the state variable is evolving in a very short time and is half-way from the final value (Figures 4b and 5a). Moreover, the slip velocity evolution shows a clear velocity hardening behavior (phase I and II, from A to B in Figure 2c) followed by a velocity weakening (B to C in Figure 2c, belonging to phase III). Therefore, we can conclude that slip weakening and velocity weakening occur simultaneously and they are both driven by the state variable evolution (quite clear in Figure 5). Once slip velocity has reached its peak value (C in Figure 2c), the traction further decreases while slip decelerates (C to D in Figure 2c). The slip velocity evolution between the points C and D still belongs to phase III (i.e., slip weakening see Figure 4b). The fact that point C does not coincide with D, means that peak slip velocity occurs before the stress is at the kinetic level and the slip is equal to D_c^{eq} .

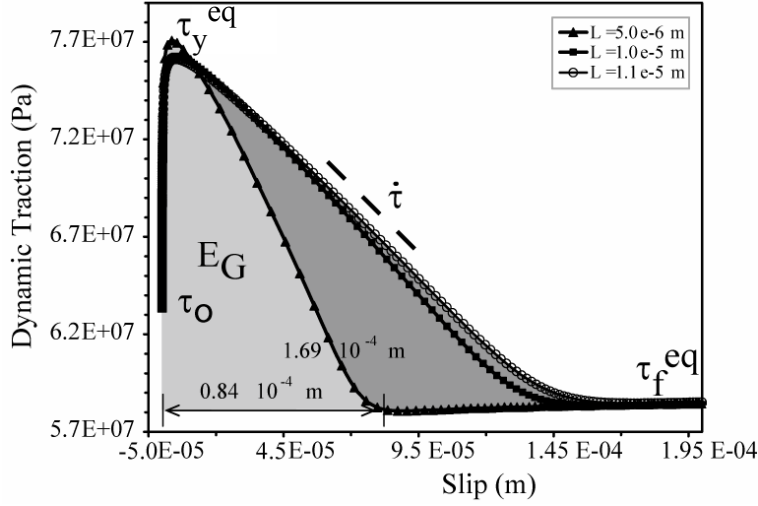


Figure 6: SW curves calculated from different simulations having the same initial and constitutive parameters (the same used in previous figures and listed in Table 1) except the characteristic distances L , ranging between 5 and 11 μm . We only change the spatial discretization to resolve appropriately the size and duration of the cohesive zone ($\Delta x = 0.005$ m). The shaded areas indicate the fracture energy, E_G , for two distinct configurations with the smallest and largest adopted L value. The equivalent slip weakening distance is 84 μm for $L = 5$ μm , 152 μm for $L = 10$ μm and 169 μm for $L = 11$ μm .

Figure 6 shows different slip weakening curves computed with different values of the parameter L and leaving unchanged all the other constitutive and initial parameters (Table 1). This figure shows that the equivalent slip weakening distance (D_c^{eq}) is larger than the parameter L (see Cocco and Bizzarri 2002) and that the absorbed fracture energy, as well as the resulting weakening rate, depend on the value adopted for the parameter L . Bizzarri and Cocco (2003) have proposed the following analytical relations to associate SW parameters to R&S constitutive and initial ones. Here we summarize these equations starting by the analytical relation between the two length-scale parameters:

$$D_c^{\text{eq}} = L \ln \left(\frac{V_o}{V_{\text{init}}} \right) \cong \frac{(\tau_y^{\text{eq}} - \tau_f^{\text{eq}})}{b \sigma_n} L. \quad (1.9)$$

This equation shows that the proportionality factor relating D_c^{eq} and L depends on the initial velocity (V_{init}) and on the slip velocity (V_o) reached when the slip is equal to D_c^{eq} (see Figure 4b). The latter is unknown a priori, and the last term in (1.9) expresses an approximate relation where the proportionality factor scales with the stress drop. This relation is valid only for the slowness law (1.6), as it will be discussed in the following. The dependence on L is well represented by (1.9) but the dependence on a and b is much more complex since both the yield stress and the kinetic friction depend on the constitutive parameters. In fact, numerical simulations presented by Bizzarri and Cocco (2003) have shown that the kinetic friction depends on the difference ($b-a$) as:

$$\tau_f^{eq} = \left[\mu_* + (b-a) \ln \left(\frac{V_*}{V_o} \right) \right] \sigma_n^{eff}. \quad (1.10)$$

The yield stress is related to the constitutive parameters through values (unknown a priori) of slip velocity (V_u) and state variable (Φ_u) reached when total traction is at the peak value (see Figure 4b). For the slowness law (1.6) the yield stress can be expressed as:

$$\tau_y^{eq} = \left[\mu_* + a \ln \left(\frac{V_u}{V_*} \right) + b \ln \left(\frac{\Phi_u V_*}{L} \right) \right] \sigma_n^{eff} \quad (1.11)$$

Equations (1.9), (1.10) and (1.11) allow the association of R&S and SW constitutive parameters. They also summarize the dependence of yield stress, kinetic friction and equivalent slip weakening distance on the R&S constitutive parameters. Figure 6 clearly shows that both the kinetic friction level and the yield stress do not depend on the value adopted for the parameter L , which indeed controls the equivalent slip weakening distance as stated in (1.9). Consequently, the fracture energy and the weakening rate depend on the parameter L .

We infer a value of D_c^{eq} larger than the adopted L parameter and the ratio D_c^{eq} / L ranges between 15 and 20, in agreement with Cocco and Bizzarri (2002), Bizzarri and Cocco (2003) and Lapusta and Rice (2003).

Numerical simulations, performed with constitutive parameters and fault parameterization at the laboratory scale ($L \sim 10 \mu\text{m}$ and $D_c^{eq} \sim 0.15 \text{ mm}$), yield fracture energy values ranging between 10^3 to 10^4 J/m^2 , in agreement with previous studies (Okubo and Dieterich, 1984). Recent studies have attempted to estimate the critical slip weakening distance from strong motion recordings (Ide and Takeo, 1997; Guatteri and Spudich, 2000) and suggested quite large values up to 0.5 m. There are several concerns, however, about the reliability of such large values of the critical slip weakening distance above all because they suggest that D_c may be a significant fraction of the maximum slip on the fault. Guatteri and Spudich (2000) pointed out that there is a limitation to infer D_c from ground motion waveforms because of the trade-off between critical slip and strength excess (i.e., the difference between yield and initial stress values). If the slip weakening law is assumed as the constitutive relation and D_c is the characteristic length scale parameter of the dynamic problem, then the nucleation patch scales with D_c . Cocco and Bizzarri (2002) have emphasized that in this case, adopting values of the critical slip weakening distance ranging between 0.1 m and 1 m, the nucleation patch dimension would be a large fraction of the whole rupture area. On the contrary, in the framework of a rate and state formulation, the nucleation patch scales with L and not with D_c^{eq} (if L were 1 mm the nucleation patch would be less than 1 km, see also Lapusta and Rice, 2002). However, in order to use the results of numerical simulations discussed here and to use the analytical relations proposed by Bizzarri and Cocco (2003) we have to solve the problem of scaling these results from the laboratory scale to the actual fault dimensions. Cocco and Bizzarri (2002) suggest that, if this scaling is allowed, according to laboratory experiments (Marone and Kilgore, 1993; Mair and Marone, 1999) L can be as large as 1 cm and the proposed scaling law would yield D_c value close to 0.2 m. In this case, the fracture energy ranges between 10^6 and 10^7 J/m^2 . The inferred D_c^{eq} values for actual earthquakes range between several centimetres to meters (see Chapter 6), suggesting that D_c may be a significant fraction of the

maximum slip on the fault. However, the scaling of the constitutive parameters from laboratory to real fault dimension is still an open question and different opinions exist about the reliability of these extremely large values of D_c for real earthquakes (see Guatteri and Spudich, 2000; Guatteri et al., 2003).

Chapter 2

Physical interpretation of the breakdown process using R&S constitutive laws

In this chapter, we aim to study the dynamic traction and the slip velocity evolution within the cohesive zone (see Figure 3 chapter 1) using a R&S constitutive law to understand the physical processes controlling the weakening and the healing mechanisms (i.e., the slip duration during the dynamic rupture propagation). In chapter 1 we have started noting that the SW behavior is the result of the dynamic failure process: in order to have a finite stress release the total dynamic traction drops when slip increases, which results in the commonly used slip-weakening behavior. This process occurs at the crack tip in a finite extended zone named the *cohesive zone* (Ida, 1972; Andrews, 1976-a,b; Ohnaka, 1996). Therefore, slip-weakening must occur within the cohesive zone, but this behavior is the result of the physical processes controlling the breakdown zone. It is well known from the literature that slip–weakening is a characteristic feature of rate and state constitutive laws (Okubo and Dieterich, 1984; Guatteri et al., 2001; Bizzarri et al., 2001). We also know an intrinsic limitation, characteristic of R&S models, to prescribe *a priori* the traction evolution within the cohesive zone, which depends on “unknown” slip velocity values associated with particular stages of the breakdown process.

We will use rate and state dependent constitutive laws to model the temporal evolution of slip velocity and dynamic traction during the propagation of a 2-D in-plane crack. We start only considering a velocity weakening regime, $b > a$ (we will show more deeply the classification of different R&S regimes in chapter 3). The goal is to understand the frictional control of slip weakening behavior and rupture healing. In the literature many different studies have discussed numerical simulations of dynamic slip on homogeneous faults showing either crack-like rupture mode or self-healing pulse propagation (Cochard and Madariaga, 1994, 1996; Perrin et al., 1995; Beeler and Tullis, 1996; Zheng and Rice, 1998). The healing of slip, leading to

short slip durations or self-healing pulse propagation mode, has been related either to stress and/or strength (frictional) heterogeneity (see for instance Beroza and Mikumo, 1996). Self-healing ruptures have also been shown to appear in rupture propagation between dissimilar materials (Weertman 1980; Andrews and Ben-Zion, 1997; Cochard and Rice, 2000).

In this chapter, we focus on the rupture propagation along homogeneous faults, while in the next chapter we will model faults with heterogeneous constitutive parameters. In such a homogeneous configuration, healing mechanism and self-healing pulses are related to the friction law (Perrin et al., 1995; Cochard and Madariaga, 1996; Beeler and Tullis, 1996; Zheng and Rice, 1998). We review and discuss previous modeling results and interpret the physical mechanisms controlling the breakdown process and the slip acceleration in the framework of a rate and state constitutive formulation.

2.1 The evolution law and the dynamic rupture growth

In the previous chapter we have discussed the results of several simulations performed for a 2-D in-plane crack obeying to a rate and state dependent law and using a slowness evolution equation as defined in equation (1.6). We have demonstrated that SW occurs within the breakdown zone and that the critical slip weakening distance is larger than the characteristic length scale parameter of the R&S formulation. We have concluded that the state variable evolution controls the weakening process and the consequent slip acceleration. Therefore, it is likely to expect that the analytical relation used for the evolution law can affect the SW behavior and the absorbed fracture energy. To test this finding, we compare the SW curves resulting from numerical simulations performed by using the same constitutive and initial parameters (see Table 1) for a slowness and a slip evolution laws, defined in equation (1.6) and (1.7) respectively. Figure 1 shows this comparison: our simulations clearly show that the slip weakening curves resulting from these two evolution laws are very different and that the equivalent slip weakening distance for a slip law is much lower than that obtained for a slowness

law (Bizzarri and Cocco, 2003). This result corroborates the idea that the state variable controls the weakening process and it suggests that the analytical relation (1.9), which was established for the slowness law, is not valid for the slip law. The kinetic friction is the same because the steady state friction value is the same for the two laws and the yield stress does not substantially change with the evolution law.

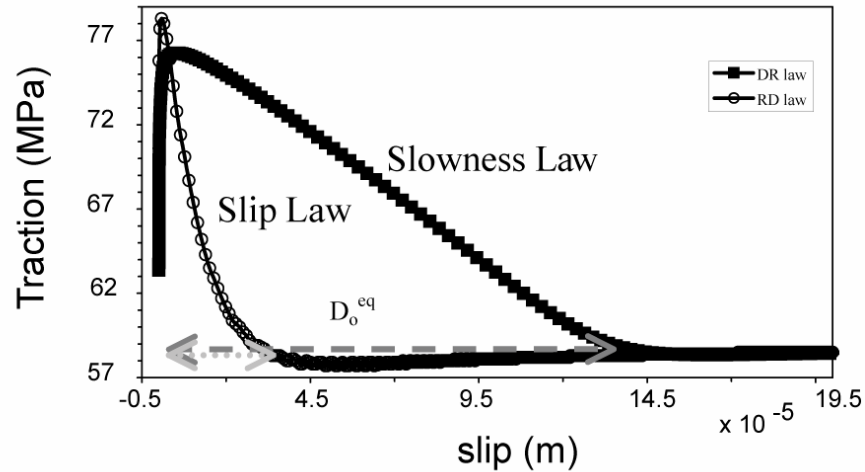


Figure 1: Comparison between the SW curves resulting from simulations performed using the slowness and the slip evolution law (defined in equations 1.6 and 1.7) with the same constitutive parameters. The shape of the SW curves and the associated critical slip distance are very different: while the slowness law yields a nearly linear decay, the slip law yields a faster stress drop with variable weakening rate ($\dot{\tau}$).

Our numerical results show that the slip velocity peaks resulting for a slip law are much larger than those simulated for a slowness evolution law. This is consistent with the shorter critical slip weakening distance that in turns results in a faster fracture energy release (as evidenced by the larger weakening rate) and a smaller cohesive zone size. According to Perrin et al. (1995) and Zheng and Rice (1998) we find that a slip or a slowness law do not yield self-healing or short slip duration, but the resulting solutions are always consistent with a crack-like rupture mode. In particular, Perrin et al. (1995) showed that no steady traveling pulse can occur if the constitutive law does not allow for restrengthening in truly stationary contact ($V=0$). Here we generalize the definition of self-healing pulses, also considering slip velocity time histories for which the residual velocity is very small although not necessarily zero after arrest. We have to remark that in a homogeneous fault self-

healing pulses can be generated either by modifying the fault constitutive law or by imposing an impulsive mode during rupture initiation, which is self-maintained during the dynamic rupture propagation (see Nielsen and Madariaga, 2002). We did not consider in this study the effect of stress and/or strength heterogeneity nor the effect of rupture propagation along a material interface. Our nucleation strategy does not prescribe the slip velocity pulse, because it is modeled as a time weakening controlled by the state variable.

2.2 The direct effect of friction

Beeler and Tullis (1996) have proposed two distinct strength functions that can yield fast restrengthening and self-healing following the Heaton (1990) suggestion that negative slip rate dependence can yield healing of slip. The first function is based on a sequential function characterized by a linear dependence on slip followed by a dependence on slip rate. Our simulations allow us to exclude this class of strength functions because we have shown that slip- and velocity- weakening occur simultaneously and not sequentially. The second function proposed by Beeler and Tullis (1996) is based on the rate and state dependent formulation, quite similar to that described by equation (1.6). They proposed a governing equation where the dependence on slip rate is eliminated by assuming a constant term for the direct effect of friction, which is included in the reference friction value (τ_{kf}):

$$\begin{aligned}\tau &= \tau_{kf} + b\sigma_n \ln \Theta \\ \frac{d\Theta}{dt} &= \frac{1}{L} [(V + V_{BT}) - \Theta V]\end{aligned}\tag{2.1}$$

where V_{BT} is an arbitrary slip velocity value. In this formulation, the state variable is non dimensional.

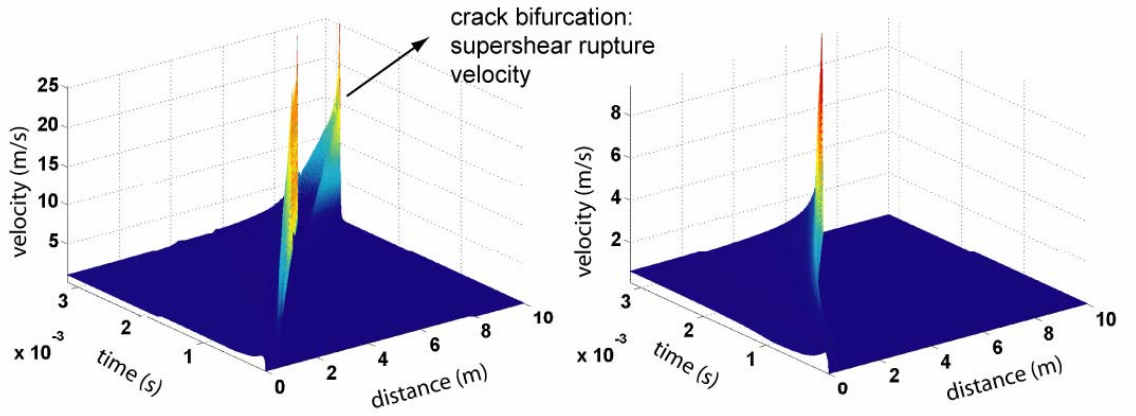


Figure 2: Spatio-temporal evolution of slip velocity for two simulations performed with different values of the parameter a (0.009 left panel and 0.0115 right panel) controlling the direct effect of friction in the governing equation. All the other parameters are those listed in Table 1. The slowness evolution law is used for these calculations. Smaller values of the parameter a yields higher rupture velocities (the rupture front bifurcation occurs only in the simulation with the smaller value).

Following Beeler and Tullis (1996), we investigate in this study the role played by the direct effect of friction and the friction behavior at high slip rates by using a slowness evolution law as defined in (1.6). Figure 2 shows the spatio-temporal evolution of slip velocity for two simulations having different values of the parameter a (0.009 and 0.0115, respectively) and leaving all the other parameters unchanged respect to the reference model shown in Chapter 1 (see Table 1). This figure shows that the peak slip velocity increases when a decreases and the crack propagation is faster (in this case, the simulation with the smaller a even shows a crack bifurcation and a jump in rupture velocity). The traction drop is faster when the direct effect of friction is reduced (small a). This result is physically reasonable and both simulations show a crack-like rupture propagation mode. We point out that we were unable to generate self-healing using a slowness constitutive law also reducing the contribution of the direct effect of friction by changing the value adopted for the parameter a .

We have also studied the effect of different velocity cutoff in the governing equation at high slip rates. We consider a governing equation (1.6) in which friction depends on slip rate when $V \ll V_{cut}$, while for $V \gg V_{cut}$ the direct term is frozen and taken constant $[a \ln(\frac{V_*}{V_{cut}} + 1)]$. In this case, friction still depends on slip velocity

through the evolution equation and the state variable. We show in Figure 3 the slip weakening curves resulting from the simulations performed with different velocity cutoff and we compare them with the reference model. This figure emphasizes that the direct effect of friction and the friction behavior at high slip rates largely control the kinetic stress level and the yield stress, while the equivalent slip weakening distance and the weakening rate are only slightly modified. The calculation with $V_{cut} = 2 \cdot 10^{-5} \text{ m/s}$ has a cutoff very close to the initial velocity (therefore, the direct effect of friction is constant and independent of slip rate during most of the simulation). The direct effect of friction of this model reduces the hardening phase (i.e. the yield stress value is close to the initial stress). The latter calculation has a higher slip rate cutoff, so that the direct effect of friction is frozen only when $V > 1 \text{ m/s}$.

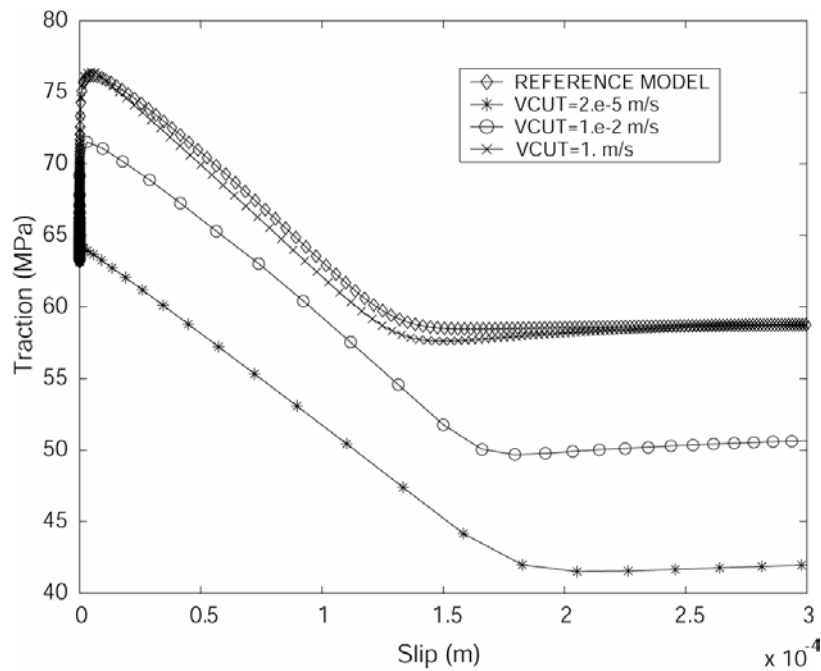


Figure 3: SW curves calculated from several simulations performed using a slowness law and different values of the slip rate cutoff (V_{cut}). The SW curve shown in Figure 1 is included for comparison, as the reference model.

However in all cases we are unable to simulate self-healing pulse mode with a slowness evolution law. It is important to point out that modifying the friction behavior at high slip rates affects the weakening processes within the cohesive zone.

Elastic moduli (Lamé constants)	$\lambda = \mu = 27 \text{ GPa}$
P and S wave velocities	$V_p = 5196 \text{ m/s}, \quad V_s = 3000 \text{ m/s}$
Effective normal stress	$\sigma_n^{eff} = 100 \text{ MPa}$
R&S constitutive parameters	$a = 0.012, \quad b = 0.016, \quad L = 1 \cdot 10^{-5} \text{ m}$
Reference value for the friction coefficient	$\mu_* = 0.56, \quad V_* = 1000 \text{ m/s}$
Initial values of the state variable within the nucleation zone and outside	$\Phi(x_1, t=0) = \begin{cases} \Phi_{\text{nucl}} = 1 \cdot 10^{-4} \text{ s} & , x_1 \in [-1.5 \text{ m}, 1.5 \text{ m}] \\ \Phi^{ss}(v_{\text{init}}) & , \text{elsewhere} \end{cases}$
Fault discretization: spatial and temporal time steps	$\Delta x = 0.01 \text{ m}; \quad \Delta t = 1.58 \text{e-}6 \text{ s};$

Table 1. Model and Constitutive parameters adopted for the numerical computation of reference model.

2.3 The evolution law and the healing mechanisms

We have discussed in the previous sections how the evolution law controls the dynamic rupture growth and the slip weakening behavior within the cohesive zone. We have also remarked that different modifications of the evolution law have been proposed to generate a self-healing or impulsive slip propagation mode. These attempts confirm our finding that the evolution law, peculiar of the rate and state formulation, play a dominant role in controlling the breakdown process and the temporal and spatial evolution of dynamic traction and slip velocity. The motivation to modify the evolution law for modeling short slip duration or self-healing consists in the impossibility to have such behaviors using slowness or slip constitutive laws (defined in equations 1.6 and 1.7). In this section, we present and discuss several simulations performed by using two other constitutive laws, which have been modified to have a fast restrengthening leading to the healing of slip. We start with the constitutive law proposed by Perrin et al. (1995) who suggested modifying the rate and state dependent laws used above to allow rapid restrengthening in truly stationary contact. These authors correctly emphasized that not all constitutive models allow for steady traveling wave pulses, and concluded that for the slowness

and slip constitutive laws used above steady pulse solutions do not exist. We believe that the observational constraints for steady pulse or constant rise time during real earthquakes are quite weak. In this study we attempt to model short rise times (that is, a slip duration much shorter than rupture duration which is independent of fault position) that are not expected with a crack –like rupture propagation mode. Perrin et al. (1995) proposed the following constitutive law:

$$\tau = \left[\mu_* + a \ln \left(\frac{V + V_{PE}}{V + V_*} \right) + b \ln \left(\frac{\Theta(V_* - V_{PE})}{L} + 1 \right) \right] \sigma_n^{eff}, \quad (2.2)$$

$$\frac{d\Theta}{dt} = 1 - \frac{\Theta(V + V_{PE})}{L}$$

where the velocity V_{PE} represents a low velocity cut-off with no weakening at slip rates $V \ll V_{PE}$ (see also Zheng and Rice, 1998). This version of the slowness evolution law allows for truly stationary contact ($V = 0$) and gives an upper limit to a contact time $\Theta \leq L/V_P$. Perrin et al. (1995) have shown that, using the constitutive law defined in (2.2), the spontaneous rupture propagation will occur either in the self-healing slip pulse mode (although not generally a steady pulse) or in the classical enlarging crack-like mode depending on the values of the adopted constitutive parameters. We show in Figure 4a the spatio-temporal evolution of slip velocity simulated using our 2-D algorithm, the constitutive law defined in (2.2), and the set of constitutive parameters listed in Table 1 with V_* equal to 10 m/s and V_{PE} equal to 10^{-2} m/s.

This figure emphasizes that slip velocity becomes very small and healing of slip clearly occurs. Slip duration is short and it is not associated to a steady pulse traveling along the fault. Figure 4b shows the time histories of state variable, slip, slip velocity and total dynamic traction and it points out again that the state variable drives the evolution of dynamic traction and the slip acceleration. The time window used in Figure 4b is too short to show the total duration of slip, but this is required to compare the different time histories.

However, the comparison between the time histories shown in this figure with that one shown in Figures 3 of Chapter 1 reveals the rapid increase of dynamic traction

immediately after the end of the weakening phase, which is due to the fast restrengthening causing the healing of slip.

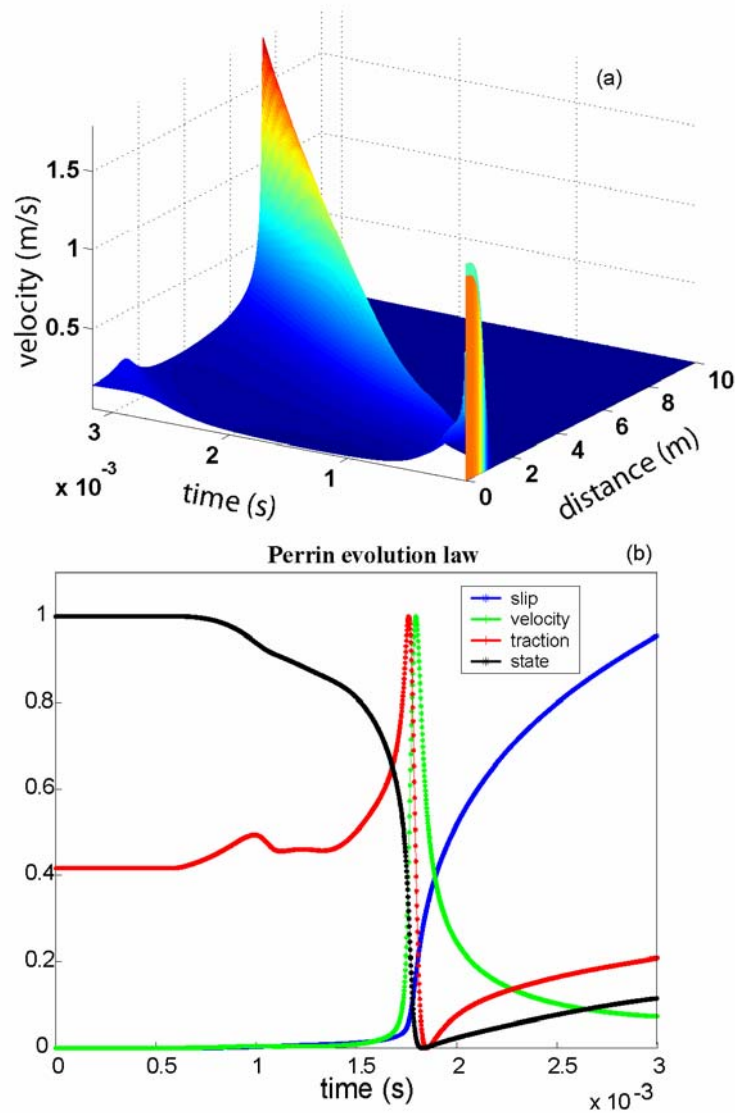


Figure4: (a) Spatio-temporal evolution of slip velocity from a simulation performed using the constitutive law proposed by Perrin et al. (1995) and stated in (2.2). The nucleation patch is shown by the larger initial slip rate (it is indispensable to favorite the nucleation). The reference slip velocity V_* in this simulation is equal to 10 m/s and the low velocity cutoff V_{PE} in (2.2) is 10^{-2} m/s. The solution shows healing of slip. The rapid restrengthening is so fast that the nucleation patch undergoes to an aseismic slip episode during the considered time window. (b) Time histories of slip, slip velocity, state variable and total dynamic traction calculated with the constitutive law described in (2.2).

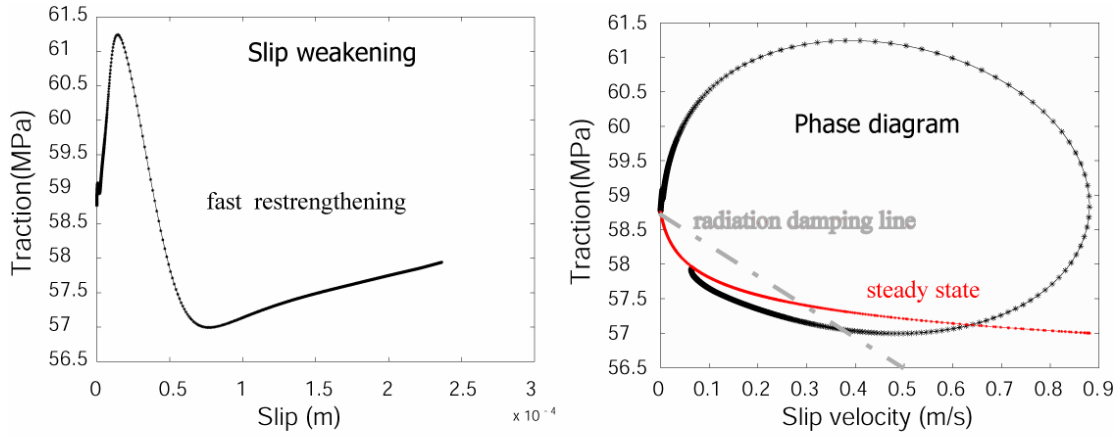


Figure 5: SW curve and phase diagram resulting from the simulations performed with the constitutive law described in (2.2). The red curve shows the steady state friction as a function of slip velocity. The straight dot-dashed (grey) line represents the radiation damping curve.

This is even more evident in Figure 5 where we have plotted the slip weakening curve and the phase diagram resulting from the constitutive law defined in (2.2). The dynamic traction shows an evident slip-hardening phase preceding the slip weakening (which is in general more pronounced than that obtained with the constitutive models previously discussed) and the kinetic friction level is maintained only for a short time because the rapid restrengthening causes the dynamic traction increase. The phase diagram is also peculiar since the dynamic system, after an evident velocity hardening and weakening phases, does not follow the steady state friction, which means that the state variable is not constant or at the steady state. The rapid restrengthening is so fast that during the time window of the dynamic propagation the rupture re-nucleates, or re-accelerates if the arrest is not actually completed (see Figure 4a).

The constitutive law (2.2), proposed by Perrin et al. (1995), includes a modification of the slowness constitutive relation (1.6) motivated by the physical requirement to allow stationary contact. Many different modifications of the rate and state constitutive laws have been proposed in the literature to attempt to explain self-healing or other dynamic processes, but only few of them are based on physical requirements. Nielsen and Carlson (2000) proposed a state dependent friction law that incorporates rate weakening and a characteristic time for healing.

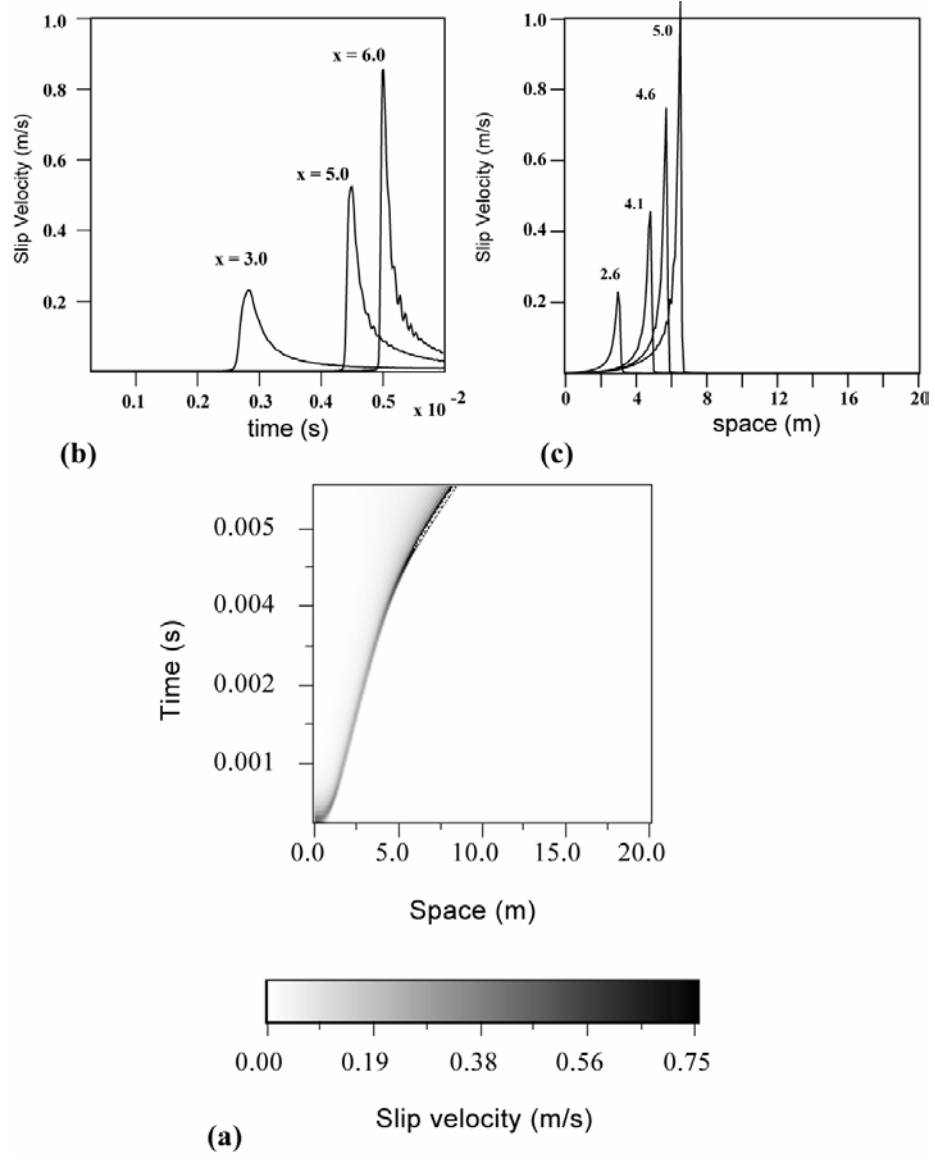


Figure 6: (a) Spatio-temporal evolution of slip velocity calculated for a simulation performed using the constitutive law described in (2.3) and a characteristic values for t_{th} equal to $3.9 \cdot 10^{-3}$ s. The top panels show the slip velocity as a function of time (b) at different points on the fault line and of space (c) calculated at different time steps (in seconds).

In this study, we have used a constitutive law where the governing equation is the same as the one used in (1.6) but the evolution law is that proposed by Nielsen et al. (2000) and Nielsen and Carlson (2000). This constitutive model has the form:

$$\tau = \left[\mu_* - a \ln \left(\frac{V_*}{V} + 1 \right) + b \ln \left(\frac{\Phi V_*}{L} + 1 \right) \right] \sigma_n^{eff} \quad (2.3)$$

$$\frac{d}{dt} \Phi = \frac{\gamma - \Phi}{t_{fh}} - \frac{\Phi V}{L}$$

where γ has the dimensions of seconds and is taken equal to 1 and t_{th} is the characteristic time for healing. The constitutive model described in (2.3) is different from that used by Nielsen and Carlson (2000) because we used a lab-derived governing equation in which we assign appropriate values to the parameters a and b . Moreover, we performed simulations with a dimensional data set that we will discuss in the following.

We have performed several simulations using the constitutive model (2.3) with the same set of parameters used in previous figures (listed in table 1) and changing the value of the characteristic time t_{th} . Our simulations show that if the characteristic time is appropriately chosen the solutions show a slip-pulse propagation mode with a nearly constant rise time. Values of the characteristic time larger than 0.1 s yield temporal evolution of slip velocity and dynamic traction very similar to the reference model. The healing of slip occurs when t_{th} becomes smaller than $5 \cdot 10^{-3}$ s. Figure 6 shows the results of a simulation performed using the values of parameters listed in Table 1 and a value of the characteristic time for healing (t_{th}) of $3.9 \cdot 10^{-3}$ s: slip velocity behavior shows a nearly constant duration and its peak increases as the crack advances. Figure 7 shows a 3-D plot with the traction dependence on slip and slip velocity. This figure shows a phase diagram quite similar to those previously discussed and a rapid increase of dynamic traction (restrengthening) immediately following the slip weakening phase that generates the healing of slip. Figure 7 shows a comparison between the 3-D phase trajectories resulting from the constitutive models (2.2) and (2.3) [a and b , respectively], which are very similar.

The results of our simulations are summarized in Figure 8 where we plot the superposition of slip profiles calculated at different times for three different constitutive models. The top panel shows the slip behavior resulting from the classical slowness law defined in (1.6) and it reveals that no healing occurs and the rupture propagates in the enlarging crack-like mode. The other two panels show the slip behavior resulting from the Nielsen and Carlson (2000) and the Perrin et al. (1995) constitutive models defined in equations (2.2) and (2.3), respectively. These models show short slip durations resembling a self-healing propagation mode.

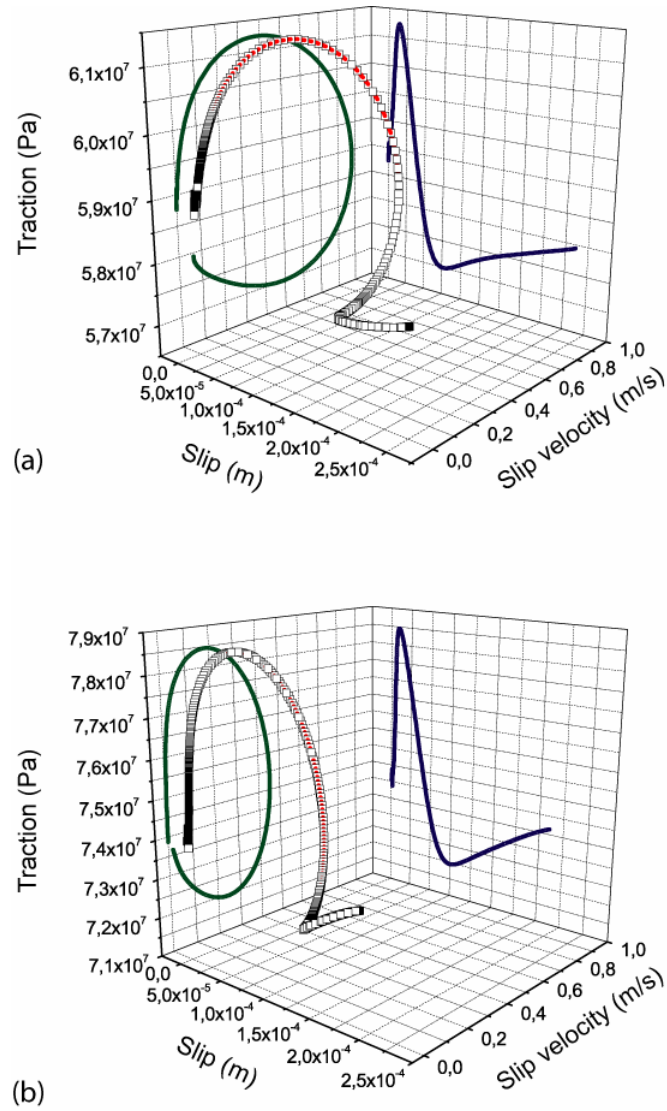


Figure 7: Comparison between the 3-D phase trajectories resulting from the simulations performed with the constitutive laws described in (2.2) (top panel - a -) and (2.3) (bottom panel - b -) and showing total dynamic traction as a function of slip and slip velocity. The slip weakening behavior resulting from these two distinct constitutive laws is very similar, while the inferred values of slip velocity are quite different.

These results confirm that appropriate modifications of the evolution law can lead to self-healing slip propagation mode, but this requires the introduction of other characteristic parameters [a velocity cutoff in (2.2), or a characteristic time in (2.3)] that must be chosen without objective constraints. This implies that healing occurs with these constitutive laws only for particular set of the initial and constitutive parameters.

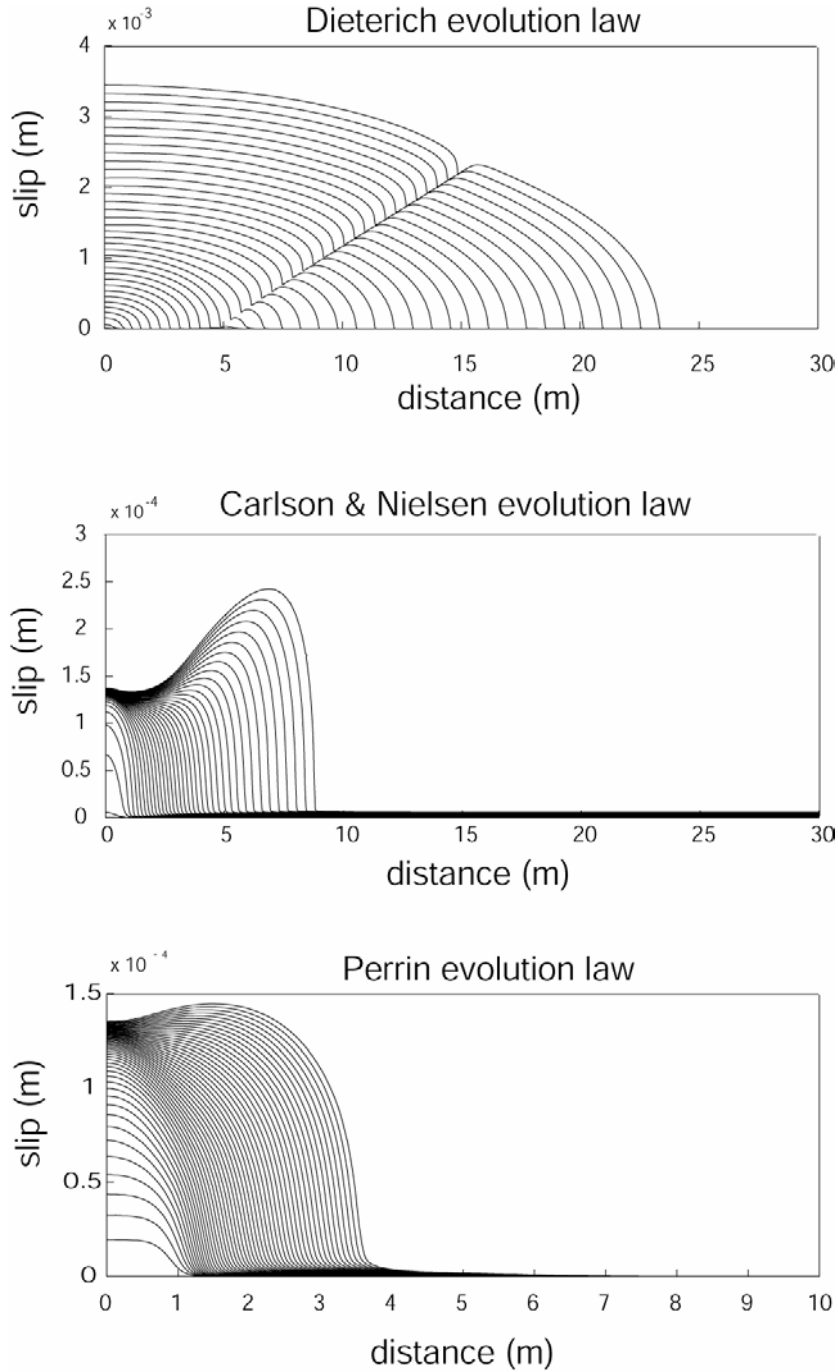


Figure8: Comparison between the slip profiles, obtained by the superposition of snapshots at different time steps of slip along the fault line, resulting from simulations performed with a slowness evolution law (top panel) and with the evolution laws described in (2.2), middle panel, and (2.3) bottom panel.

2.4 Discussions

We want to provide a physical interpretation of the breakdown process in order to explain the weakening mechanisms responsible for crack propagation and healing of slip. We model a 2-D in-plane rupture propagation along a homogenous fault line and we adopt rate and state dependent constitutive laws. We have illustrated that this

constitutive model allows the quantitative simulation of the rupture initiation and propagation and involves slip weakening within the cohesive zone. We have demonstrated that in the framework of rate and state constitutive laws the evolution equation of state variable governs both the weakening mechanisms and the healing of slip. We have compared different evolution laws and we conclude that slowness and slip constitutive models appropriately describe the rupture initiation and propagation but are unable to generate slip velocity pulses or short rise time, since the rupture grows as an enlarging crack-like mode. Therefore, the choice of the evolution law is crucial to represent the weakening and healing mechanisms in a homogeneous fault.

In order to perform the simulations discussed in this study and to interpret the state variable evolution it is necessary to have an optimal resolution of the cohesive zone. This implies that, even if the convergence and stability criteria are satisfied and solutions are found in a continuum model of fault dynamics, it is necessary to choose accurately the spatial and temporal discretization to follow and image the fast state variable evolution. This observation explains the intrinsic limitation in constraining constitutive parameters and slip velocity evolution by modeling radiated seismic waves (see also Guatteri and Spudich, 2000), which would require the modeling of high frequency waveforms. Because the zone of very rapid state evolution (controlling stress and slip velocity behaviors at the crack tip) scales with L , estimating the value of this length scale parameter is crucial to define the resolution and to identify the dimensions of nucleation patch and cohesive zone. Therefore, for these purposes, the adoption of a slip weakening model is much more practical, because it allows us to prescribe the traction evolution within the cohesive zone, to constrain the fracture energy and to simulate radiated ground motions. The dependence of yield stress, kinetic friction level and D_c values on slip velocity values, which are unknown *a priori*, makes the simulation of spontaneous rupture propagation with rate and state constitutive models less feasible.

In the framework of a rate and state formulation, appropriate modifications of the evolution law allow us to simulate spontaneous ruptures propagating as a slip velocity pulse with short rise times, thus including self-healing. These constitutive models are characterized by a rapid restrengthening occurring immediately after the end of the weakening stage. However, these constitutive laws have never been tested in laboratory. This raises the question on the reliability of these analytical

modifications of lab-derived constitutive laws to explain short slip durations, even when motivated by physical arguments.

By adopting the rate and state dependent laws, we try to incorporate the dependence of the friction coefficient on time as well as on the properties and roughness of the fault surface. However, other factors such as thermal pressurization and pore fluid lubrication can affect the effective normal stress, thus modifying the friction law ($\tau = \mu \sigma_n^{eff}$). Moreover, heterogeneities of constitutive parameters and complexities of fault geometry and earth structure should be considered in our modeling attempts, as we will show in the next chapter.

We aim to identify and model those mechanisms occurring in the cohesive zone, which are controlled by the constitutive law. According to our results, we can interpret the breakdown process in terms of the roughness and the properties of the contact surface, which evolves during sliding. Thus, in this context, we extend the physical interpretation of the state variable evolution, proposed to describe the nucleation and the long term restrengthening, to interpret the dynamic failure episode during the crack propagation (i.e., the breakdown process). The important conclusion of this chapter is that slip weakening should not be considered as an alternative description of the breakdown process. We propose that the state variable evolution controls slip weakening, because in the framework of a rate and state constitutive formulation it governs the weakening mechanisms and the slip acceleration. We have to remind here, however, that complementary interpretations of the state variable and its evolution law exist: Segall and Rice (1995) and Sleep (1997) proposed to relate the state variable to the porosity within the fault zone, thus accounting for the effects of dilatancy and pore compaction. Therefore, while we have shown that the evolution law governs the breakdown process, the physical interpretation of the state variable is not uniquely defined, because it depends on different competing mechanisms.

Chapter 3

Heterogeneous faults modelled with R&S law

Numerous recent investigations have shown that the rupture history imaged on the fault plane during moderate-to-large magnitude earthquakes is quite complex: slip is non-uniformly distributed on the fault and rupture velocity or slip duration can change dramatically during the dynamic rupture propagation. The heterogeneity of slip and the variations of rupture speed are certainly associated to the complexity of fault geometry, to the non-uniform distribution of pre-stress (Day, 1982; Peyrat et al., 2001) as well as to the variations of frictional properties on the fault plane (Boatwright and Cocco, 1996). The short slip duration and the healing of slip can also be associated to stress heterogeneity (Beroza and Mikumo, 1996; Day et al., 1998) or rupture propagation between dissimilar materials (Andrews and Ben Zion, 1997; Cochard and Rice, 2000). Otherwise, in a homogeneous configuration the healing of slip has been modeled by appropriately modifying the constitutive relation (see previous chapter and see Perrin et al., 1995; Zheng and Rice, 1998) that allows traction re-strengthening. However, as we have seen in chapter 2, although the constitutive laws which include self-healing of slip are physically reasonable, they have not been corroborated with laboratory experiments.

In this chapter we model the dynamic propagation of an earthquake rupture on a heterogeneous fault still using R&S constitutive laws. This implies that we have to describe and represent the frictional heterogeneity in terms of non-uniform distributions of R&S constitutive parameters along our 2-D fault model. Several studies were focused on the investigation of the effects of spatial heterogeneities of the constitutive properties (see Tse and Rice, 1986; Rice, 1993; Boatwright and Cocco, 1996 among many others). In particular, Boatwright and Cocco (1996; BC96 in the following) discussed the frictional control of crustal faulting by using a R&S law and a single degree of freedom spring-slider dynamic system. They proposed that the fault response to the dynamic stress perturbations can differ depending on

the variability of the constitutive parameters. They proposed four frictional fields separating the velocity weakening regime (VW) into strong and weak fields and the velocity strengthening regime (VS) into compliant and viscous response (see Table 1). BC96 associated these four frictional regimes with different values of the constitutive parameters and with observed features of seismicity and strain release as depicted in Table 1. Several authors have suggested that fault frictional parameters can vary with depth (Blanpied et al., 1991, 1995; Rice, 1993; Lapusta et al., 2000 among many others). BC96 proposed that these frictional parameters can also change along the fault strike, suggesting that frictional properties may control crustal faulting. We investigate by means of our 2-D finite difference algorithm the rupture propagation on a fault modeled through the different regimes proposed by BC96. We study how the interaction between velocity weakening and velocity strengthening portions of a 2-D fault can affect the dynamic rupture propagation.

<i>Regime</i>	<i>Description</i>	<i>A and B</i>	<i>Seismicity</i>	<i>Strain Release</i>
Velocity weakening (VW)	Strong Seismic (S-VW)	$B \gg A$	main shocks and some aftershocks	episodic dynamic slip
	Weak Seismic (W-VW)	$B - A > 0$ $B - A \leq 0.05 \text{ MPa}$	interseismic, foreshocks, main shocks and aftershocks	creep and intermittent dynamic slip
Velocity strengthening (VS)	Compliant (aseismic)	$A - B > 0$ $A - B \leq 0.1 \text{ MPa}$	some aftershocks	creep and forced dynamic
	Viscous (aseismic)	$A \gg B$	None	stable sliding

Table 1. Frictional behaviors proposed by Boatwright and Cocco (1996). The parameters A and B represent $a\sigma_n^{eff}$ and $b\sigma_n^{eff}$, respectively.

3.1 The velocity-weakening frictional regime

Because we are interested in modeling the spontaneous dynamic propagation of an earthquake rupture, we first consider the propagation in a velocity weakening

frictional regime (VW). This frictional behavior is characterized by $(B-A) > 0$ and relatively small values of the L parameters. We present in this section the results of several simulations performed on a homogeneous fault. The model parameters used for these simulations are listed in Table 2. We consider a set of parameters representative of the laboratory scale and we assume a constant normal stress σ_n^{eff} ($\sigma_n^{eff} = \sigma_n - p_{fluid}$; where p_{fluid} is the pore fluid pressure).

The velocity weakening behavior ($A < B$) represents the unstable regime that causes dynamic slip episodes on the fault plane, dynamic stress drop and the emission of seismic waves. For instance, we can associate VW patches to intermediate depth fault portions, as those located between 3 to 15 Km along the S. Andreas Fault.

3.1.1 Strong Velocity-Weakening Fault

We first model a VW regime characterized by a relatively large difference of constitutive parameters ($B-A \geq 0.6$ MPa) and, according to BC96, we refer to it as a strong velocity weakening regime (S-VW). The results of the simulations are shown in Figure 1 and the input and constitutive parameters are listed in Table 2. The strength parameter has been introduced by Das and Aki (1977a, 1977b) to quantify how a fault area is unstable and ready to fail [$S = (\tau_y - \tau_0) / (\tau_0 - \tau_f)$]. For a 2-D fault governed by a linear SW law, Andrews (1976a, 1976b) showed that S expresses also a limit to discriminate if a crack can ($S < 1.77$) or can not ($S > 1.77$) propagate with super-shear rupture velocity. For R&S constitutive laws it is possible to define a parameter S^{eq} equivalent to S by using the values of parameters τ_y^{eq} , τ_0 , τ_f^{eq} (Bizzarri and Cocco 2003). The simulation shown in Figure 1, by using the R&S constitutive laws for a strong seismic behavior ($B - A = 0.75$ MPa), is associated with a value of equivalent parameter $S^{eq} < 1.77$.

We can clearly see in Figure 1a that the rupture front bifurcates; this has been previously obtained by Okubo (1989) and by Bizzarri et al. (2001). The spatio-temporal plot shown in this figure has been drawn with a resolution smaller than that adopted for numerical calculations in order to better illustrate the increase of peak slip velocity and the jump in rupture front speed.

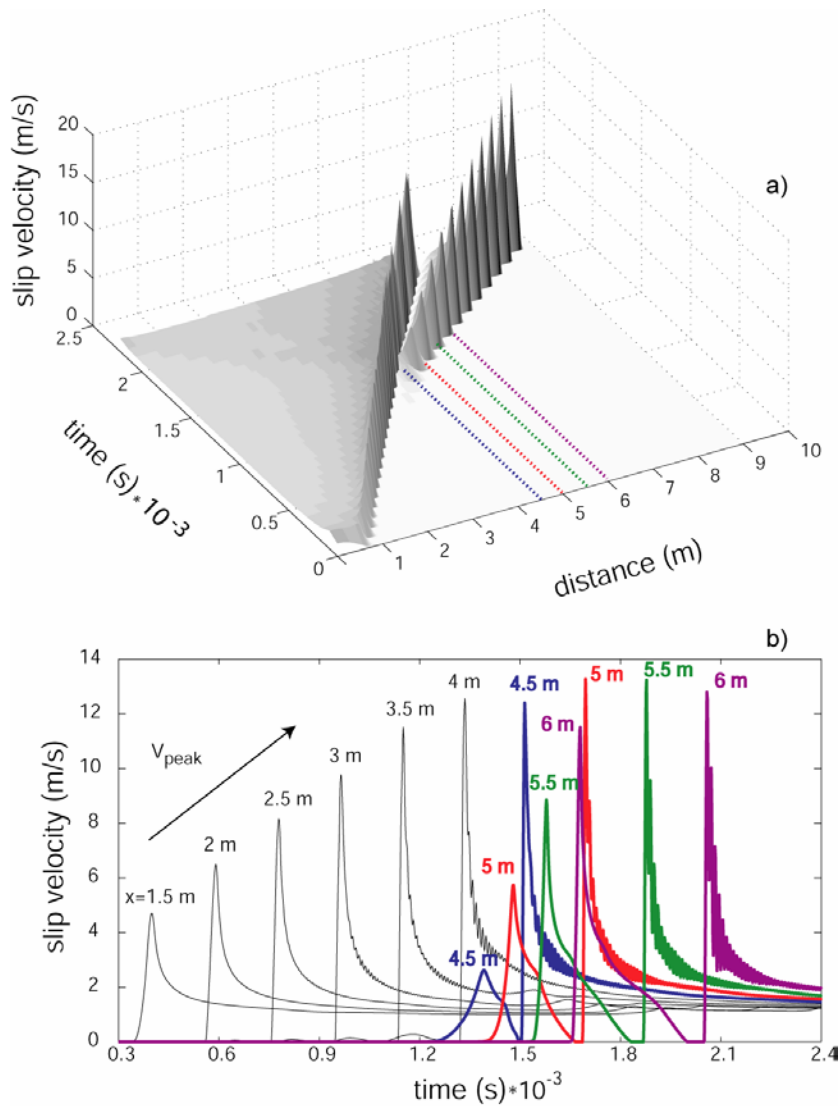


Figure 1: Dynamic rupture propagation on a strong velocity weakening fault. The model and constitutive parameters used for these calculations are listed in Table 2. Top panel shows the spatio-temporal evolution of slip velocity. We have drawn this plot with a reduced resolution in order to emphasize the increase in peak slip velocity. Bottom panel shows the time histories of slip velocity in different positions along the fault: black lines identify those points located before the point where crack accelerates to a super-shear rupture velocity, while colored curves identify those points located in the region where the crack has bifurcated.

Figure 1b shows the temporal evolutions of slip velocity: black lines indicate slip velocity time histories at those fault positions located before the acceleration of the rupture front to super-shear speed; the colored lines show slip velocity at those points where the crack is bifurcated. The increase of peak slip velocity occurs only within the cohesive zone: thus, we observe it only in the external rupture front.

Moreover, these simulations illustrate that when the rupture jumps to a super-shear rupture velocity the slip velocity, drops to zero and thus slip heals before to accelerate to internal rupture front.

<i>Parameter</i>	<i>Strong Seismic Regime</i>	<i>Weak Seismic Behavior</i>
$\lambda = \mu$	27 GPa	27 GPa
v_P	5196 m/s	5196 m/s
v_S	3000 m/s	3000 m/s
μ_0	0.56	0.56
a	0.0085	0.015
b	0.016	0.016
L	1×10^{-5} m	0.8×10^{-6} m
σ_n^{eff}	100 MPa	100 MPa
v_{init}	1×10^{-5} m/s	1×10^{-5} m/s
Φ_{nucl}	1×10^{-4} s	1×10^{-4} s
$\Phi_{outside\ the\ nucleation}$	$\Phi^{ss}(v_{init})$	$\Phi^{ss}(v_{init})$
τ_0	$\tau^{ss}(v_{init})$	$\tau^{ss}(v_{init})$
Nucleation region	[-1.5 m, 1.5 m]	[-2.0 m, 2.0 m]
Δx_1	0.01 m	0.01 m
Fault region	[-10 m, 10 m]	[-10 m, 10 m]

Table 2. Model and constitutive parameters adopted for the numerical experiments for homogeneous configurations. The set of parameters refer to a typical laboratory scale.

Thus, a strong VW regime allows the simulation of earthquake ruptures in agreement with theoretical experiments performed with a slip-weakening law (see Bizzarri et al., 2001, and references therein) and with laboratory experiments (Rosakis et al., 2000).

The strong seismic areas have a large breakdown stress drop (defined as the difference between the yield and the frictional stress $\Delta\tau_b = \tau_y^{eq} - \tau_f^{eq}$) and very large co-seismic slip: in a strong VW patch, slip and peak slip velocity are three times larger than those obtained for the reference model (Figure 2 Chapter 1) at the same

distances from the nucleation. The rupture velocity is close to 2.6 km/s immediately after the nucleation and the external front moves at about 4.5 km/s after the bifurcation. The separation between the two fronts increases going far from the nucleation, because of the different rupture velocities.

3.1.2 Weak Velocity-Weakening Fault

According to BC96 we define a *weak fault* as a fault characterized by a small difference between A and B ($B - A < 0.05\text{MPa}$). The results extrapolated by comparing Figure 2 of Chapter 1 and Figure 1 of this Chapter are representative of simulations characterized by values of B and A parameters selected to have $(B - A) > 0.2\text{ MPa}$. We experienced a severe difficulty to achieve a spontaneous nucleation and then spontaneous dynamic rupture propagation with $0\text{ MPa} < B - A < 0.1\text{ MPa}$ performing many numerical experiments. We point out here that decreasing $(B - A)$ we increase the dimension of the nucleation patch, which is defined as (Dieterich, 1992):

$$l_c = \eta \mu L / (b-a) \sigma_n^{eff} \quad (3.1)$$

where η is a geometric constant that depends on the crack type. Therefore, to avoid increasing the size of the nucleation patch we are confined to use a smaller L . We have obtained a spontaneous nucleation using $(B - A) = 0.1\text{ MPa}$ and $L = 0.8 \cdot 10^{-6}\text{ m}$ (see Table 2 for the whole set of adopted parameters). As expected, under these conditions the slip velocities within the nucleation patch (where the instability is promoted) are much larger than those inferred during the dynamic propagation within the weak fault portion. Our modeling results suggest that: i) peak slip velocity in weak regions can be even more than 10 times smaller than that simulated for the reference model; ii) the breakdown stress drop is decreased by 30%, although yield stress and kinetic friction level are both decreased; iii) the equivalent slip weakening distance decreases because both the breakdown stress drop and L decrease; iv) the inferred rupture velocity is smaller than that of the reference model and we never observe a crack bifurcation; v) despite the smaller values of the dynamic parameters we still retrieve an evident slip weakening behavior of the traction versus slip curves.

We believe that these results and the inferred behavior of a weak fault portion are physically reasonable because, according to BC96, we expect that weak fault zones undergo to dynamic instabilities only during micro-earthquakes or when they are loaded by a dynamic rupture front propagating in an adjacent strong weakening area. We will model this latter behavior in the next section.

3.2 Numerical representation of frictional heterogeneities

The goal of this section is to model the dynamic rupture propagation on a 2-D heterogeneous fault. Because in our approach the spontaneous dynamic propagation is governed by the R&S friction law, we represent the source heterogeneities in terms of non-uniform distribution of constitutive parameters. As described above, we follow the findings of BC96, who proposed that both the velocity weakening and the velocity strengthening regimes (see Scholz, 1990 and 1998) are separated into two fields depending on the values of constitutive parameters and the response to external loading (see Table 1). As shown in the previous section an earthquake rupture can spontaneously nucleate only within strong velocity weakening area (S-VW), characterized by sufficiently large values of the parameters $(B - A)$ and L . However, a dynamic rupture can propagate also in a weak velocity weakening area (W-VW). Nucleation in these regions occurs only for very small earthquakes or when it is forced by a sudden external stress change. We remind here that in their original classification BC96 have used the A and B parameters, which in the present study correspond to $A = a\sigma_n^{eff}$ and $B = b\sigma_n^{eff}$.

The velocity strengthening (VS) behavior (defined by the condition $A > B$) models a stable sliding, i.e. an aseismic slip. By definition, it is impossible to obtain spontaneous rupture propagation for a homogeneous case. The VS behavior has been proposed to describe several portions of the San Andreas Fault, which are characterized by creep events (see Scholz, 1990). A VS area can be characterized by the thickness of unconsolidated sediments (like Southern California) or by unconsolidated gouge within the fault (like in Central California; Marone et al., 1991). According to BC96 the velocity strengthening areas can contribute to the

arrest of an earthquake rupture. In particular, compliant areas are velocity strengthening fault regions that slip aseismically but can be driven to instability if they are sufficiently loaded by an abrupt stress increase due to the rupture propagation in an adjacent velocity weakening area (BC96). The VS behavior is characteristic of the R&S laws and it cannot be simulated by using the SW law.

The two “intermediate” fields proposed by BC96, weak and compliant, have frictional velocity dependencies that are close to velocity neutral: they can modulate both tectonic loading and the dynamic rupture process. Aftershocks can occur on compliant areas around a high slip patch, but most of the stress is diffused through aseismic slip.

In the following sections we will present and discuss the results of different simulations of dynamic crack propagation on a heterogeneous fault representing frictional heterogeneity in terms of a non-uniform distribution of either the L or B and A parameters.

3.2.1 Heterogeneous distribution of the L parameter

In this section we will present two numerical experiments in which we consider variable values of the characteristic length L along the fault; all models and constitutive parameters are listed in Table 3. We remind here that the L parameter controls the state variable evolution and affects the size of nucleation zone (equation (3.1)). Therefore, with the increasing L value, the fault spends a longer time to reach an extension equal to the critical length l_c and to initiate the spontaneous dynamic rupture propagation.

In Figure 2 we show results of numerical experiment in which a fault patch with $L = 9 \mu m$ is surrounded by a region with a greater L ($= 15 \mu m$). In panel 2a the spatio-temporal evolution is reported. In panel 2b we show histories of slip velocity for different points located along the fault. Figure 2 points out that the rupture penetrates within the region having a greater L .

As previously noted, during the propagation the peak slip velocity increases as the rupture front moves far away from the nucleation patch and, as soon as the crack tip encounters the region with a greater L , peak slip velocity is immediately reduced, but

even in this region it starts to grow again. As in the reference model, v_2 (i.e. the velocity at the new steady state) is almost the same for all points.

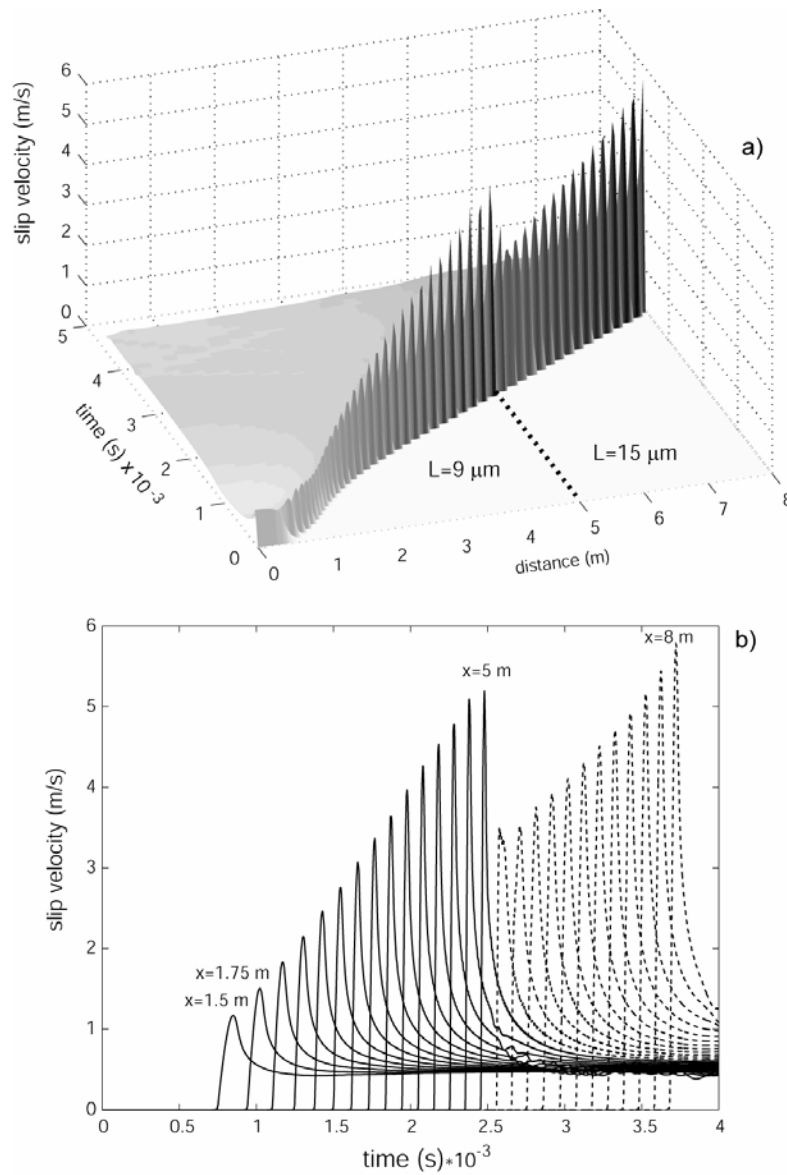


Figure 2: Dynamic rupture propagation along a heterogeneous fault: the adopted constitutive parameters are listed in Table 3. The fault is represented as two patches having different values of the L parameter (L_1 and L_3 in Table 3): the external one has a larger value (1.6 times the inner one). Top panel shows the spatio-temporal evolution of slip velocity. Bottom panel displays the time histories of slip velocity in different positions along the fault: solid lines identify slip velocity computed for those points located in the inner region (low L), while dashed lines identify slip velocity computed for those points located in the external region (high L).

We have plotted in Figure 3 the slip–weakening curves calculated for different points located along the fault strike for the same simulation shown in Figure 2.

Parameter	Heterogeneity of L (Figure 2-3)	Barrier-healing (Figure4)	Finite slip duration (Figure5)	Complex rupture propagation (Figure6)
$\lambda = \mu$	27 GPa	27 GPa	27 GPa	27 GPa
v_p	5196 m/s	5196 m/s	5196 m/s	5196 m/s
v_s	3000 m/s	3000 m/s	3000 m/s	3000 m/s
μ_0	0.56	0.56	0.56	0.56
a_1	0.012	0.012	0.015	0.014
a_2	0.012	0.012	0.015	0.015
a_3	0.012	0.012	0.012	0.012
b_1	0.016	0.016	0.014	0.016
b_2	0.016	0.016	0.014	0.013
b_3	0.016	0.016	0.016	0.016
$L_1=L_2$	1.5×10^{-5} m	1×10^{-3} m	1×10^{-5} m	1×10^{-5} m
L_3	0.9×10^{-5} m	1×10^{-5} m	1×10^{-5} m	1×10^{-5} m
x_1	5 m	5 m	7 m	6 m
x_2	5 m	5 m	7 m	4 m
σ_n^{eff}	100 MPa	100 MPa	100 MPa	100 MPa
v_{init}	1×10^{-5} m/s	1×10^{-5} m/s	1×10^{-5} m/s	1×10^{-5} m/s
Φ_{nucl}	1×10^{-4} s	1×10^{-4} s	1×10^{-4} s	1×10^{-4} s
$\Phi_{outside the nucleation}$	$\Phi^{ss}(v_{init})$	$\Phi^{ss}(v_{init})$	$\Phi^{ss}(v_{init})$	$\Phi^{ss}(v_{init})$
τ_0	$\tau^{ss}(v_{init})$	$\tau^{ss}(v_{init})$	$\tau^{ss}(v_{init})$	$\tau^{ss}(v_{init})$
Nucleation region	[-1.5 m, 1.5 m]	[-1.5 m, 1.5 m]	[-1.5 m, 1.5 m]	[-1.5 m, 1.5 m]
Δx_1	0.01 m	0.01 m	0.01 m	0.01 m
Fault region	[-10 m, 10 m]	[-10m, 10m]	[-50 m, 50m]	[-50 m, 50m]

Table 3. Model and constitutive parameters used for the simulations on a heterogeneous fault.

Because the state variable evolution is different for different values of the L parameter, the dynamic traction also displays a quite diverse behavior. When the rupture enters the region characterized by a greater L , the value of D_c^{eq} and consequently the fracture energy increase. Thus, Figure 3 corroborates the linear relation existing between the equivalent slip weakening distance D_c^{eq} and the L parameter (equation (1.9)). The kinetic friction level is nearly the same in the two regions. We emphasize that the slip-weakening curves maintain the expected trend also during the propagation along a heterogeneous fault but the dynamic physical

quantities (such as dynamic stress drop or fracture energy) depend on the constitutive parameters. The simulation presented above is characterized by a small contrast of the L parameter in the two regions. We show in Figure 4 the results of a numerical experiment in which the variation of L is more pronounced: we simulate the dynamic propagation along a fault where the inner region has $L = 10 \mu m$ and the external region has a higher L value ($L = 1 mm$). In this case the rupture is unable to penetrate the external patch. This configuration has been named “barrier model“ by Bizzarri et al. (2001). In fact, we observe that during the propagation within the inner region the rupture behavior is identical to the reference configuration (Figure 2a Chapter 1).

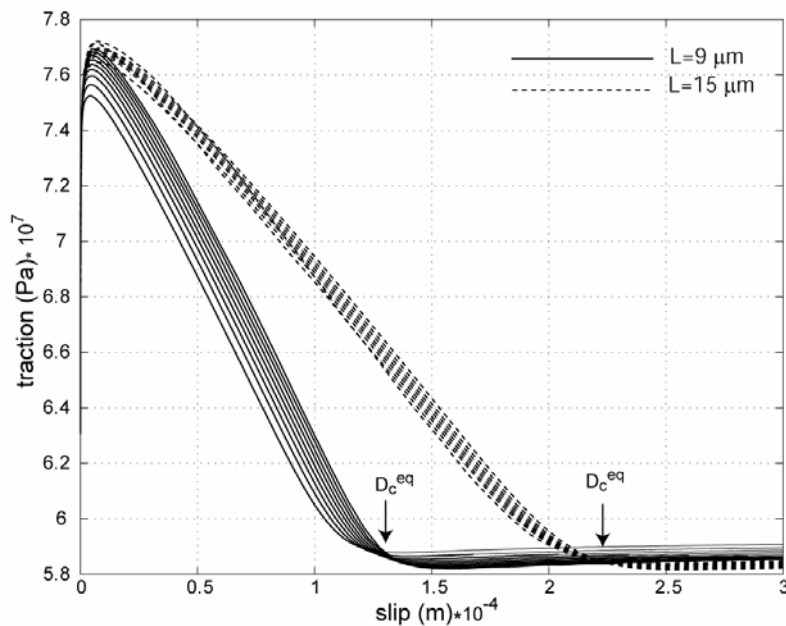


Figure 3: Slip-weakening curves calculated for the simulation shown in the previous figure, whose model and constitutive parameters are listed in Table 3. The traction evolutions as a function of slip have been plotted for several points located on the two patches having different values of L parameter at different distances from the nucleation patch.

When the rupture front approaches the high- L region (L is $1 mm$, thus the contrast is 1000), a back-propagating healing front causes the crack arrest, as the rupture does not have enough energy to break the barrier and propagate inside the high- L area. This process is known as a “barrier-healing“. Slip velocity time histories of different fault points are plotted in Figure 4b: we can clearly observe the increase of the peak as rupture propagates away from the nucleation patch. The back propagating front

causes a remarkable decrease of the slip velocity with a consequent healing. In this case our simulation yields a slip velocity time history with a finite duration.

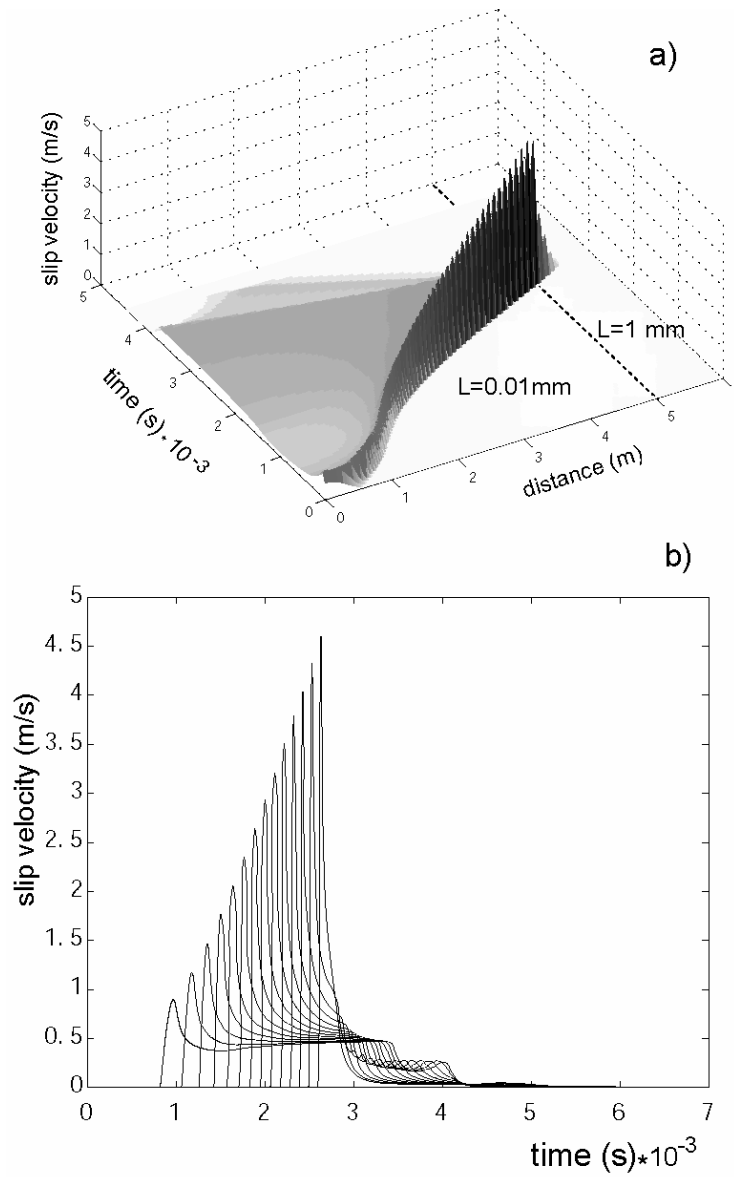


Figure 4: Dynamic rupture propagation along a heterogeneous fault: the adopted constitutive parameters are listed in Table 3. The fault is represented as two patches having different values of the L parameter (L_1 and L_3 in Table 3): the external one has a larger value (1000 times the inner one). Top panel shows the spatio-temporal evolution of slip velocity. Bottom panel displays the time histories of slip velocity in different positions along the fault.

3.2.2 Heterogeneous distribution of the $(B - A)$ parameter

In this section we will present and discuss some numerical experiments in which a velocity weakening zone is surrounded by velocity strengthening region. In the first simulation we compute the dynamic propagation of an earthquake rupture along a fault on which a velocity weakening patch is adjacent to a velocity strengthening region. The initial and constitutive parameters are listed in Table 3.

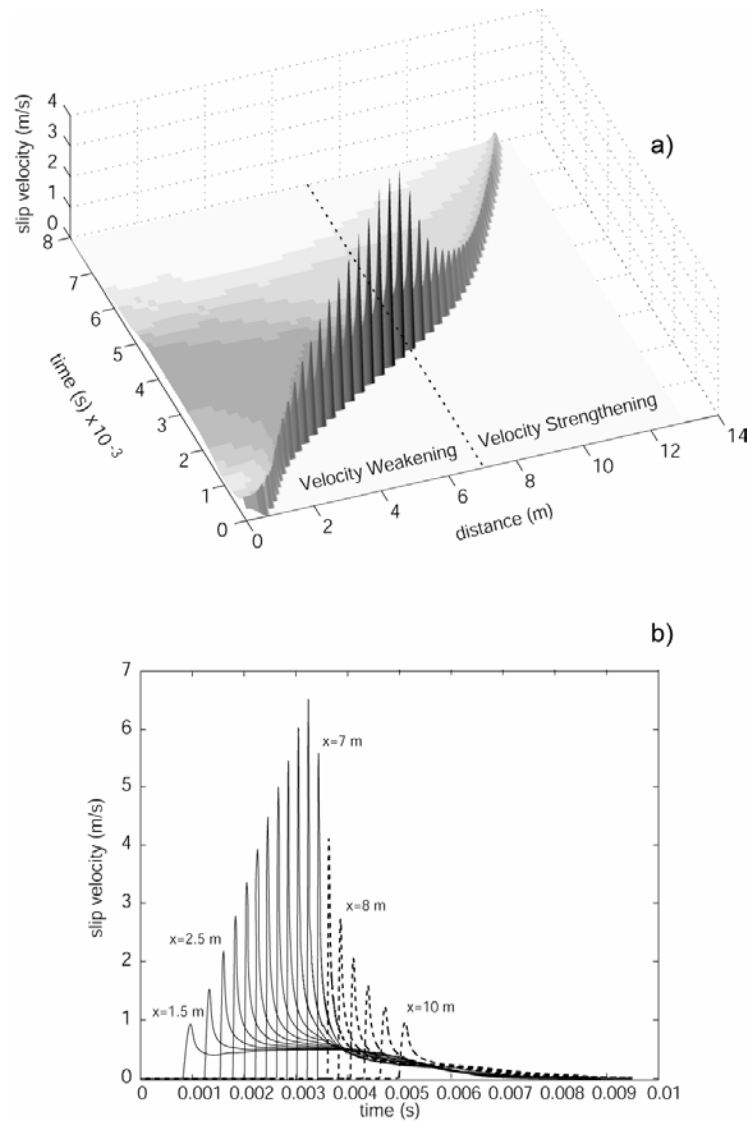


Figure 5: Dynamic rupture propagation along a heterogeneous fault: the adopted constitutive parameters are listed in Table 3. The fault is represented as two patches having different values of a and b parameters (a_1, b_1 and a_3, b_3 in Table 3): a velocity strengthening area is adjacent to the velocity weakening patch where the rupture nucleates. Top panel shows the spatio-temporal evolution of slip velocity. Bottom panel displays the time histories of slip velocity in different positions along the fault.

Figure 5 shows the results of these calculations: the dynamic rupture nucleates and propagates within the velocity weakening zone, thus it penetrates within the velocity strengthening region for a small distance before being arrested. The rupture arrest is gradual and it generates healing of slip only when rupture is stopped inside the VS region. In panel b we plot the slip velocity time histories, which show the expected behavior (similar to that one of Figure 3 Chapter 1) until the crack tip penetrates within the VS zone; thus, peak slip velocity gradually decreases and heals. Figure 6 shows the results of a numerical experiment in which two VW regions are separated by a VS patch located between them. The initial and constitutive parameters are listed in Table 3. As expected, the rupture initially accelerates within the VW region and it partially penetrates within VS area. Slip velocity is progressively attenuated and the crack tip decelerates.

In this area, the rupture velocity is very low and the crack is almost arrested. Because of the small dimension of the VS region, the crack is able to propagate within the VS patch and it re-accelerates again when it reaches the external VW region. Figure 6b shows the time histories of the slip velocity. It emerges that slip velocity has a finite duration only during the rupture propagation within the internal VW region, while in the external VW region it does not return to zero (i.e., no healing of slip).

These simplistic simulations provide a picture of the complex interactions between fault patches having different frictional properties. Our 2-D simulations illustrate how the traction and slip velocity evolutions are modified during the propagation on heterogeneous faults. These calculations propose stimulating implications for slip duration and fracture energy. We will discuss these issues in the following sections.

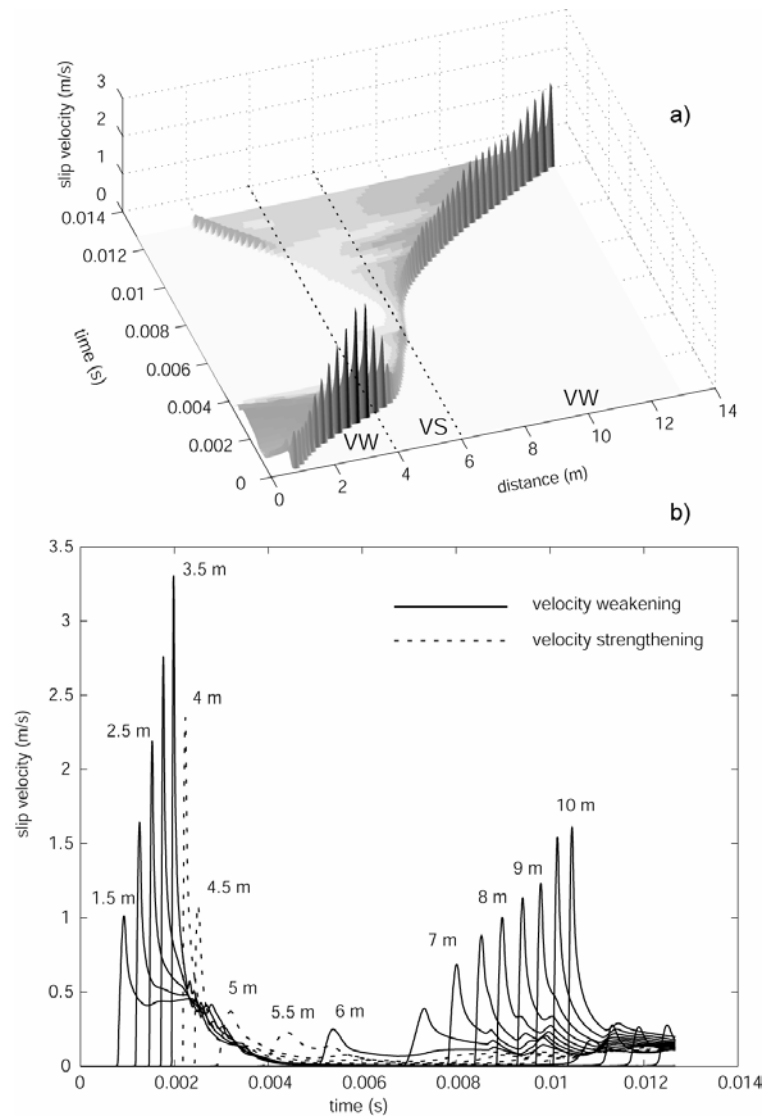


Figure 6: Dynamic rupture propagation along a heterogeneous fault: the adopted constitutive parameters are listed in Table 3. A narrow velocity strengthening patch separates two velocity weakening areas (identified by the values of the parameters (a_1, b_1, a_2, b_2 and a_3, b_3 in Table 3)). The rupture nucleates within the inner velocity weakening patch. Top panel shows the spatio-temporal evolution of slip velocity. Bottom panel displays the time histories of slip velocity in different positions along the fault.

3.3 Implications for slip duration

The simulations presented in the Chapter 1 confirm that the dynamic rupture propagation on a homogeneous fault governed by a R&S friction law (the slowness formulation defined in equation (1.6)) does not show the healing of slip (as clearly shown in Figures 2 and 4). This is in agreement with the results of Perrin et al.

(1995) and Bizzarri et al. (2001). Although different regularizations or modifications of the constitutive formulations have been proposed to get the healing of slip and/or self-healing pulses (see Chapter 2), even source heterogeneities can produce a finite duration of slip velocity and short slip durations (see Beroza and Mikumo, 1996; Day et al., 1998). In the present Chapter we have tested two different heterogeneous configurations; the first is based on the variation of the L parameter and the other on the interaction between VW and VS patches represented by changing the values of A and B .

A strong contrast of the L parameter represents a barrier and produces a “barrier healing” (see Zheng and Rice, 1998; Bizzarri et al., 2001) similarly to the arrest on the crack-like rupture propagation. Figure 4 shows that the slip duration depends on the distance from the barrier and it is shorter for closer distances. On the contrary, the interaction between VW and VS yields a finite slip durations (see Figure 5), but the spatio-temporal distribution of slip velocity does not resemble a self-healing pulse. In other words, while we have simulated finite and relatively short slip durations, we are unable to generate self-healing pulses. These results are consistent with the findings of Perrin et al. (1995) and corroborate the outcomes of Day et al. (1998), who suggested that source heterogeneity yields healing of slip. An important implication emerging from these results is that healing of slip does not require traction re-strengthening: total dynamic traction remains at the kinetic friction level also when slip velocity tends to zero.

3.4 Implications for fracture energy

We have computed fracture energy for the different simulations performed in this study. The fracture energy is defined as the amount of energy that the crack spends to advance and increase its length. It has been defined as:

$$G = \frac{1}{2} \int_0^{+\infty} (\tau - \tau_f) du \quad (3.2)$$

and it is measured as the area below the traction versus slip curve shown in Figure 3 and above the minimum traction τ_f . For a dynamic rupture propagation on a

homogeneous fault governed by a SW law the fracture energy G is constant and known *a priori* over the whole fault surface ($G=1/2(\tau_u-\tau_j)D_c$). This is not the case when rupture propagation is governed by other constitutive laws or when the constitutive parameters are not uniform on the fault.

In order to quantify the fracture energy changes during the crack growth, we plot in Figure 7 the computed G as a function of the position along the fault for four different configurations investigated in this study. Figure 7a shows the resulting values for the homogeneous configuration (the reference model shown in Figure 1), which reveals an increasing trend as the rupture propagates far away from the nucleation patch. Figure 7b, -c, and -d displays the resulting values computed for three heterogeneous configurations. In particular, Figure 7b corresponds to the non-uniform L distribution: as the rupture penetrates in the region with higher L , the computed fracture energy increases by a sudden jump to a larger value as expected from the results shown in Figure 3.

Figure 10c refers to the rupture arrest within a VS area shown in Figure 5: after an initial increase of G with increasing distance from the nucleation patch, we notice a decrease of G within the VS area. Finally, Figure 7d shows the fracture energy estimated in different fault positions during the rupture propagation in the heterogeneous fault modeled in Figure 6: the propagation within the VS area produces a sudden drop in G , which is followed by an increase when it starts to propagate again within the external VW region.

The calculations summarized in Figure 7 point out that frictional heterogeneity explains the variability of fracture energy on the fault plane, which is associated to both the variations of slip and breakdown stress drop.

Our estimates of fracture energy are related to dynamic fault model in a laboratory scale. There still are uncertainties about the real values of fracture energy for actual faults. We will see in detail the fracture energy values computed for real earthquakes in Chapter 6.

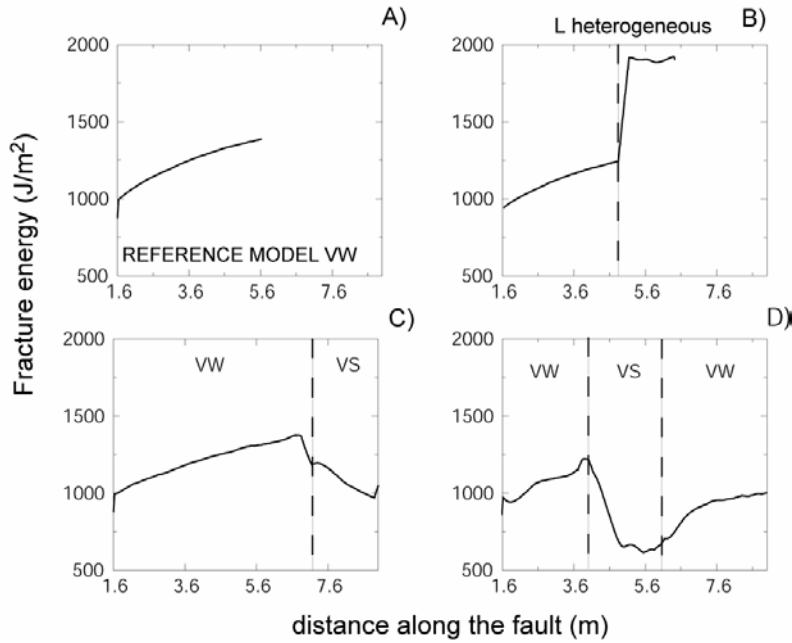


Figure 7: Fracture energy values in different positions along the fault for four configurations investigated in this study: (a) refers to the reference model shown in Figure 1; (b) refers to the heterogeneous L distribution shown in Figures 5 and 6; (c) and (d) refer to the heterogeneous distribution of the a and b parameters shown in Figures 8 and 9, respectively.

3.5 Conclusive remarks

We extend the results of BC96 to investigate the dynamic rupture propagation on a 2-D fault with a heterogeneous distribution of constitutive parameters. We use the rate- and state-dependent formulations to characterize fault heterogeneities following the findings of BC96, who proposed to split the velocity weakening and the velocity strengthening regimes into four distinct frictional fields. Our results corroborate the conclusions of BC96 demonstrating that a velocity strengthening area can arrest as well as can be driven to a dynamic instability by an earthquake rupture propagating in the adjacent fault patch. We represent numerically the fault heterogeneity by assigning different values of L or $(B-A)$ parameters along the fault line. Our simulations show that the interaction between the propagating dynamic rupture front and the heterogeneous fault patches depends on the values of the constitutive parameters. In particular, we show that a variation of the L parameter can modify the peak slip velocity or can arrest the rupture propagation depending on the value of the

L contrast. The heterogeneity of the L parameter does not modify the breakdown stress drop neither contributes to the variations of rupture velocity if the contrast is smooth. On the contrary, the heterogeneity of the distribution of the difference ($B-A$) affects the dynamic rupture propagation in a more complex way: dynamic stress drop and strength excess strongly depend on B and A parameters. Moreover, rupture can penetrate within a velocity strengthening area and the heterogeneous distributions of B and A yield complex time histories of slip velocity.

We propose that frictional heterogeneities can explain the observed complexity of slip distribution and the variability of rupture velocity during earthquakes. Our results have important implications for slip durations (i.e., local rise time) and fracture energy. A large contrast in the L parameter represents a barrier that produces a crack-like solution with variable but finite slip durations. Because the variations of constitutive parameters affect both the critical slip-weakening distance (see Bizzarri and Cocco, 2003 and references therein) and the breakdown stress drop, the inferred fracture energy varies along the fault. We show that the increase of the L parameter results in a fracture energy increase and that heterogeneous distribution of ($B-A$) yields evident variations of fracture energy along the fault. Because we model here a laboratory fault, our estimates ($\sim 10^3$ J/m²) of fracture energy cannot be compared with those inferred for real earthquakes.

We mainly focus on the interactions between the propagating dynamic rupture front and the heterogeneous fault patches. According to BC96, the response of fault patches having different frictional properties to a constant tectonic load also controls the pattern of seismicity and the behavior of crustal faults. Thus, fault frictional properties and their variations on the fault plane play an important role in characterizing crustal faulting as well as the mechanical properties of major fault zones.

Chapter 4

Estimates of D_c for different dynamic rupture models

We have seen in previous chapters that the determination of the temporal evolution of dynamic traction within the cohesive zone during the propagation of an earthquake rupture is the major task of many recent investigations. Shortly, this evolution is characterized by the traction increase to the upper yield stress (τ_y), which is followed by a decrease to the kinetic friction level (τ_f), during a time interval that defines the duration of the breakdown process. The traction decrease (i.e., the weakening phase) is associated to the slip increase, resulting in the well known slip weakening behavior (Figure 1a). Slip weakening (SW) has been observed in laboratory experiments (Okubo and Dieterich, 1984; Ohnaka et al., 1987), it has been proposed in theoretical studies (Ohnaka, 2003 and references therein) and used in numerical simulations of earthquake ruptures. In the previous chapters we have also shown that slip weakening is a characteristic behavior of rate and state friction. Such a traction variation with slip must be common to any constitutive relation proposed to model rupture propagation. The slip weakening is a characteristic feature of the dynamic failure episode characterizing the breakdown process, but the traction drop with increasing slip is controlled by the physical processes governing the constitutive behavior. For this reason, the estimate of dynamic parameters (e.g., D_c , dynamic stress drop, fracture energy...) for real fault dimension is one of the major tasks for seismologists.

Many different approaches have been proposed to estimate the critical slip weakening distance (D_c) for real earthquakes. Most of them rely on the reconstruction of the traction evolution from kinematic rupture models (Ide and Takeo, 1997; Guatteri and Spudich 2000; Zhang et al., 2003). It seems, however, that some of the D_c values may be overestimated due to limited data resolution and may furthermore be biased by computational constraints or by the assumptions of

kinematic rupture model (see chapter 5 of this thesis). Recently, Mikumo et al. (2003) proposed a method to estimate the critical slip weakening distance from slip velocity functions. The theoretical demonstration of this method is discussed in Fukuyama et al. (2003). This approach is based on the estimate of the slip weakening distance at each point on the fault as the slip (D'_c) at the time of peak slip velocity (see Figure 1), supposing that the traction reaches its minimum value in that time. Fukuyama et al. (2003) have shown that the estimates of D'_c can be affected by an error of roughly 50%. The values of D_c proposed in the recent literature span from microns (laboratory experiments in Dieterich, 1979) to several meters (e.g. Zhang et al., 2003). This raises the question of the actual size of the critical slip weakening distance. In this chapter we present the results of different numerical simulations of the dynamic propagation of a 2-D in-plane crack obeying different constitutive laws. The goal is to discuss the retrieved slip velocity time histories to verify if the critical slip weakening distance can be estimated from the slip value at the peak slip velocity.

4.1 Simulations with a slip weakening law

Figure 1 illustrates the results of a 2-D simulation performed using the SW law (equation 1.8) and the input parameters listed in Table 1 (model A). Figure 1a and 1b show the total dynamic traction as a function of slip and slip velocity, respectively, for a target point on the fault; the former depicts the imposed constitutive law, while the latter is part of the solution of the spontaneous dynamic calculation.

Figure 1c shows the normalized time history of slip, slip velocity and total dynamic traction. This simulation reveals that the peak of slip velocity occurs exactly when the traction is at its minimum (i.e., the kinetic friction level), consistent with the Mikumo et al. (2003) findings. In the present study, we refer to the slip weakening distance inferred from the slip amplitude at the peak slip velocity as D'_c , following Fukuyama et al. (2003) and Spudich and Guatteri (2004).

As expected, for this simulation D'_c (0.1 m) matches the D_c value assigned as input parameter in the numerical calculation. Because of the low strength value adopted in this simulation ($S = 0.8$, where S is the strength parameter defined by Das and Aki, 1977), the rupture speed becomes super-shear and the resulting peak slip velocity is very high.

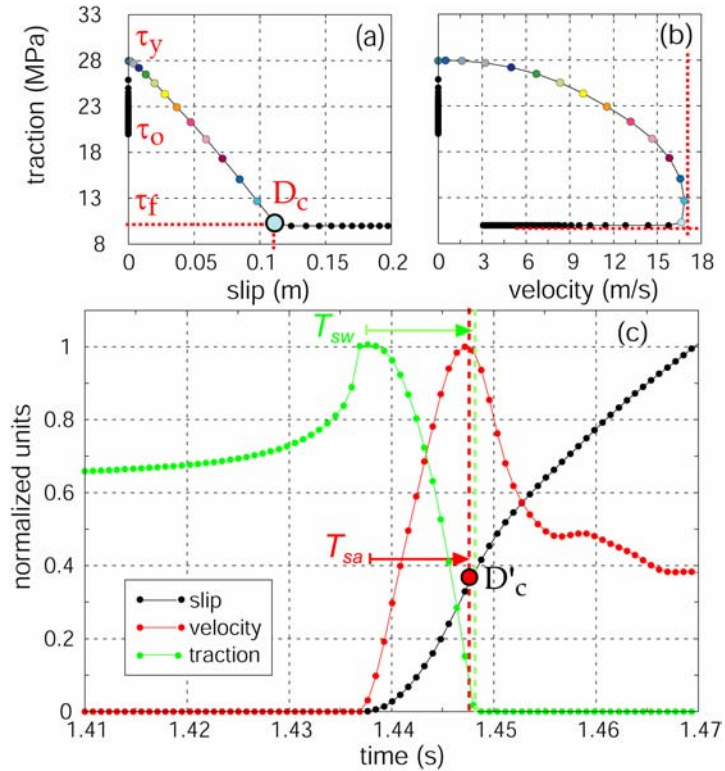


Figure 1: Traction versus slip (a) and slip velocity (b) calculated for a 2-D in-plane crack obeying a SW law for a target point located 5 km from the nucleation. The parameters adopted in this simulation are listed in Table 1 (Model A). Colors are used to depict the temporal evolution. (c) normalized time histories of total dynamic traction, slip velocity and slip. The dashed lines in (b) emphasize that peak slip velocity is reached when traction is at its minimum value.

The time coincidence between the peak of slip velocity and the minimum traction implies that the temporal duration of slip weakening phase (T_{sw}) is equal to the duration of slip acceleration phase (T_{sa}), as shown in Figure 1. In other words, the slip acceleration during the weakening phase is always positive. Because this should rely on the fault constitutive properties, in this chapter we investigate whether this behavior is common in constitutive formulations other than SW, widely adopted in the literature.

<u>Model A – SW [S=0.8]</u>	<u>Model B – R&S</u>	<u>Model C –SW [S = 1.5]</u>
$\sigma_n^{eff}=30$ MPa	$\sigma_n^{eff} = 100$ MPa	$\sigma_n^{eff} = 30$ MPa
$\tau_0 = 20$ MPa	$a = 0.013$	$\tau_0 = 20$ MPa
$\tau_y = 28$ MPa	$b = 0.017$	$\tau_y = 24.5$ MPa
$\tau_f = 10$ MPa	$L = 10^{-5}$ m	$\tau_f = 17.7$ MPa
$D_c = 0.1$ m	$\Psi_{init} = 1s; V_{init} = 10^{-5}$ m/s	$D_c = 0.1$ m
$\rho = 2700 \text{Kg/m}^3; Vp = 5196 \text{m/s}; Vs = 3000 \text{m/s}$		

Table 1. Medium and constitutive parameters.

4.2 Simulations with rate and state laws

We present the results of several simulations performed to model the spontaneous dynamic propagation of a 2-D in-plane crack obeying to the R&S law (equation 1.6). Figure 2a shows the normalized time histories of slip, slip velocity, traction and state variable for the reference model presented in chapter 1. This set of parameters is based on laboratory experiments results. For this simulation D_c inferred from the traction versus slip curve is 0.16 mm. This figure clearly points out that the peak of slip velocity occurs well before that the traction reaches the kinematic stress level. This is also evident looking at the phase diagram displayed in the inset of Figure 2a, that shows a stage in which both slip velocity and traction decrease (C-D in Figure 2a). In this case, the value of D'_c is 0.085 mm, roughly 50% of D_c . Because we are interested here only to relative differences between D_c and D'_c , we do not face the problem of scaling the laboratory values to real fault dimensions. The friction law controls the evolution of slip velocity and the timing of its peak.

4.2.1. The direct effect of friction

In chapter 2 we have performed many different simulations by changing the constitutive parameters. We discuss here again the effect of changing the parameter a controlling the direct effect of friction in equation (1.6) with the intent of estimating the D_c values. Figure 2b shows the time histories of the relevant physical

quantities calculated for the same set of parameters used in Figure 2a, but using a smaller value of the a parameter (0.010).

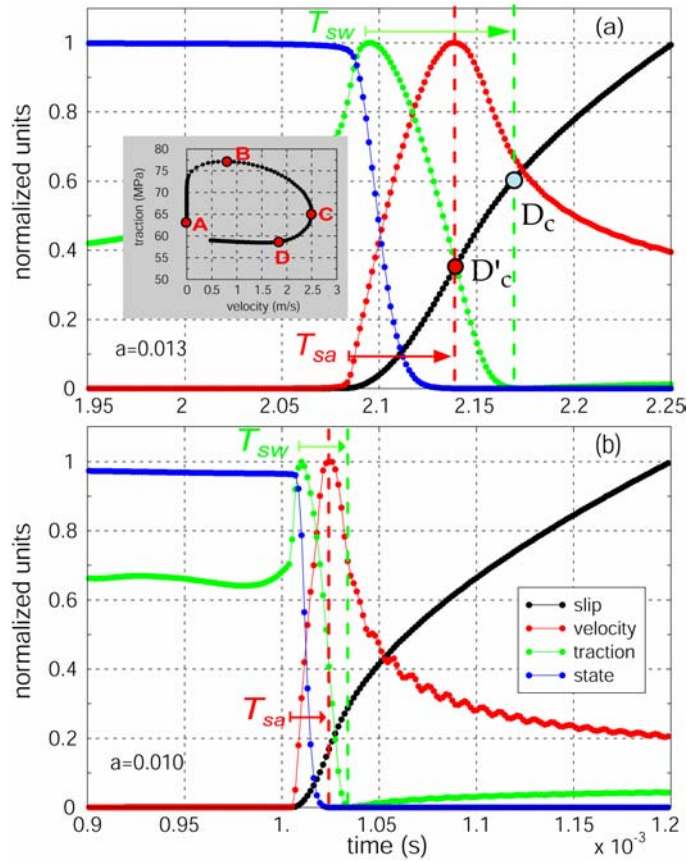


Figure 2: Normalized time histories of state variable, slip, slip velocity and total dynamic traction computed for a 2-D in-plane crack obeying R&S friction. The inset in panel (a) displays the traction as a function of slip velocity (phase diagram). The constitutive parameters used in these simulations are listed in Table 1 (Model B). (b) same as above with a smaller value of a parameter (0.010). Capital letters identify the different stage of the breakdown process.

In this case the timing of peak slip velocity is still not coincident with the time at which the traction reaches the kinetic level, but their difference is smaller than that shown in Figure 2a. In this simulation D_c is 0.18 mm, while D'_c is 0.12 mm. Our numerical results suggest that the direct effect of friction controls the occurrence and the amplitude of slip velocity peaks. However, we have to remark that, by reducing the parameter a , we change both the yield and the kinetic stress values as discussed by Bizzarri and Cocco (2003).

4.2.2. Friction behavior at high slip rates

The previous results motivated a further test. We have performed several simulations modifying the friction behavior at high slip rates defined by equation (1.6). As explained in chapter 2, we have assumed that, when the slip velocity exceeds a fixed threshold (V_{cut}), the direct friction term $[\ln(V^*/V)]$ in equation (1.6) is frozen and taken constant $[\ln(V^*/V_{cut})]$ (Weeks, 1993). This implies that for $V > V_{cut}$ the governing equation (1.6) does not directly depend on slip velocity, although the dependence on slip rate is still present in the state variable evolution. We show in Figure 3 the results of two simulations performed by using the parameters listed in Table 1 (Model B), with $a = 0.012$ and two different values of V_{cut} . In panel (a) the slip velocity cutoff is slightly larger than the initial velocity ($V_{cut} = 2 V_{init}$); therefore, the direct effect of friction is constant for most of the simulation. On the contrary, in panel (b) V_{cut} is two orders of magnitude larger ($200 V_{init}$).

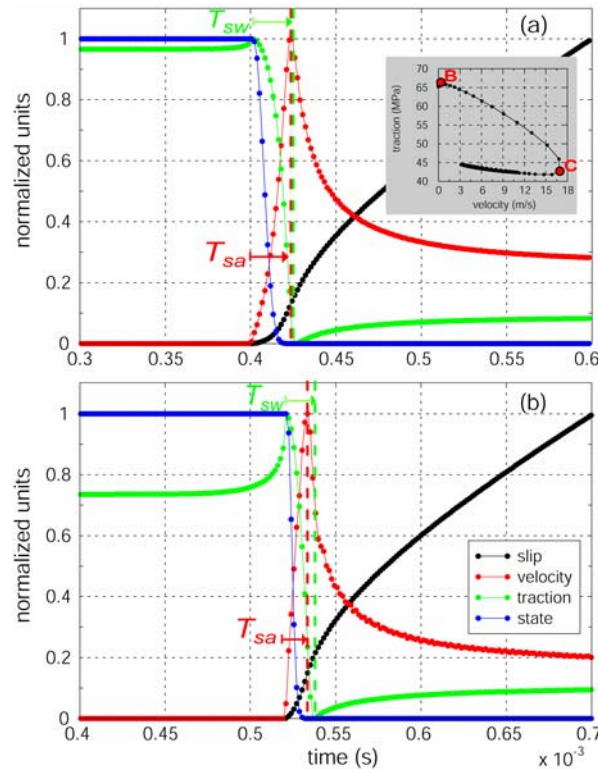


Figure 3: Normalized time histories of state variable, slip, slip velocity and total dynamic traction computed with model B of Table 1 and a slip velocity cut-off (V_{cut}) on friction at high slip rates. In Panel (a) V_{cut} is $2 \cdot 10^{-5}$ m/s, slightly larger than the initial velocity ($1 \cdot 10^{-5}$ m/s), while in panel (b) V_{cut} is $2 \cdot 10^{-3}$ m/s. The inset in panel (a) shows the associated phase diagram.

This figure shows that the direct effect of friction modifies the phase diagram reducing the velocity-hardening phase. In this case, the peak slip velocity occurs at the end of the weakening phase, when traction reaches the kinetic stress level and slip is equal to the critical distance.

When the velocity dependence of the direct effect of friction is eliminated, the phase diagrams display a nearly linear decay (inset of Figure 3a). On the contrary, if the slip rate controls the direct effect, the phase diagram is more elliptic and the velocity-hardening phase is more pronounced (inset of Figure 2a).

Our simulations point out that the peak of slip velocity and the minimum traction are reached at similar times if the direct effect of friction is taken constant; this is also evident looking at the phase diagram displayed in the inset of panel (a). The critical slip distances inferred from the simulation shown in Figure 3a are $D_c = 0.23$ mm and $D'_c = 0.18$ mm.

4.3. Conclusive remarks

The simulations discussed above demonstrate that using R&S dependent laws, the slip velocity evolution is controlled by the adopted friction law, its behavior at high slip rates and the constitutive parameters. We will show here that also using a SW law the timing of peak slip velocity depends on the assumed constitutive parameters. The simulation shown in Figure 1 is representative of a relatively low-strength fault ($S = 0.8$). For the homogeneous configuration here considered, this implies that during propagation, the rupture accelerates to super-shear speeds. We show in Figure 4 the results of another simulation performed using a SW law with a higher strength parameter ($S = 1.5$). The model parameters are listed in Table 1 (Model C). In this case the rupture velocity is sub-shear. Figure 4 displays the time evolution of the normalized physical quantities and points out that peak of slip velocity occurs before the traction reaches its minimum. The inferred difference between D_c and D'_c is slightly less than 30%.

Our simulations demonstrate that the phase diagrams reflect the differences between D_c and D'_c . In particular, when the peak of slip velocity is simultaneous with the

minimum traction, the phase diagram consists of extremely fast slip acceleration (the portions A-B and C-D in Figure 2a shrink).

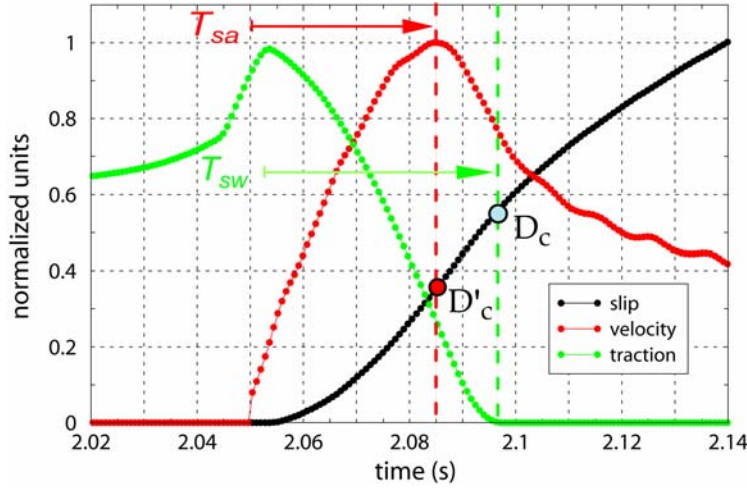


Figure 4: Normalized time histories of total dynamic traction, slip velocity and slip for a calculation performed with a SW law and the model parameters listed in Table 1 (Model C). The strength value (1.5) is larger than that of Figure 1 (0.8).

This is evident comparing Figure 1b and the inset in Figure 3a with the phase diagram shown in Figure 2a. Fukuyama and Madariaga (1998) proposed the following boundary condition relating traction $[\tau]$ to slip velocity $[V]$ on the fault plane:

$$\sigma(x, t) = \frac{\mu}{2V_s} V(x, t) + \int_{\Sigma} \int_0^t K(x - \xi; t - t') V(\xi, t') dt' dS \quad (4.1)$$

where μ and V_s are the rigidity and the shear wave velocity, respectively. K is the integration kernel, which accounts for the contribution of the past slip history. This relation is independent of the constitutive law, although friction controls the slip velocity function included in (4.1). Equation (4.1) is useful to interpret our results and the different phase diagrams obtained in this study. The phase diagrams shown in Figures 1 and 3 are characterized by large values of slip velocity and, as a consequence, by large values of dynamic load due to previous slip history [i.e., the integral term in (4.1)]. In these conditions, we find that $D_c \sim D'_c$. We have to emphasize however that these simulations yield unrealistic values of slip velocity. On the contrary, the shape of the phase diagram shown in Figure 2a is characterized

by smaller contributions of the dynamic load and a reduced slip acceleration. In this case, we found that D'_c is 50% of D_c .

The results obtained in this chapter generalize the Fukuyama et al. (2003) conclusions. We show that the variability of fault constitutive properties can explain the observed differences between D'_c and D_c . Spudich and Guatteri (2003) tested the accuracy of D'_c estimates and found that low pass filtering of slip models can bias the inferred values causing an artificial correlation between D'_c and total slip. In our calculations the peak slip velocity always occurs within the breakdown time and then D'_c is smaller than D_c .

Therefore the estimated value of the parameter D'_c is affected by the friction law and the constitutive parameters, which control the slip acceleration and the traction drop during the breakdown time. The differences found in this study between D'_c and D_c can vary from few percent up to 50%, in agreement with Fukuyama et al. (2003). Although the biases pointed out by Guatteri and Spudich (2000) and Spudich and Guatteri (2003) might represent a limitation to constrain the actual critical slip weakening distance, the estimate of D'_c might be still useful if we accept the idea that D_c can range over several order of magnitudes. In this case an error of 50% in D'_c , can still allow us to constrain the size of the critical slip weakening distance.

We have seen in these four chapters the difficulty in describing all the competing processes affecting earthquake dynamics that still need the definition of a constitutive law. Besides, there are still open questions concerning the problem of bridging laboratory and seismological estimates of length-scale parameters. These doubts raise important issues which affect the estimate of fracture energy and the earthquake energy balance.

Our results stimulate further investigations of the actual values of dynamic parameters and motivate the second part of this thesis.

Part II:

***Link between dynamic and kinematic
representations of earthquake rupture***

Chapter 5

Inference of dynamic parameters from kinematic models

5.1 Background

The space and time history of shear stress produced on the fault plane during an earthquake rupture has been explored by several recent studies (Bouchon et al., 1998; Dalguer et al., 2002; Zhang et al., 2003; Day et al., 1998). The dynamic traction evolution is commonly inferred from kinematic rupture models with the ambition to constrain the fault constitutive behavior (Ide and Takeo, 1997; Guatteri and Spudich, 2000).

Kinematic rupture models for moderate to large earthquakes are currently obtained by inverting ground motion waveforms, which provide a detailed image of the slip history during the rupture process (e.g. Hartzell and Heaton, 1983; Fukuyama and Irikura, 1986; Takeo, 1987; Beroza and Spudich, 1988; Yoshida and Koketsu, 1990; Wald and Heaton, 1994; Yoshida et al., 1996; Cotton and Campillo, 1995; Yagi and Kikuchi, 2000; Bouchon, et al., 2000; Sekiguchi and Iwata, 2002 among many others). One fundamental purpose of these inverse modeling attempts is to improve our understanding of the physical processes governing dynamic rupture propagation and the seismic wave generation. It is still an important task to distinguish between different slip models characterized by a propagating slip pulse (Heaton, 1990; Zheng and Rice, 1998) or a crack-like rupture growth (Das and Aki, 1977; Day 1982). Kinematic source models retrieved through the inversion of seismological and geodetic data have shown that large slip patches are usually a small fraction of total rupture area. Slip heterogeneity and rupture complexities are probably generated by a combination of different factors such as non-uniform initial stress distributions, non-planar fault geometry and heterogeneous distribution of constitutive properties of the fault as well as of the elastic properties of the crust.

Several assumptions are needed to constrain the rupture history of an earthquake and to infer a unique kinematic source model whose simulated waveforms have reasonable fit to observations. The temporal evolution of slip on the fault plane is obtained either by assuming an analytical expression for the source time function (single window inversion) or by assuming that each fault point can slip more than once (multi-window inversion). The latter provides the slip time history as part of the solution, although the temporal resolution of the retrieved kinematic model is rather low, while the former imposes a priori the source time function. Because the temporal evolution of dynamic traction on the fault plane is retrieved by the slip time history, the choice of the source time function might affect the inferred dynamic parameters. This is the main motivation of the present chapter.

Most of these investigations solve the elasto-dynamic equation to compute the dynamic traction at selected points on the fault plane, where the kinematic model is supposedly well resolved.

The traction evolution allows the calculation of dynamic stress drop and strength excess on the assumed fault plane (*Mikumo and Miyatake, 1995; Bouchon, 1997*) as well as the estimate of the critical slip weakening distance (D_c). For instance, *Ide and Takeo (1997)* evaluated values of D_c ranging between 50 and 100 cm for the 1995 Kobe earthquake. Several other recent studies have inferred in similar ways values of the slip weakening distance ranging between 20% and 90% of the total final slip (*Pulido and Irikura, 2000; Guatteri et al., 2001; Peyrat et al., 2001*). Moreover, an unexplained correlation between the total slip and the inferred D_c values has been obtained by some investigators (*Zhang et al., 2003*). In this chapter we aim to understand if the source time functions adopted in kinematic models can bias the retrieved dynamic parameters and partially explain the variability of D_c estimates. *Guatteri and Spudich (2000)* also emphasized the limitations in estimating the critical slip weakening distance by modeling ground motion waveforms. In particular, they concluded that both the adoption of spatial and temporal smoothing constraints in the formulation of the inverse problem and the modeling of low-frequency seismic waves can bias the inferred values of D_c . Here we face the same problem from a different point of

view. The values of the critical slip weakening distance computed from kinematic inversions and ground motion modeling are two order of magnitude larger than those inferred in laboratory experiments (Okubo and Dieterich, 1984; Ohnaka and Yamashita, 1989) or used in numerical simulations performed with laboratory-derived constitutive laws (Cocco and Bizzarri, 2002, and Bizzarri and Cocco, 2003). This means that there is still an open debate within the scientific community on the actual size of the critical slip weakening distance, as we have underlined in the previous chapter. We aim to contribute to this debate by estimating the dependence of traction evolution on the source time function chosen to model ground motion waveforms.

5.2 Methodology

We use a 3-D finite difference dynamic code to calculate the stress time history on the earthquake fault plane (Andrews, 1999). The stress is computed through the fundamental elasto-dynamic equation (Ide and Takeo, 1997). The total dynamic traction in each fault position is calculated by the sum of two contributions: the instantaneous term depending on slip velocity and the dynamic load related to the previous slip history. This explicit dependence has been found analytically by Fukuyama and Madariaga (1998). Their inferred equation is the following:

$$\sigma(x, t) = \frac{\mu}{2V_s} S(x, t) + \int_{\Sigma} \int_0^t K(x - \xi; t - t') S(\xi, t') dt' dS \quad (5.1)$$

where $S(x, t)$ represents the slip velocity, V_s the shear velocity, μ the rigidity, K the dynamic load associated to those points that are still slipping. The equation (5.1) has been already described in the previous chapter [see equation (4.1)]. We show this formulation only to highlight the direct effect of the local source time function on the corresponding traction evolution. In the present study we impose the slip velocity as a boundary condition. In other words, each node belonging to the fault plane is forced to move with a prescribed slip velocity time history. In this way we do not need to specify any constitutive relation and the dynamic

traction evolution is a result of the calculations. The space and time distribution of slip velocity (S) is derived from an input kinematic rupture model.

5.3 Dependence of traction evolution on source time function adopted in kinematic rupture models

In this section, we study the effects on traction evolution due to the adoption of an analytical expression of source time function, typically used for single time-window inversion procedure. We use different slip velocity distributions, defined as

$$S(\xi, t) = \dot{f}(t - t_R(\xi)) \cdot D_{\max}(\xi), \quad (5.2)$$

by adopting different source time functions $\dot{f}(t)$ (whose unit is s^{-1}) for a given distribution of final slip $D_{\max}(\xi)$. In (5.2) $\xi=(\xi_1, \xi_2)$ represents the local coordinates on the fault plane, t is time and $t_R(\xi)$ the rupture time. This means that the shape of the slip velocity function all over the fault is chosen *a priori*, while the rupture time and the slip amplitude can vary depending on the node position.

5.3.1. Adopted source time functions

In order to investigate the resulting dynamic traction evolution, we use three distinct source time functions $\dot{f}(t)$ characterizing slip velocity, which have the following analytical forms:

$$f_1 = \dot{f}(t) = H(t) \frac{2}{\tau_R} \left[1 - \tanh^2 \left(\frac{2}{\tau_R} \left(2t - \frac{3}{2} \tau_R \right) \right) \right] \quad (5.3a)$$

$$f_2 = \dot{f}(t) = H(t) \frac{2}{\tau_R} e^{-\frac{2t}{\tau_R}} \quad (5.3b)$$

$$f_{3,4} = \dot{f}(t) = H(t) H(\tau_R - t) \frac{2}{\pi \tau_R} \left(\frac{-t + \tau_R}{t} \right)^{1/2} \quad (5.3c)$$

In these equations $H(t)$ is the Heaviside function, t_R is equal to zero, τ_R is the rise time and the others quantities are defined above. These relations define source time functions already known in the literature: (5.3a) and (5.3b) are similar to those used by Cotton and Campillo (1995) in their kinematic inversion method, while (5.3c) has been proposed by Nielsen and Madariaga (2003) [they derived this function from the steady-state solutions of Freund (1979) and Broberg, (1999)]. Nielsen and Madariaga (2003) have demonstrated that function (5.3c) is obtained either in steady-state or self-similar model solutions and that it is compatible with a constant frictional level inside the slipping area.

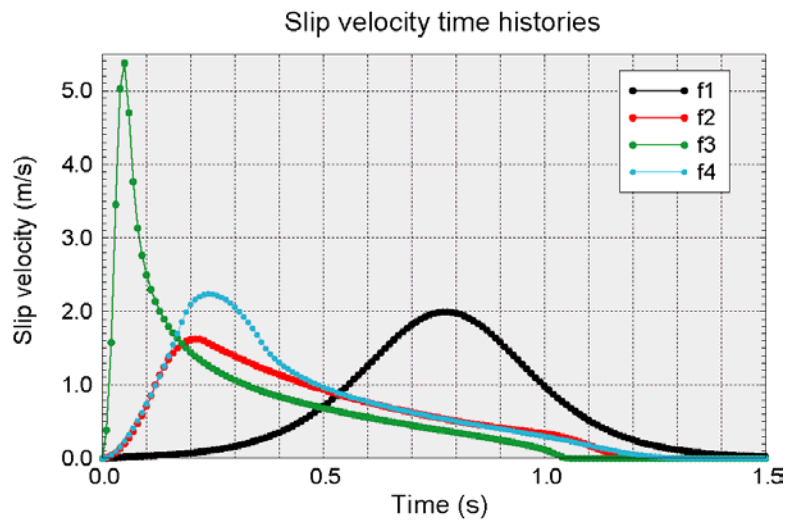


Figure 1: Slip velocity time histories: the numerical representation of analytical relations defined in equations (5.3) is obtained by smoothing in time the functions with a triangular window of different widths to avoid the singularity.

We emphasize that only the function (5.3c) is based on elasto-dynamic considerations. To avoid the singularity or discontinuity of some analytical relations, the numerical representation of $\dot{f}(t)$ is obtained by smoothing the functions in time: we convolve $\dot{f}(t)$ with a moving triangular window of assigned width. In particular, for function (5.3c) we use two smoothing windows with different durations of 0.07 s and 0.37 s; the corresponding functions are named in the following f_3 and f_4 , respectively. All the functions are normalized to have a unit integral over time. The slip velocity time histories defined above are shown in Figure 1. The function f_1 is characterized by a very smooth rupture onset; on the contrary, f_3 is characterized by an abrupt onset and a larger peak

value. Function f_2 has been truncated to impose the prescribed duration, function f_1 tends to zero exponentially, while function $f_{3,4}$ has an analytical expression with zero slip velocity at T_R . To simplify the analysis we have chosen the same rise time for all the time functions ($\tau_R=1$ s).

For our simulations, we assume a homogeneous half-space discretized with $\Delta x=\Delta y=\Delta z=100$ m grid cell size, $\Delta t=0.01$ s and an initial shear stress $\tau_0=20$ MPa; the density is $\rho = 2700$ kg/m³ and the body wave velocities are $V_P = 5.2$ km/s and $V_S = 3.0$ km/s.

5.3.2 Simulations with a uniform slip model

We perform our numerical simulations by assuming a rupture model similar to that proposed for the 2000 Western Tottori (Japan) earthquake ($M_w=6.8$) consisting of a vertical fault plane with a left lateral strike-slip motion (Fukuyama et al., 2003). The fault is 26 km long and 14.4 km wide (Figure 2a). We first consider a uniform slip model ($D_{\max} = 1$ m) characterized by a constant rupture velocity (2.0 km/s) and rise time (1s).

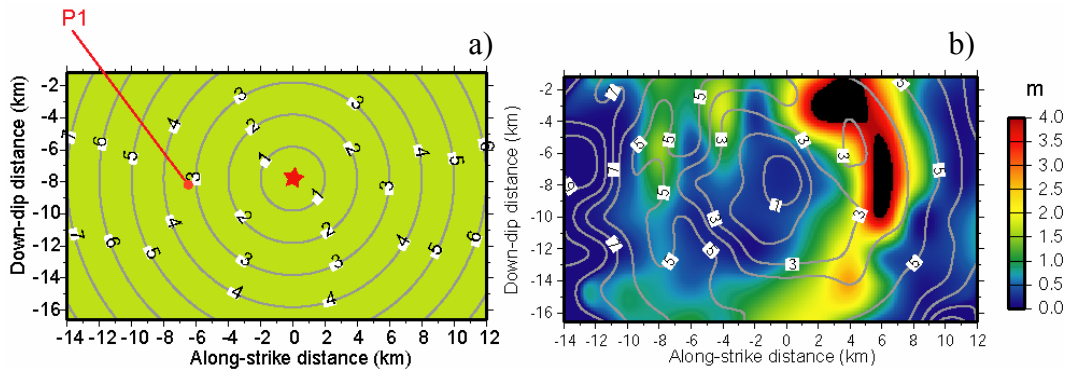


Figure 2: (a) Uniform slip model ($D_{\max}=1$ meter) and rupture velocity propagation ($V_r=2$ km/s) for rupture model similar to 2000 Western Tottori earthquake. (b) Heterogeneous slip and rupture time distribution on the fault plane for the 2000 Western Tottori earthquake inferred from Iwata and Sekiguchi (2001) model.

We therefore derive four kinematic models, which differ only in the adopted source time functions.

We start verifying how the source time function affects the simulated seismograms. We compare the synthetic ground velocities calculated at several

receivers by using these different kinematic models as input for the isochrones approach (Spudich and Xu, 2002). In Figure 3a and 3b we show the N-S component of ground velocity band-pass filtered between 0.1-1.5 Hz and 1.5-15 Hz for two stations with epicentral distances of 13 km and 37 km, respectively. We shift the temporal histories in the y-axis only to highlight the differences. We find that in the frequency band 0.1 - 2.0 Hz the simulated time histories are almost identical, while they differ in the high frequency band (1.5 - 15 Hz). In particular, the seismograms computed with f_3 have higher frequency content and larger peak velocities (roughly twice than the others). This simple test confirms that these rupture models are “kinematically” equivalent in the frequency band usually adopted in waveform inversions (0.05-1.5 Hz).

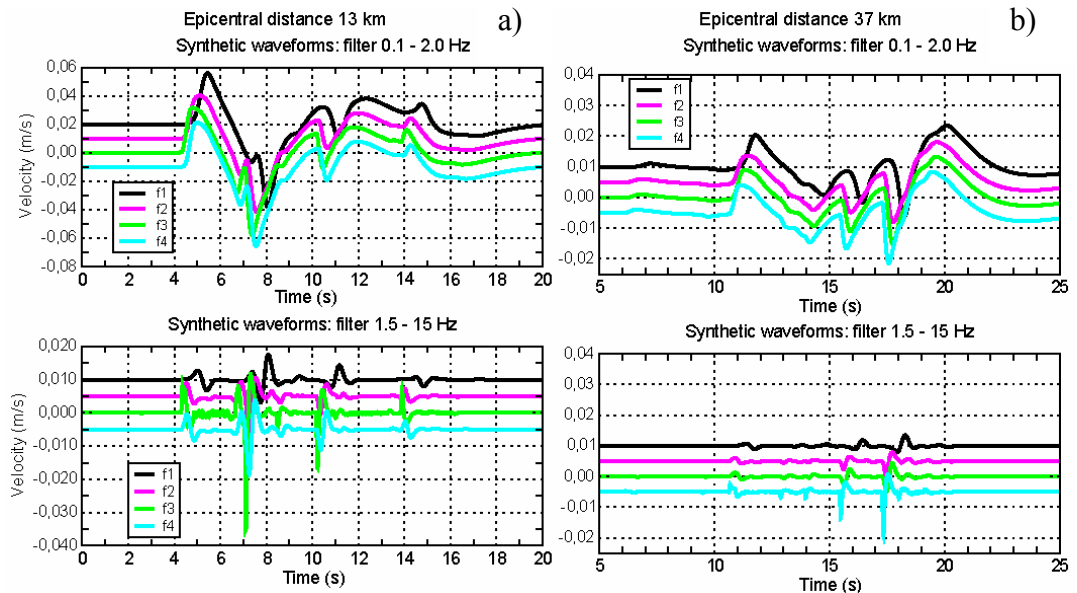


Figure 3: N-S components of synthetic ground velocities band-pass filtered between 0.1-1.5 Hz and 1.5-15 Hz computed at two stations with epicentral distance of 13 km (left panels) and 37 km (right panels).

The four adopted source models are the input parameters in our dynamic algorithm. Figure 4 shows the time history of slip, slip velocity and the resulting dynamic traction (left panels) as well as the traction as a function of slip (right panels) calculated for a particular target point shown in Figure 2a. Our numerical results illustrate that the traction evolution within the cohesive zone exhibits the slip weakening behavior, although the shape of the slip weakening curve strongly depends on the assumed source time function. The total dynamic traction shows

an evident restrengthening for all source models (healing of slip, see Figure 4). Our results show that the yield stress and the frictional stress amplitudes depend on the adopted source time function, because the slip velocity peaks are different (see Figure 1 and 4). We emphasize the difficulty in using source time functions that are particularly sharp. In fact, even with a spatial discretization of 100 m in the numerical algorithm, the traction evolution inferred by using the time function f_3 of figure 1 shows evidence of numerical dispersion (see the shaded area in figure 4), which is due to a spatial under-sampling of slip velocity.

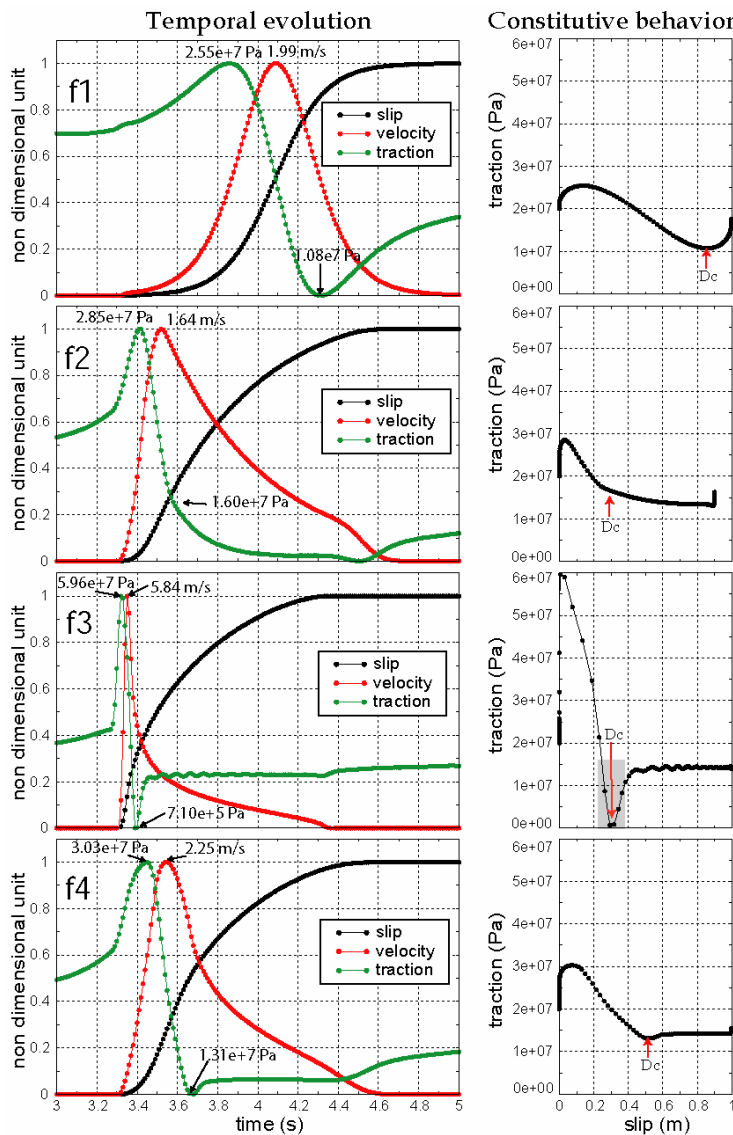


Figure 4: Normalized time histories of slip, slip velocity and total dynamic traction (left panels) calculated with the source time functions defined in equations (5.3a-b-c) for the target point P1 (shown in Figure 1a). Right panels show the resulting slip weakening behaviors in dimensional units. The arrows depict the estimated value of the critical slip weakening distance. Numbers indicate the absolute amplitude values in each panel.

Therefore, the required spatial and temporal resolution of the dynamic model depends on the shape of the selected source time function. It is interesting to note that the traction computed with the function f_4 is in good agreement with the analytical form, well known in the literature (Nielsen and Madariaga, 2003 and references therein). The numerical simulations shown in Figure 4 demonstrate that the inferred values of D_c strongly depend on the assumed source time function: the smoothest function (f_1) gives an estimate of D_c exceeding 80% of total slip, while the sharpest one (f_3) yields D_c of the order of 30% of the final slip. These results are consistent with the conclusions of previous investigations that pointed out the high sensitivity of D_c estimates to fault parameterization (Day et al., 1998; Guatteri and Spudich, 2000).

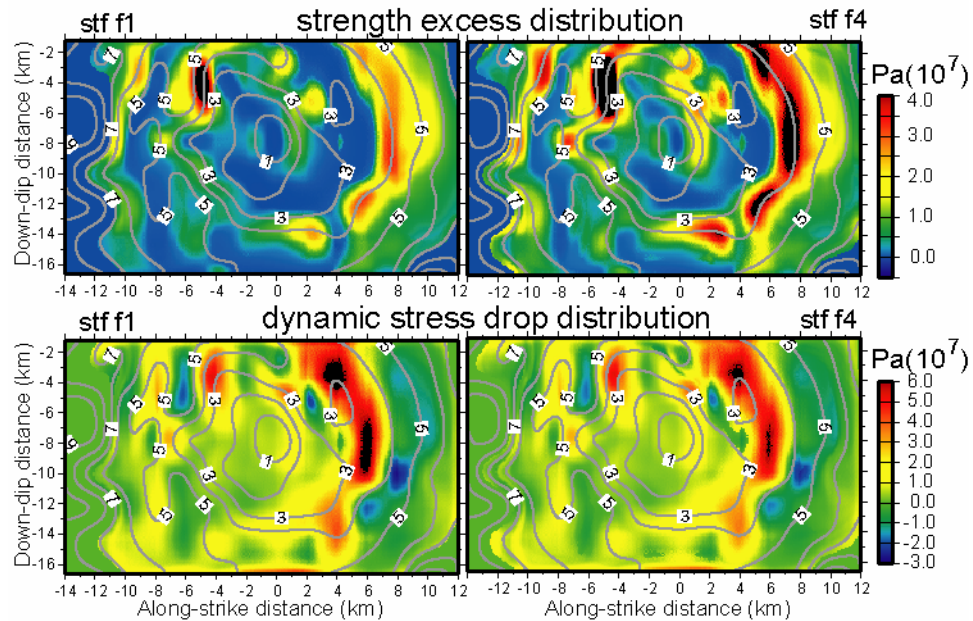


Figure 5: Strength excess and dynamic stress drop distribution calculated on the fault plane, using the source time functions f_1 and f_4 shown in figure 1. The rupture time distribution is superimposed to each panel.

5.3.3 Simulations with a heterogeneous slip model

We now examine the dynamic traction evolution calculated from a heterogeneous kinematic model. We use the slip distribution proposed by Iwata and Sekiguchi (2001) for the 2000 Western Tottori earthquake. For the purpose of our study, we oversimplified this model by retaining only the rupture times and the strike

component of the slip distribution (shown in Figure 2b). We consider two source time functions among those shown in Figure 1, namely f_1 and f_4 , using a constant rise time of 1 s. The resulting two different slip velocity models are used as input for the dynamic code to compute the spatio-temporal evolution of total traction: the inferred spatial distribution of dynamic stress drop and strength excess are shown in Figure 5. This figure shows that high values of strength excess are found in correspondence of zones where the crack tip decelerates. The adopted source time function affects the amplitudes of both strength excess and dynamic stress drop: the source time function f_4 produce larger strength excess amplitudes than those calculated from f_1 , while the contrary happens for the stress drop values. This is due to the fact that f_4 has a steeper initial slope (see Figure 1) and generates larger slip accelerations than f_1 .

We show in Figure 6 the distribution of the breakdown stress drop (defined by Ohnaka and Yamashita, 1989, as the difference between the yield and the frictional stress) and the critical slip weakening distance calculated for f_1 and f_4 . This figure illustrates that the breakdown stress drop is less dependent on the adopted source time function than strength excess or dynamic stress drop. This result suggests that the two source time functions affect the amplitudes of both yield and frictional stresses of nearly the same amount. Moreover, the spatial distribution of D_c inferred for both f_1 and f_4 is correlated with the final slip distribution. This observation is consistent with the dynamic modeling results obtained by Zhang et al. (2003). The ratio between D_c and the final slip strongly depends on the adopted source time functions.

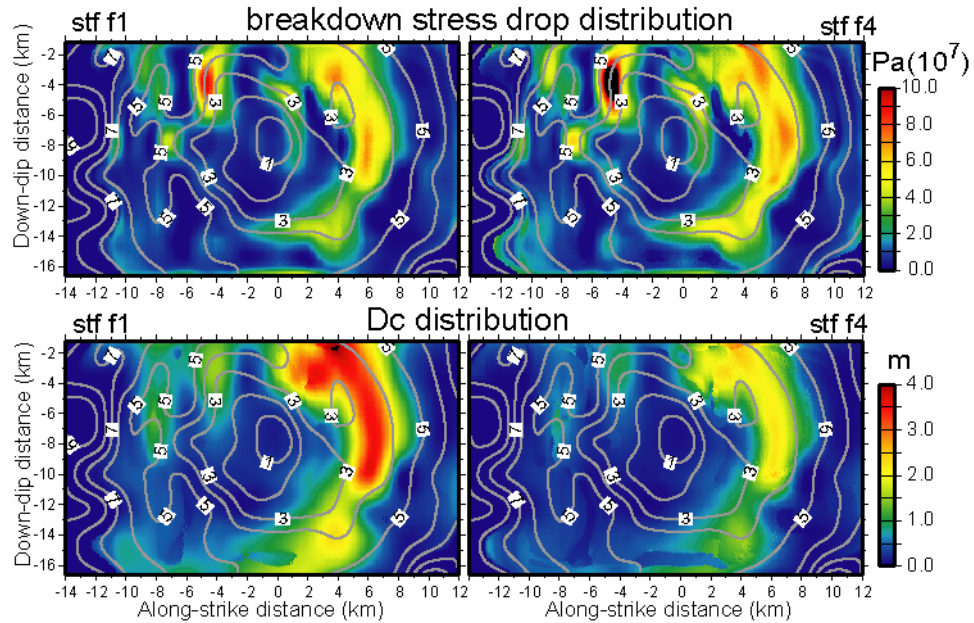


Figure 6: Distribution of breakdown stress drop and critical slip weakening distance on the fault plane retrieved for the two source time functions f1 and f4. The rupture time distribution is superimposed to each panel.

5.3.4 Discussion

We show that the choice of the source time function in kinematic rupture models affects the calculation of dynamic parameters in numerical algorithms which use the slip history as a boundary condition on the fault plane. The most interesting results concern the inferred value and the spatial distribution of the critical slip weakening distance (D_c). We find that different source time functions yield different D_c values ranging between 30% and 80% of the total slip. We also point out that the same source time function, smoothed in different way, yields different D_c values. This occurs because the smoothing operation modifies the initial slope and the associated slip acceleration.

Our simulations point out that different dynamic stress drop patterns can be associated with the same slip distribution. This might represent an important limitation to constrain the slip weakening distance using kinematic models derived from ground motion modeling.

In this synthetic test study, we have chosen a spatio-temporal resolution that is better than that used in kinematic modeling of ground motion waveforms recorded

during real earthquakes. Therefore, the retrieved pattern of strength excess and dynamic stress drop, as well as the critical slip weakening distance, are biased by the limited temporal resolution and the low frequency representation of the adopted source time functions. The methodology used in this study to infer the traction evolution and the slip weakening curves is common to many recent investigations. However, in these numerical approaches the source time function is chosen a priori, and it might not be consistent with the dynamic propagation of an earthquake rupture. We have verified this inadequacy when we have modeled heterogeneous distribution of rupture times. In fact, in those fault portions where the rupture accelerates or decelerates, the peak, the shape and the duration of slip velocity do not change as expected by rupture dynamics, because they are imposed a priori. This condition limits the capability to reconstruct the time history of dynamic traction overall the fault plane. The possibility that kinematic models might not be dynamically consistent should be taken into account to constrain stress or strength during earthquake ruptures.

For this reason, we suggest the use of source time functions which are compatible with earthquake dynamics. On the basis of these findings in the next section we will propose an analytical expression for a new source time function suitable for the dynamic rupture modeling.

5.4 A kinematic source time function compatible with earthquake dynamics

We have underlined that several assumptions are needed to constrain the rupture history of an earthquake and to infer a unique kinematic source model. We do not discuss here the issues related to the discrete representation of the fault as well as to the resolution and the accuracy of the inversion procedure. Instead, we will focus on the adoption of the source time function (STF) that prescribes the slip velocity evolution during the rupture propagation on the assumed fault. This is particularly important for single time-window inversion procedures, in which

the temporal evolution of slip or slip velocity is prescribed by assuming an analytical expression of STF. However, multi-window approaches are often applied to invert ground motion time histories. The STF adopted in multi-window methods are rather crude and the final source time function is given by the superposition of several functions (a triangular function in most of the cases) appropriately shifted in time. Cohee and Beroza (1994) compared these two methods of waveform inversion and found that the single time window technique does a better job in recovering the true seismic moment and the average rupture velocity.

Nakamura and Miyatake (2000) proposed an “ad hoc choice” of the slip velocity function to fit dynamic rupture models. In their time-domain parameterization they introduced a source time function composed by the combination of a quadratic function, a kostrov function and finally a linear function. They were interested in near-field strong ground motion simulations rather than to better constrain the dynamic models. Several others papers (Hisada, 2000; 2001; Guatteri et al., 2003) have pointed out the importance of the STF in kinematic source models for strong ground motion prediction.

Nielsen and Madariaga (2003) theoretically derived a formulation for self-similar and self-healing pulses (functions f_3 and f_4 of previous section), which may represent an alternative to the Kostrov's crack solution (i.e., a square root singularity function; Kostrov, 1964) and is compatible with evidences of pulse-like rupture propagation observed in many investigations (e.g. Heaton, 1990).

This function was originally proposed by Yoffe (1951) for steady state solution in mode I crack and subsequently by Broberg (1978, 1999) and Freund (1979), who extended it to a mode II crack propagation. Hereinafter we refer to this source time function as the *Yoffe* function.

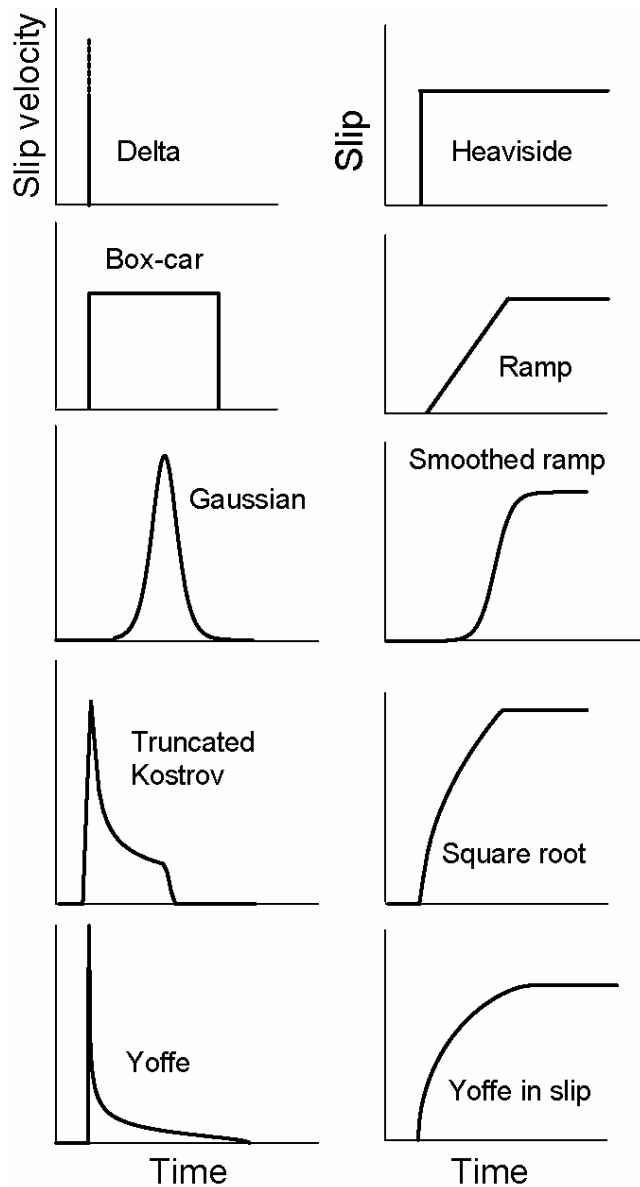


Figure 7: Slip velocity functions of delta, box-car, Gaussian, truncated Kostrov, and Yoffe are shown in left panels. The corresponding slip functions of Heaviside, ramp, smoothed ramp, square root, Yoffe in slip are shown in right panels.

In the previous section we have discussed the effect of different STFs on the estimation of dynamic parameters. In particular, we compared the traction evolutions inferred from several well-known STFs: a smoothed ramp function, an exponential function and a regularized *Yoffe* function (see some examples in Figure 7). We pointed out that the distribution of dynamic parameters strongly depends on the assumed STF and we suggested that the obtained dynamic parameters might be biased especially when using STFs that are not compatible with elastodynamics. In particular, we have shown that the inferred values of the

critical slip weakening distance, stress drop and strength excess as well as their distribution on the fault plane are affected by the adopted source time function.

In this section, we extend this work by introducing a new STF and providing an analytical form which is compatible with elastodynamics. We propose an analytical function which is suitable for the dynamic rupture modeling based on the *Yoffe* function derived by Nielsen and Madariaga (2003). In order to eliminate its singularity, we convolve the original *Yoffe* function with a triangular function and obtain a regularized *Yoffe* function. We promote our solution for several reasons. First, this function is consistent with the self-similar solution of elastodynamic equation and with spontaneous dynamic models governed by slip-weakening (Nielsen and Carlson, 2000; Nielsen and Madariaga, 2003). Second, this function can describe a local healing process with variable rise time consistent with laboratory experiments on fault friction (Ohnaka and Yamashita, 1989). Third, this function is consistent with traction evolution of spontaneous crack models, describing the traction drop near the propagating rupture front within the cohesive zone and providing realistic values of the critical slip weakening distance. Fourth, this function can be easily used in either forward or inverse waveform modeling.

5.4.1 Analytical form of the new kinematic source time function

The most common assumption in kinematic modeling of ground motion time histories is the definition of a finite slip duration during the rupture propagation at variable velocity (e.g. Heaton, 1990). Once the source time function is chosen, its shape is prescribed by the total slip value, the rupture time and the rise time (duration of slip) at each point on the fault. This parameterization is common to both multi-window and single window inversion procedures. However, the former approach allows in principle a more flexible way of modeling slip duration (e.g. Hartzell and Heaton, 1983; Wald and Heaton, 1994; Yagi and Kikuchi, 2000; Sekiguchi and Iwata, 1996; Kaverina et al., 2002). If the temporal resolution would be high (i.e. very short duration of unit source

time functions), the multi-window approach might yield reasonable estimations of total slip duration. Unfortunately, this condition is very rare and for most of the applications the total slip duration at each point on the fault is inferred through a few (less than 6) superimposed simple functions. The single window approach has been used by assuming different functional forms of STF to retrieve the rupture history of large earthquakes (e.g. Fukuyama and Irikura, 1986; Fukuyama and Mikumo, 1993; Cotton and Campillo, 1995). The more unphysical STF is the Heaviside function in slip, corresponding to a delta function in slip velocity. The simplest STF is a ramp in slip of duration τ_R (its corresponding slip velocity is a box-car) and a smoothed ramp function proposed by Bouchon (1997) (its corresponding slip velocity is similar to a Gaussian function). More complicated functions have been proposed: the truncated inverse square root singularity (Beroza and Spudich, 1988), the exponential (Cotton and Campillo, 1995) and the power law (Liu and Archuleta, 2004) functions among many others. In Figure 7 we show examples of these functions. In many of the above studies, the selection of STF was done without careful inspections on the physical consistency nor insights to the consequences for dynamic modeling.

We deal in this section with the problem of kinematic models consistent with earthquake dynamics. To this goal we propose a regularized *Yoffe* function as a candidate of a kinematic source time function. Nielsen and Madariaga (2003) proved that the *Yoffe* function shown in Equation (5.3c) is an alternative of the Kostrov solution (Kostrov, 1964). We rewrite here the equation for completeness:

$$Y(t) = \frac{2}{\pi\tau_R} H(t)H(\tau_R - t) \sqrt{\frac{\tau_R - t}{t}} \quad (5.4)$$

where τ_R is the rise time and $H(t)$ is the Heaviside function. Thus we modified this analytical *Yoffe* function as described in Equation (5.4) in order to remove the singularity at the rupture front. We have showed that if the *Yoffe* function is convolved with a triangular time function, the source time function can be used as a boundary condition in a 3D dynamic rupture computation to compute the traction evolution. The constitutive relation inferred from both assumed slip function and corresponding traction evolution still preserves a slip-weakening behavior as the original *Yoffe* function. Here we derive an explicit form of this

function by analytical computation. The triangular function can be expressed as follows:

$$W(t) = \frac{1}{\tau_s} [tH(t)H(\tau_s - t) + (2\tau_s - t)H(t - \tau_s)H(2\tau_s - t)] \quad (5.5)$$

where τ_s is the half duration of the triangular function. Therefore, the regularized *Yoffe* function can be obtained by convolving Equation (5.4) with Equation (5.5) as follows:

$$S(t) = D_{\max} \int_{-\infty}^{+\infty} W(t - T)Y(T)dT \quad (5.6)$$

where D_{\max} stands for final slip. The explicit analytical formulation of this function is presented in the Appendix. In the following of this study we refer to $S(t)$ as a slip velocity time function. It should be noted that the regularized *Yoffe* function can now be fully described through three parameters: τ_R , τ_s , and D_{\max} . In Figure 8 we show a comparison between the original *Yoffe* function and the regularized *Yoffe* proposed in this section.

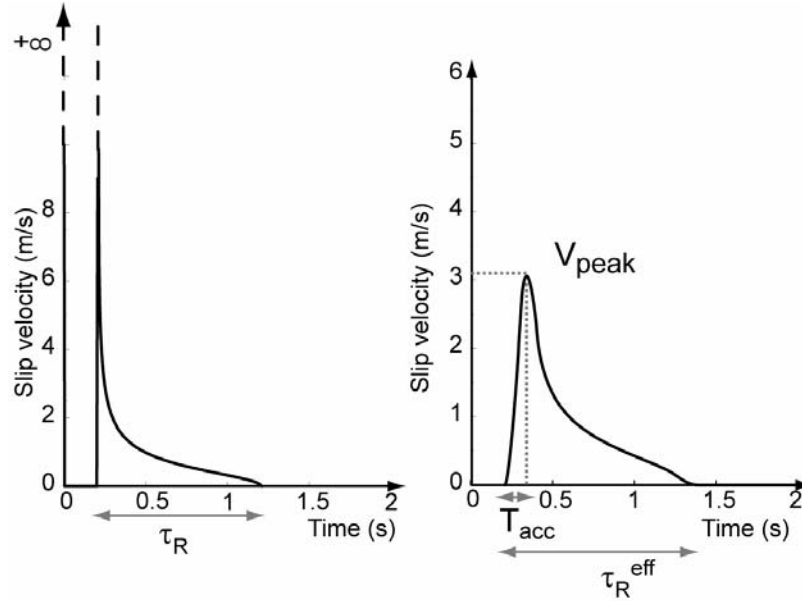


Figure 8: Comparison between the original *Yoffe* function (left) and the regularized *Yoffe* function (right) calculated for $\tau_s = 0.15s$. The peak velocity (V_{peak}) becomes finite in the smoothed case although it is infinite in the original definition.

In the following sections we investigate the relations between these three parameters and those obtained by dynamic rupture computations. This allows us to investigate the fundamental features of the key kinematic parameters useful to

describe the source process. It should also be noted that this function is similar to that inferred by Ohnaka and Yamashita (1989) from laboratory experiments (see Panel C in Figure 6 of Ohnaka and Yamashita, 1989).

5.4.2 Parameterization of source time function

Numerical simulations of spontaneous dynamic rupture of earthquakes clearly show that the traction evolution within the cohesive zone controls the slip acceleration and the slip velocity time history (Chapter 2). Recent investigations have pointed out that the shape, peak value and time of peak slip velocity vary during the dynamic propagation. These parameters are controlled by the initial stress, frictional parameters and constitutive relations on the fault.

It seems convenient to introduce a new parameter T_{acc} , which is defined as the time to peak slip velocity (i.e. the duration of positive slip acceleration) as illustrated in Figure 8.

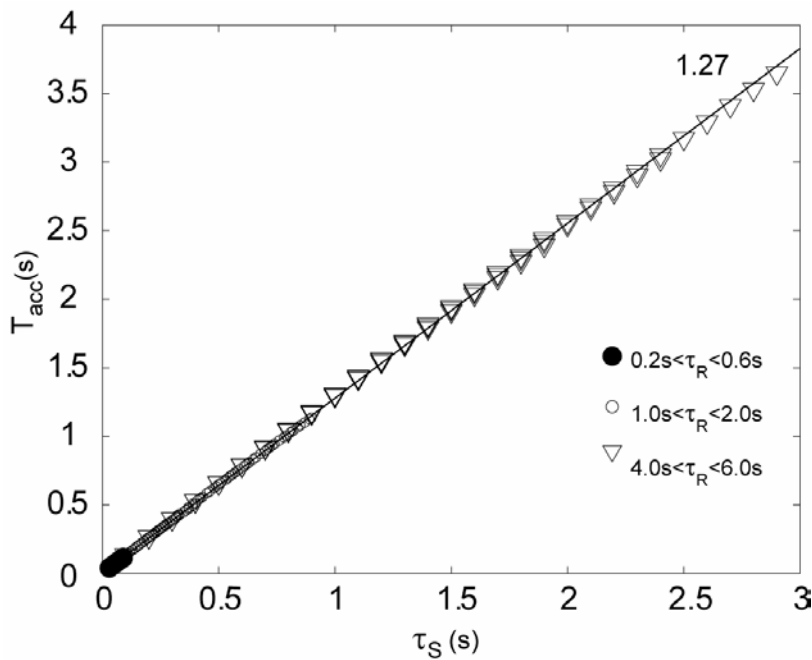


Figure 9: Correlation plot between smoothing time window (τ_s) and time to peak slip velocity (T_{acc}) for various rise time values τ_R comprised between 0.2s and 6.s. The straight line represents the linear regression.

In the original *Yoffe* function, T_{acc} is zero because of the singularity. On the contrary, in the regularized *Yoffe* function, T_{acc} is controlled by the duration of the

triangular function used as a smoothing operator τ_S , which is not a physical parameter. The temporal smoothing of original Yoffe function yields finite peak slip velocity values. Because τ_S appears only in the regularized *Yoffe* function, we numerically investigated the relation between T_{acc} and τ_S for different τ_R . As shown in Figure 9, T_{acc} is linearly related to τ_S , confirming that τ_S directly controls the duration of the positive slip acceleration (T_{acc}). In particular, the ratio T_{acc}/τ_S does not depend on other parameters and is equal to 1.27 ± 0.01 . The linear relation has been inferred by varying the rise time between 0.2s and 6.0s: Figure 9 clearly shows that τ_S does not affect T_{acc} .

However it should be noted that, after temporal convolution, the effective final duration of the STF (τ_R^{eff}) is slightly larger than τ_R :

$$\tau_R^{eff} = \tau_R + 2\tau_S \quad (5.7)$$

Therefore, our proposed source time function is parameterized by the three parameters having a clear physical meaning: the total slip D_{max} , the slip duration (rise time) τ_R and the duration of the positive slip acceleration T_{acc} . We will discuss later the relation between these parameters and the dynamic ones which govern the dynamic process of earthquake rupture.

5.4.3 Kinematic relations

In this section we discuss the relations between the kinematic source parameters: τ_R , D_{max} , T_{acc} , τ_S , and V_{peak} . We start pointing out that only few parameters are usually retrieved through kinematic analyses of forward or inverse modeling of seismic waves (see Beresnev, 2003). The rupture time, final slip and, sometimes, the slip duration are commonly estimated but slip velocity function and inferred peak slip velocity are rarely estimated. We emphasize however that the relation between total slip and V_{peak} depends on the adopted source time function. Moreover, peak slip velocity can change dramatically during the dynamic rupture process.

We plot in Figure 10 a set of our new STF obtained by changing only the τ_R values (upper panel) or the τ_S values (bottom panel). From Figure 10 we observe that T_{acc} does not depend on the rise time τ_R but is related to τ_S as

described above. This is physically reasonable because it is widely believed that different mechanisms control slip acceleration and the healing of slip (see Chapter 1).

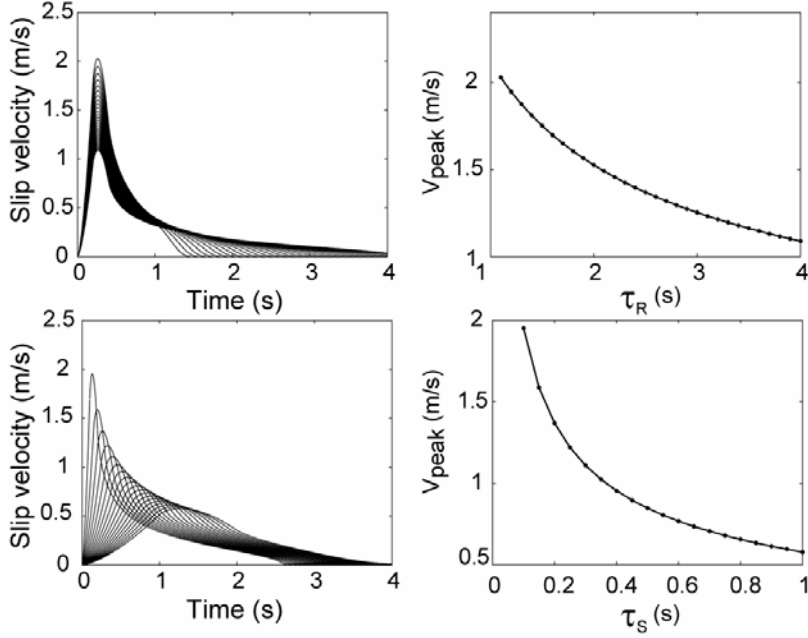


Figure 10: Upper left panel shows slip velocity functions using $\tau_S = 0.2s$ with variable τ_R in a range between $1s$ and $4s$. Lower left panel is slip velocity functions using $\tau_R = 2.5s$ with variable τ_S in a range between $0.1s$ and $1s$. In the right panels, the corresponding V_{peak} distributions as a function of τ_R or τ_S are shown.

To investigate analytically the relation between T_{acc} and the corresponding V_{peak} , we need to compute the derivative of STF (i.e. slip acceleration function). Since T_{acc} is always in the range between τ_S and $2\tau_S$ as illustrated in Figure 9, the derivative in this range becomes

$$\dot{S}(t) = -2\sqrt{(t-\tau_S)(\tau_S+\tau_R-t)} - 2\tau_R \arcsin\sqrt{\frac{(t-\tau_S)}{\tau_R}} + \sqrt{t(\tau_R-t)} + \tau_R \arcsin\sqrt{\frac{t}{\tau_R}} \quad (5.8)$$

Unfortunately it was quite difficult to find an explicit analytical formulation of T_{acc} , which is the solution of $\dot{S}(t)=0$. We are therefore confined to solve this equation numerically. We compute the Taylor series expansion of Equation (5.8) to obtain the expression of T_{acc} as a function of other parameters. The obtained relation is

$$T_{acc} = 1.3 \tau_S + O(f \tau_R, \tau_S) \quad (5.9)$$

which is consistent with the numerical results shown in Figure 3. This relation allows us to express V_{peak} as a function of T_{acc} , τ_R , and D_{max} .

We then insert Equation (5.9) into the solution of Equation (5.6) presented in the Appendix (Eqs. A13 and A14) for the range $\tau_S < t < 2 \tau_S$. V_{peak} might be obtained from this relation for $t = T_{\text{acc}}$. Unfortunately, the resulting relation was again complicated and it seems difficult to obtain the explicit formulation of V_{peak} as a function of other kinematic parameters such as T_{acc} , τ_R , and D_{max} . For this reason, we are forced to search the simplest relation numerically, by computing many regularized *Yoffe* functions varying the relevant parameters, as shown in Figure 10. The right panels of Figure 10 display the inverse dependence of V_{peak} on τ_S and τ_R . We then found the following asymptotic relation by trial and error:

$$V_{\text{peak}} = 1.04 \frac{D_{\text{max}}}{T_{\text{acc}}^{0.54} \tau_R^{0.47}} \approx C \frac{D_{\text{max}}}{\sqrt{T_{\text{acc}} \tau_R}} \quad (5.10)$$

Figure 4 shows that, the regularized *Yoffe* functions obtained by fixing the slip duration ($\tau_R = 2.5$ s, bottom panels), display different effective durations (τ_R^{eff}) ranging within the interval predicted by Equation (5.7). Thus, since τ_R is fixed, τ_R^{eff} varies because τ_S is changing. Equation (5.10) allows the association between final slip and peak slip velocity for a given regularized *Yoffe* function.

It should be noted that T_{acc} is different from T_w proposed by Ohnaka and Yamashita (1989). They introduced T_w as the half width of total slip acceleration (that means half rise time) to connect this kinematic parameter with the dynamic breakdown time (T_c). T_c is defined as the time required for the shear stress to decrease from its peak value to a kinetic frictional stress level. In the dynamic spontaneous rupture models T_c is usually non-uniform on the fault. This parameter defines the duration of breakdown process within the cohesive zone. Ohnaka and Yamashita (1989) related T_c with the cutoff frequency (f_{max}^{δ}) of the power spectral density of slip acceleration of the same point on the fault as $f_{\text{max}}^{\delta} = 1/T_c$.

We will do something similar with T_{acc} and T_c in the following section. This new *Yoffe* function allows the slip acceleration to be bounded at and near the propagating crack tip (see panel B in Figure 11). This feature is very important and it is not ensured in dynamic modeling simply introducing a cohesive zone with a constitutive law. The peak slip acceleration is one of the key parameters characterizing earthquake source which is important for strong ground motion prediction.

5.4.4 Deriving dynamic rupture parameters from kinematic models

In this work we use the new regularized STF obtained in the previous section. We assume a homogeneous half-space discretized with grid size $\Delta x = \Delta y = \Delta z = 50$ m, time step $t = 0.005$ s, density $\rho = 2700$ kg/m³ and P- and S- wave velocities are $V_p = 5.2$ km/s and $V_s = 3.0$ km/s, respectively. A planar vertical fault is assumed whose dimensions are 12.8km along strike and 6.4km along dip. The hypocenter is located at 6.4km along strike and 3.2 km along dip, which is the same for all models. Upper margin of the fault is at the free surface.

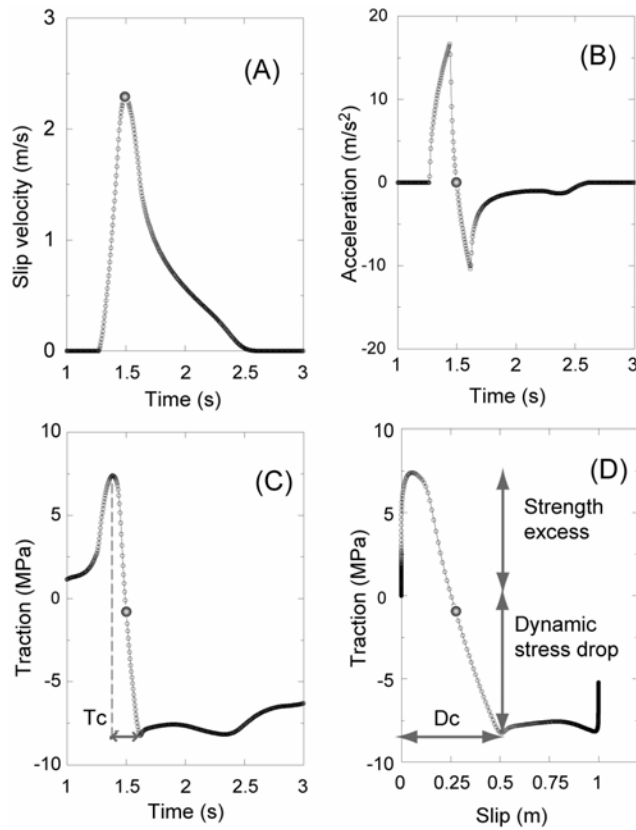


Figure 11: A typical example of (A) slip velocity, (B) slip acceleration, and (C) stress evolution as a function of time during the rupture. (D) stress evolution as a function of slip is also shown. The big open circle indicates the time of peak slip velocity ($t = T_{acc}$). [model #5 in Table 1]

Inferred dynamic parameters

We have computed a number of models to examine the relations between kinematic and dynamic parameters as listed in Table 1. All models have a strike

slip faulting with a uniform distribution of rupture velocity (v_r), τ_R , T_{acc} , D_{max} and initial stress on the fault plane. This means that at each point on the fault the slip velocity function is the same but shifted along time. On the contrary the traction evolution depends on the position on the fault because of the different contribution of the dynamic load (second term in Equation (5.1)). In this computation, we did not use the points close to the fault edge to avoid the artificial reflections due the lack of absorbing boundary condition. In Figure 11 we show an example of the inferred traction evolution at an interior point on the fault plane using the proposed new STF and the kinematic parameters of model #5 in Table 1: panel A displays the adopted STF, panel B the resulting slip acceleration, panel C the calculated temporal evolution of dynamic traction and panel D illustrates the traction evolution as a function of slip. Since seismic waves are only sensitive to the stress change, we can only discuss the relative values of stress. We treat the following values as relative ones: strength excess (difference between yield stress and initial stress), dynamic stress drop (difference between initial stress and minimum stress during slipping), breakdown stress drop (difference between yield stress and minimum stress, $\Delta\sigma_b$). Therefore, we need to assume an initial stress (σ^0) distribution to interpret the slip-weakening curves and the distribution of dynamic parameters on the faults (Tinti et al. 2004b). In this paper we assume a uniform initial stress distribution to examine more easily the dependence of dynamic and kinematic parameters. Hereafter, we show the stress change evolution relative to the uniform initial stress, i.e. $\sigma(t)-\sigma^0$.

We illustrate in Figure 11(D) the strength excess and the dynamic stress drop at this selected point on the fault. We observe a clear restrengthening of stress associated to the healing of slip in Figure 11 (C) and (D). This behavior is called 'undershoot'. We have to note, however, that such a behavior might depend on the position on the fault. In Figure 11 (D), the slip weakening behavior is observed with a critical slip weakening distance D_c . Tinti et al. (2004b) have shown that the spatial distributions on the fault plane of strength excess and dynamic stress drop are strongly controlled by the adopted kinematic parameters. In particular, the strength excess is affected by rupture time distribution as well as

by the peak slip velocity distribution as we will show in the next section, while the dynamic stress drop is controlled mainly by the slip distribution.

#	τ_S (s)	T_{acc} (s)	D_{max} (m)	v_r (km/s)	τ_R (s)	τ_R^{eff} (s)	V_{peak} (m/s)	D_c (m)	$\Delta\tau_b$ (MPa)	T_c (s)
1	0.090	0.115	1.0	2.0	1.0	1.18	3.21	0.376	21.56	0.115
2	0.125	0.160	1.0	2.0	1.0	1.25	2.71	0.437	17.58	0.170
3	0.125	0.160	1.0	2.0	2.0	1.25	1.94	0.313	12.43	0.165
4	0.150	0.195	1.0	2.0	1.0	1.30	2.47	0.475	15.96	0.205
5	0.175	0.225	1.0	2.0	1.0	1.35	2.27	0.509	14.80	0.250
6	0.175	0.225	1.0	2.0	1.5	1.85	1.87	0.421	12.10	0.245
7	0.175	0.225	1.0	2.0	2.0	2.35	1.63	0.366	10.48	0.245
8	0.175	0.225	1.0	2.0	2.5	1.85	1.46	0.330	9.38	0.245
9	0.175	0.225	1.0	2.0	3.0	3.35	1.34	0.301	8.56	0.245
10	0.175	0.225	1.0	1.5	1.0	1.35	2.27	0.501	23.56	0.240
11	0.175	0.225	1.0	1.8	1.0	1.35	2.28	0.506	18.22	0.238
12	0.175	0.225	1.0	1.9	1.0	1.35	2.27	0.508	16.10	0.240
13	0.175	0.225	1.0	2.2	1.0	1.35	2.27	0.505	14.31	0.280
14	0.175	0.225	1.0	2.3	1.0	1.35	2.27	0.512	12.36	0.275
15	0.175	0.225	1.0	2.5	1.0	1.35	2.27	0.505	12.07	0.285
16	0.175	0.225	1.0	2.7	1.0	1.35	2.27	0.498	10.84	0.270
17	0.175	0.225	1.0	3.0	1.0	1.35	2.27	0.470	10.44	0.290
18	0.250	0.320	1.0	2.0	1.0	1.50	1.88	0.597	12.77	0.375
19	0.250	0.320	2.0	2.0	1.0	1.50	3.75	1.193	25.53	0.375
20	0.250	0.320	3.0	2.0	1.0	1.50	5.63	1.790	38.30	0.375
21	0.250	0.320	1.0	2.5	1.0	1.50	1.88	0.587	10.61	0.400
22	0.300	0.385	1.0	2.0	1.0	1.60	1.70	0.640	11.91	0.455
23	0.350	0.445	1.0	2.0	1.0	1.70	1.56	0.684	11.25	0.545

Table 1: List of dynamic rupture computation models

5.4.5 Relation between kinematic and dynamic source parameters

A common feature of dynamic models is the traction evolution within the cohesive zone showing a slip weakening behavior, which in general may have variable weakening rate (i.e., not linear). This has been observed in dynamic simulations performed with different constitutive laws, including time weakening or rate and state dependent friction laws (see Bizzarri and Cocco, 2003 and references therein). The modeling results shown in Figure 11(D) indicate that the peak stress is attained at nonzero slip and that a slip-hardening phase precedes the slip-weakening phase. In our simulations this behavior is a consequence of imposing a bounded slip acceleration. We discuss here that the dynamic traction growth to the upper yield stress value is associated to the slip acceleration phase; in our calculations, the value of T_{acc} controls the traction evolution and the dynamic weakening rate (as seen both by traction versus time and versus slip). In this section we aim to propose useful relations between kinematic and dynamic parameters. We will compare in the following our scaling relations with those proposed by Ohnaka and Yamashita (1989).

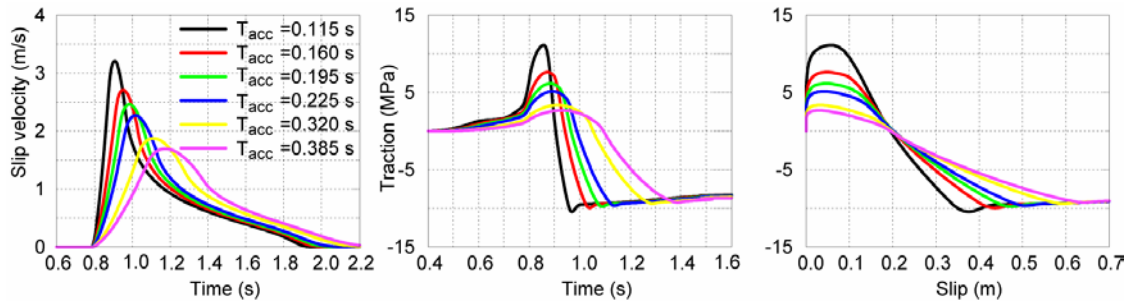


Figure 12: (left) Slip velocity evolutions, (middle) traction evolutions, and (right) constitutive behaviors for various T_{acc} . [models #1; #2; #4; #5; #21 and #22 in Table 1]

We have performed a series of simulations with the parameters listed in Table 1. Each model has a constant rupture velocity and a uniform distribution of kinematic parameters on the fault plane. Figure 12 shows the dynamic traction evolutions and the constitutive behaviors calculated using different slip velocity

functions, each of which is obtained by different smoothing factor τ_S ; consequently different T_{acc} .

According to Equation (5.10) we expect the variation of V_{peak} as a function of T_{acc} , which can be seen in the left panel of Figure 12. Looking at the traction time histories and at the constitutive behaviors in Figure 12, we observe that strength excess, $\Delta\sigma_b$, T_c and D_c depend on T_{acc} . In particular, we point out that the weakening rate ($\Delta\sigma_b / D_c$) is associated to T_{acc} , characterizing the adopted source time function.

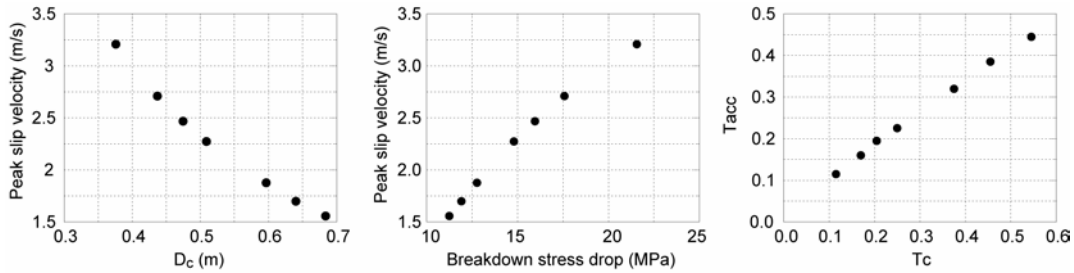


Figure 13: Relations between V_{peak} and D_c (left) or $\Delta\sigma_b$ (center) with different T_{acc} are shown. Relation between T_{acc} and T_c is also shown in right panel. [models #1; #2; #4; #5; #21; #22; #23 in Table1]

To examine the relations between kinematic and dynamic parameters we plot the relations of V_{peak} versus D_c and $\Delta\sigma_b$ and T_{acc} versus T_c in Figure 13. We found a negative correlation between V_{peak} and D_c . On the contrary, a positive correlation between V_{peak} and $\Delta\sigma_b$ is inferred. Besides, the central panel of Figure 12 and the right panel of Figure 13 show a positive correlation between T_{acc} and T_c , i.e. $T_{acc} = KT_c$, where K is a positive constant equal to ~ 0.75 for all models computed in Table 1.

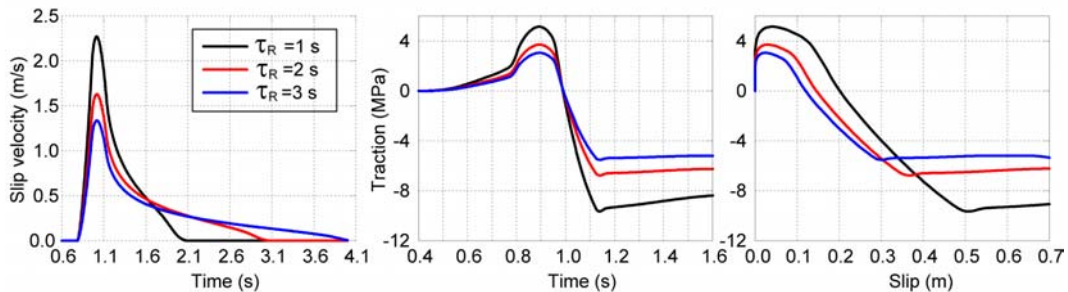


Figure 14: (left) Slip velocity evolutions, (center) traction evolution, (right) constitutive behaviors for various τ_R , using $T_{acc} = 0.225s$. [models #5; #7 and #9 in Table 1]

We show in Figure 14 the traction evolutions and constitutive behaviors corresponding to several slip velocity functions with different τ_R (and constant T_{acc}). The left panel of this figure indicates that decrease of τ_R reduces the frictional stress level and increases D_c . In particular, looking at the central panel of Figure 14, we observe that the minimum traction is achieved at the same time, which means that T_c is constant. The comparison between the slip-weakening curves (stress versus slip plots) in Figure 12 and Figure 14 confirms that T_{acc} controls the weakening rate ($\Delta\sigma_b/D_c$). The inverse relation between τ_R and D_c in Figure 14 may look somehow strange, but since all the kinematic parameters other than τ_R are kept constant and the inferred T_c is then constant, the shorter τ_R results in the larger D_c . In Figure 15 we plot the V_{peak} versus D_c for four simulations with different uniform rise times (varying from 1.0s to 3.0s) and for a simulation having variable rise time on the fault ranging from 0.6s to 3.5s. In this case, we observe a positive correlation between these two parameters. This is because D_{max} is kept constant and then shorter τ_R produces larger V_{peak} .

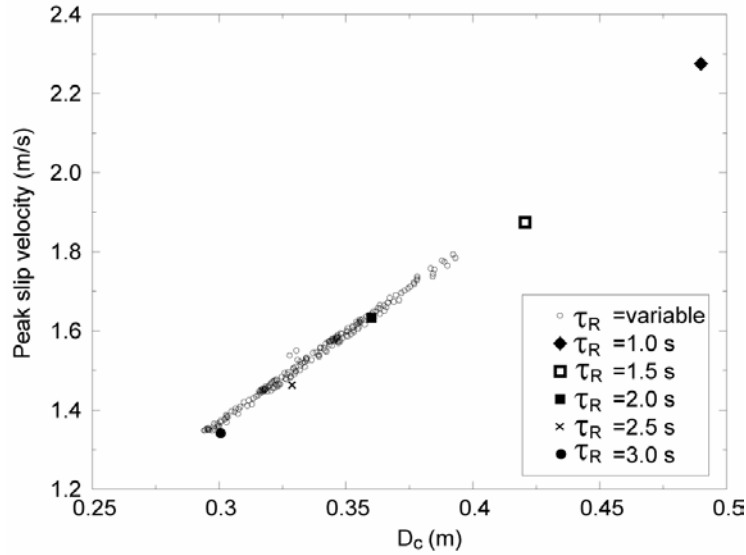


Figure 15: Relation between V_{peak} and D_c for different τ_R , assuming $T_{acc}=0.225s$. Each black dot corresponds to different point on the fault for variable τ_R . [models #5; #6; #7; #8 and #9 in Table1]

By compiling all these simulations we have verified that V_{peak} is related to D_{max} and D_c by an expression depending on both τ_R and T_{acc} . Here we propose the following scaling relations derived for uniform τ_R and T_{acc} , respectively:

$$V_{peak} \propto \frac{D_{max}^2}{D_c \tau_R} \quad (5.11)$$

$$V_{peak} \propto \frac{D_c}{T_{acc}} \quad (5.12)$$

From these equations we obtain:

$$D_c \propto \sqrt{\frac{T_{acc}}{\tau_R}} D_{max} \quad (5.13)$$

Equation (5.12) is the same as Equation (44) in Ohnaka and Yamashita (1989): $\dot{D}_{max} = (0.56 \div 0.91) D_c f_{max}^s$, where \dot{D}_{max} is peak slip velocity and f_{max}^s is the inverse of T_c . From this equation, it emerges that the ratio D_c/D_{max} depends on the ratio T_{acc}/τ_R and therefore it can be variable on the fault plane.

We obtain the relation between V_{peak} and breakdown stress drop:

$$V_{peak} \propto \Delta\sigma_b \quad (5.14)$$

This equation corresponds to the Equation (47) of Ohnaka and Yamashita (1989) ($\dot{D}_{max} = v\sigma_p / C(v)\mu$, where σ_p is $\Delta\sigma_b$ in our notation and μ is the rigidity).

Finally, from Equations (5.12) and (5.14) as well as the relation $T_{acc} \propto T_c$, we obtained $T_c \propto D_c / \Delta\sigma_b$, that is the same as Equation (50) of Ohnaka and Yamashita (1989).

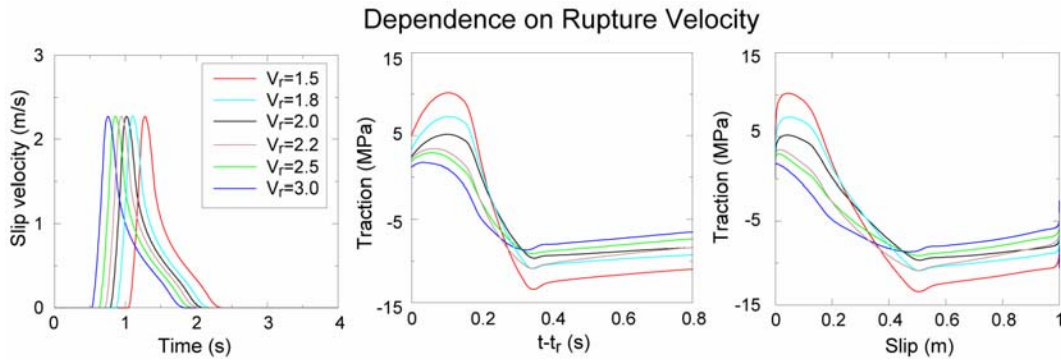


Figure 16: (left) slip velocity evolutions, (center) traction evolutions, and (right) constitutive behaviors are shown with different rupture velocities. [models #5; #10; #11; #13; #15 and #17 in Table 1]

In all the above proposed scaling relations we can consider the dependence of rupture velocity. We examined the effect of variable rupture velocity (different

uniform rupture time distribution). By fixing D_{\max} , T_{acc} and τ_R (then V_{peak} becomes fixed), we simulated rupture processes changing only the rupture time distribution. The range of rupture velocity (v_r) is set from 1.5 km/s to 3 km/s. We plot the corresponding traction evolutions and the inferred constitutive behaviors for the same point on the fault in Figure 16. Because in our simulations the rupture onset (i.e. the rupture times, t_r) are different, in central panel we plot $\Delta\sigma_b$ as a function of relative time ($t-t_r$). D_c and T_c are approximatively constant and the variation between the traction evolutions depends only on $\Delta\sigma_b$. From Figure 17, we found an inverse correlation between $\Delta\sigma_b$ and v_r . In these simulations V_{peak} is set constant. We confirmed that Eq. (5.14) becomes

$$V_{\text{peak}} \propto C(v_r)\Delta\sigma_b \quad (5.15)$$

where $C(v_r)$ is a constant depending on the rupture velocity, as stated in the Ohnaka and Yamashita (1989) equations.

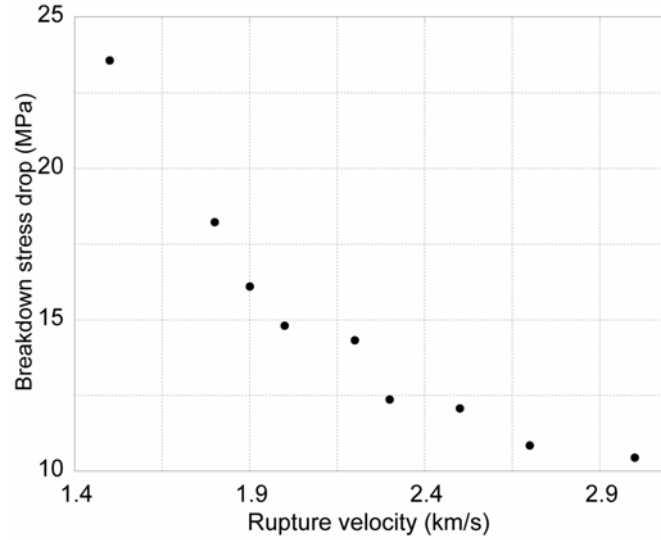


Figure 17: Traction (MPa) Relation between $\Delta\sigma_b$ and v_r , assuming $T_{\text{acc}} = 0.225s$ and $\tau_R = 1s$. [models #5; #10-17 in Table 1]

5.4.6 Discussions

We propose an innovative and original parameterization of the source time function to be used in kinematic modeling of ground motion time histories. We suggest that a kinematic model can be adequately described by the total slip

(D_{\max}) and the rupture time distributions on the fault plane as well as by the source time function defined by the slip duration (τ_R) and the duration of the positive acceleration (T_{acc}). We propose several scaling relations between kinematic and dynamic parameters. It is important to emphasize that our proposed scaling relations agree with those obtained by Ohnaka and Yamashita (1989). Their work is based on a comparison between laboratory experiments, theoretical considerations and numerical simulations of spontaneous dynamic crack propagation in 2-D. They assumed a slip-dependent constitutive law (exponential law) and inferred some relations between kinematic and dynamic parameters. Moreover, their theoretical and numerical results start from the crack model assumption, not including the local healing of slip. Our assumptions are completely different but the inferred relations are consistent. Because our slip velocity functions have a finite duration, the inferred traction evolution shows restrengthening and healing of slip. The agreement between our scaling relations and those proposed by Ohnaka and Yamashita (1989) further corroborates the validity of our numerical analyses.

The parameter T_{acc} , used to define the regularized *Yoffe* function, is linearly related to the duration of the breakdown process T_c (see Figures 11 and 12) and the proportionality factor between these two parameters depends on the assumed rupture velocity. This is evident looking at the results of our simulations listed in Table 1.

Mikumo et al. (2003) proposed that the critical slip weakening distance can be measured as the slip at the time of peak slip velocity. As discussed on chapter 4 this implies that the duration of the positive slip acceleration T_{acc} has to be close to the duration of the breakdown process, and thus their ratio should be close to unity. Our modeling results suggest that this is true only for constant (or weakly variable) rupture velocity models. In chapter 4 have shown that T_{acc} and T_c depend on the adopted constitutive law and on the constitutive parameters as well as the friction behavior at high slip rates. Therefore, we emphasize that T_{acc} is a source parameter with a clear physical meaning and it is directly controlled by fault constitutive properties. Simulations with spontaneous dynamic rupture models suggest that in general T_{acc} can change on the fault plane.

Another interesting result is the linear relation between peak slip velocity and breakdown stress drop, in agreement with Ohnaka and Yamashita (1989). This scaling relation points out that peak slip velocity is related to the mechanisms controlling the breakdown process and to the earthquake stress drop. The proportionality factor between these two parameters depends on rupture velocity, as previously suggested by Ohnaka and Yamashita (1989). We have also shown that the final slip (D_{\max}) and the critical slip weakening distance D_c are related and that their ratio depends on both slip duration and T_{acc} . This scaling relation (see Equation 5.13) does not imply that the ratio between these two parameters is constant on the fault plane, because both T_{acc} and τ_R can vary as a function of positions on the fault plane.

The scaling relations proposed in this study can be very useful to constrain the values and to potentially reduce the number of independent parameters in the kinematic inversion of seismograms. For example, once we construct a model with a given distribution of D_{\max} and D_c , we can examine the different combinations of other parameters such as τ_R and V_{peak} . It should be emphasized that in many kinematic models τ_R is not well constrained and T_{acc} is not investigated and imposed along with the assumed source time function. Although we believe that the estimation of T_{acc} through the modeling of radiated waveforms is extremely delicate, we underline that the proposed parameterization of the STF is suitable to associate kinematic and dynamic parameters. This is very important for the dynamic interpretation of kinematic slip models.

Chapter 6

Earthquake fracture energy inferred from kinematic rupture models on extended faults

6.1 Introduction

The elastic strain energy released during an earthquake is partitioned into radiated energy, heat and the fracture energy consumed as the rupture area expands. The quantification of these global quantities [i.e., for the whole rupture area] allows the definition of the earthquake energy balance, which is an important issue in earthquake mechanics. However, the evaluation of the fracture energy at a specific point on the fault plane is not a common procedure and relies on knowledge of the dynamic traction evolution with coseismic slip. Different constitutive behaviors have been proposed to describe dynamic stress breakdown processes during earthquake ruptures and the physical mechanisms controlling the dynamic traction evolution are still a matter of debate. Here we focus on the seismic inferences of fracture energy to constrain the way fault strength degrades during slip and to test whether fracture energy is stably inferred (Grueteri and Spudich, 2000; Grueteri et al., 2001).

High-quality strong motion and teleseismic waveforms are nowadays available immediately after a moderate-to-large earthquake and numerous kinematic slip models on extended faults are routinely computed. Therefore, many investigators have attempted to infer dynamic parameters from these kinematic models to reveal elements of physical processes operating on faults during earthquakes [e.g. to discriminate crack model from healing pulse model and to deduce the dynamic traction evolution and the weakening processes]. For example, we mention Quin [1990] (1979 Imperial Valley), Mikumo and Miyatake

[1995] (1984 Morgan Hill), Ide and Takeo [1997] (1995 Kobe), Bouchon [1997] (1979 Imperial Valley, 1984 Morgan Hill, 1989 Loma Prieta, 1994 Northridge), Day et al. [1998] (1992 Landers; 1994 Northridge; 1995 Kobe), Pulido and Irikura [2000] (1992 Landers), Guatteri et al. [2001] (1995 Kobe), Dalguer et al. [2002] (2000 Tottori), Zhang et al. [2003] (1999 Chi Chi), Mikumo et al. [2003] (2000 Tottori), among many others. Using the information given by the kinematic slip model, they computed the spatial distribution on the fault of dynamic parameters such as strength excess, dynamic stress drop, and critical slip weakening distance D_c . Many of these studies obtained a large value of D_c and a strong correlation of this parameter with total slip.

Guatteri and Spudich [2000], through a dynamic inversion method, found two dynamic models having very similar ground motions, rupture times, slip distribution and fracture energy but different traction evolutions. They showed the trade-off between D_c and strength excess parameters. The important part of their work was that both models had the same fracture energy, which implies that the fracture energy can be stably estimated over at least a limited range of slip weakening distances, despite the nonuniqueness of the other dynamic parameters.

In chapter 5 we studied the dynamic consequences of the slip velocity function (SVF) adopted *a priori* in kinematic inversions. Using kinematic models as input, we observed the dependence of traction evolution and dynamic parameters (strength excess, dynamic stress drop, and critical slip weakening distance) on the shape of the SVF and on its parameters such as peak value, rise time and duration of positive acceleration. Spudich and Guatteri [2004] showed that low-pass filtering of kinematic slip models can bias inferences of D_c and D_c' (defined in Mikumo et al. [2003]) to large values and possibly bias fracture energy upward and radiated energy downward.

In this last chapter we estimate fracture energy on extended faults for moderate to large earthquakes (Landers 1992, Northridge 1994, Tottori 2000, Imperial Valley 1979, Morgan Hill 1984, Colfiorito 1997, Kobe 1995) and we compare the results with the previous studies. Following the pioneering work of Husseini et al. [1975],

many authors have estimated fracture energy for earthquakes using different procedures [Beroza and Spudich, 1988; Guatteri et al., 2001; Favreau and Archuleta, 2003, Ide, 2003; Rice et al., 2004]. Almost all these cited authors give estimates of average fracture energy (G) for the whole rupture and potential scaling relations between G and other average kinematic and dynamic parameters. We will discuss the still large uncertainties about the different mechanisms that contribute to the partitioning of earthquake energy. We will interpret the inferred dynamic traction evolutions and we will examine the factors that determine the compatibility between kinematic images and dynamic models. Despite the nonuniqueness of kinematic models and the assumptions needed to compute dynamic models, fracture energy may be a less nonunique observational parameter to characterize the dynamic rupture [Guatteri and Spudich, 2000]. Finally, using our large set of real earthquakes (13 kinematic models), we provide scaling relations between average fracture energy density and several kinematic factors.

6.2 Methodology

6.2.1 Computation method

Here we only summarize the methodology explained in Chapter 5. We use a 3-D finite difference code based on the Traction-at-Split nodes method to calculate the stress time series on the earthquake fault plane [Andrews, 1999]. The fault is represented by a surface containing double nodes and the stress is computed through the fundamental elastodynamic equation [Ide and Takeo, 1997]. Assuming that linear elastodynamics governs the disturbance off the fault plane itself, each node belonging to the fault plane is forced to move with a prescribed slip velocity time series. In other words, we impose the slip velocity as a boundary condition on the fault, determining the stress-change time series everywhere on the fault. In this way we do not need to specify any constitutive relation and the dynamic traction evolution is a result of the calculations. The space and time

distribution of slip velocity are obtained from the kinematic rupture models. We cannot use exactly the original kinematic images because the dynamic computations require spatio-temporal interpolations and smoothing operations to convert the slip model to a continuously differentiable slip-rate function. Before computing the traction evolutions we look at the resolution analysis and the smoothing operation. The free surface is included and the Earth models are simplified assuming homogeneous half-spaces.

6.2.2 Interpolation and Smoothing

The finite difference computation of stress requires interpolation to a finer grid than that found in the kinematic models because of the stability and convergence conditions that the finite difference code has to satisfy [Bizzarri and Cocco, 2003]. In addition, temporal and spatial smoothing are required to avoid the artificial stress singularities that would exist at the edges of blocky subfaults in the kinematic slip models. The grid size of kinematic models ranges typically between 1 km and 5 km. In our finite difference computation, it was necessary to use a grid size ranging from 0.08 km to 0.4 km to be certain to resolve the spatial cohesive zone and to exclude any artificial complexity [see chapter 5]. Our temporal step ranges between 0.008 s to 0.04 s depending on the earthquake model.

We used the following spatial interpolation and smoothing scheme. Usually, each kinematic slip model consists of a 2D grid of subfaults. Slip within each subfault occurs in one or more time windows. During each time window the subfault's slip velocity function is specified by the modeler to be a simple function like a triangle. For each subfault, each time window follows the preceding by a given constant time interval. The initiation times of the first and subsequent time windows for a particular subfault are delayed by some time interval to account for rupture propagation from the hypocenter to the subfault.

For example, a collection of kinematic slip models can be found in http://pasadena.wr.usgs.gov/office/wald/slip_models.html, compiled by D. Wald; in this site, the slip distribution of the 1994 Northridge earthquake, for instance, inferred by Wald et al. [1996] inverting strong motion data, is given in three different time windows.

The goal of our interpolation is to develop a spatially and temporally smoothed version of the kinematic model, sampled on a dense spatio-temporal grid, preserving the rupture propagation and the seismic moment of each subfault. Consider a slip model with only one time window. The multi-time-window algorithm is a straightforward extension. Let the centers of each subfault be at positions $\mathbf{x}_i, i = 1, N$, let the moment of the i th subfault be M_i^K , and let A_i denote the spatial region of the i th subfault. Let $u(\mathbf{x}_i)$ be the total strike-slip component of slip in the i th subfault of the kinematic slip model for that time window. We pad the periphery of the u function with two rows and columns of zero slip, and we raise N accordingly. Let $\mathbf{y}_i, i = 1, L$ be the denser set of locations where interpolation is desired. Spatial smoothing is achieved when we determine $u(\mathbf{y}_i), i = 1, L$ by bicubic interpolation of $u(\mathbf{x}_i)$. This step of the interpolation does not modify the original slip values. However, if we calculate M_i^I , the moment of the interpolated function integrated over the extent A_i of the i th subfault, we find that $M_i^I \neq M_i^K$. We iteratively modify the kinematic slip model until acceptable agreement is achieved, as follows. For each subfault we create modified kinematic model $u'(\mathbf{x}_i) = u(\mathbf{x}_i)M_i^K / M_i^I$. Then we interpolate the modified kinematic model, and check the moment ratio, repeating the process until satisfactory convergence is achieved. In practice this algorithm works very well for subfaults with large or moderate slip but always introduces moment into kinematic subfaults originally having zero moment and having neighboring subfaults with nonzero moment. However, these are the subfaults which are least likely to be resolved in the kinematic slip model and we do not interpret them in our analysis to infer the

constitutive behavior. The iteration does not introduce negative slip because the modification is made with a product between positive quantities. When the kinematic model has two component of slip (strike slip and dip-slip) the iteration is made with the magnitude of the slip on each subfault. Then we set $u'_{strike}(\mathbf{x}_i) = u'(\mathbf{x}_i)u_{strike}(\mathbf{x}_i)/u(\mathbf{x}_i)$ and $u'_{dip}(\mathbf{x}_i) = u'(\mathbf{x}_i)u_{dip}(\mathbf{x}_i)/u(\mathbf{x}_i)$ to preserve the original rake angles. This procedure does not introduce more information [i.e. heterogeneities] at scales smaller than the minimum kinematic resolved length [Mai and Beroza, 2002; Lavallée and Archuleta, 2003]. In other words, we still have the resolution given by the kinematic inversion. Figure 1 shows the comparison between the original slip model and our interpolated slip distribution for the 1994 Northridge earthquake. The two color bars in Figure 1 emphasize that the maximum slip value on the fault is different (2.99 m in the original model, 3.2 m in the interpolated model) because the preservation of each subfault's moment forces us to change the original slip values.

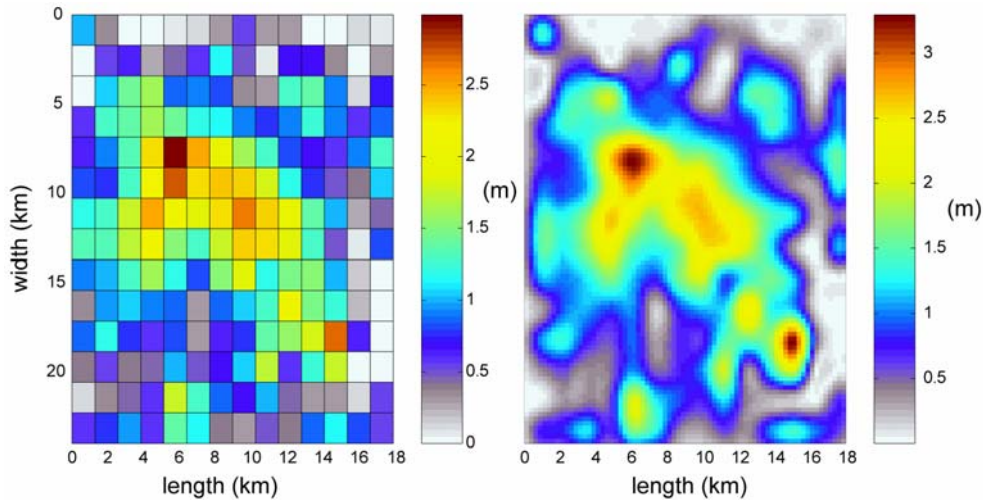


Figure 1: Slip distribution on the fault plane of 1994 Northridge earthquake. Left panel: the original slip distribution inferred by Wald et al. [1996] from the joint inversion of near-source strong ground motion, teleseismic and GPS data. Right panel: the same slip distribution interpolated by bicubic interpolation preserving the seismic moment of each kinematic subfault.

To introduce rupture propagation into our interpolated model, we use bicubic interpolation to derive interpolated rupture time from the kinematic rupture time $t_r(\mathbf{x}_i)$. A slip velocity time function is assigned to each interpolated

point by linear interpolation of the kinematic SVF (typically a triangle), and temporal smoothing is achieved by convolution with a rectangular (boxcar) function, i.e. by calculating the running mean. When the kinematic model has a complex analytical SVF (i.e. square root or \tanh function), the slip velocity time function is inferred by computing the analytical equation at each assigned time step. A similar interpolation process was used by Day et al. [1998], except that they used biquadratic interpolation and they did not preserve moment in the subfaults.

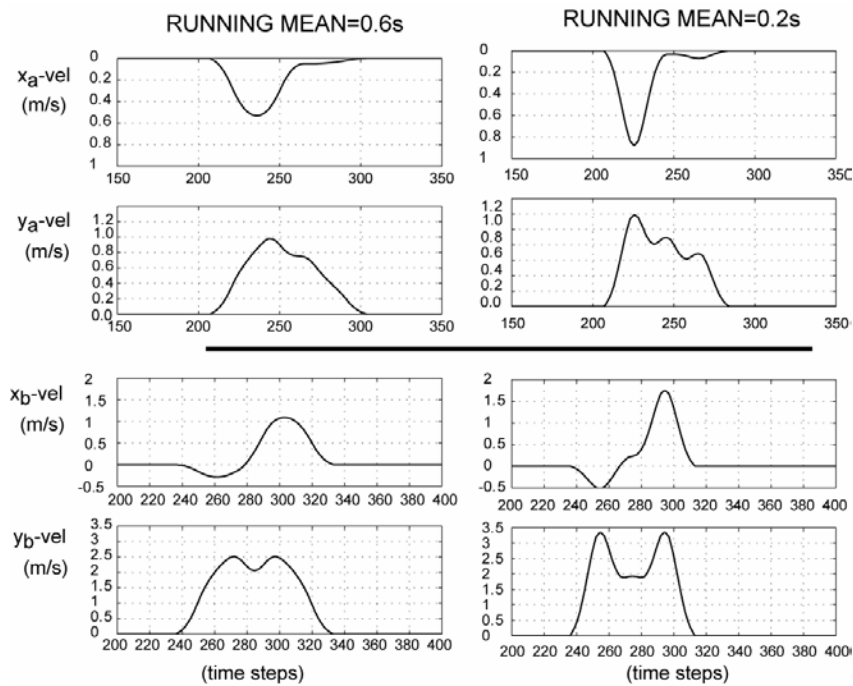


Figure 2: Effect of running mean (pass-band filtering) on the two components of slip velocity function for two target points on the 1994, Northridge earthquake model. In the left column the slip velocity functions are smoothed by taking a running mean of $T_{\text{box}}=0.6$ s width, equal to the triangular window duration; on the right column the slip velocity functions are smoothed with a $T_{\text{box}}=0.2$ s running mean.

The duration of the box-car function, T_{box} , represents the cut-off frequency, i.e. the box-car is a low pass filter. The T_{box} value strongly affects the slip velocity evolution for single window source models [i.e. analytical function] as well as for multi-windows models [i.e. several triangular functions]. The slip images were derived using only relatively long-wavelength observations and we have to be

Careful choosing the size of smoothing operator. When we decide the window for the running mean we should not preserve frequencies that were not inverted or modeled to fit the waveforms and to get the slip model. However, it is also true that we have to sample the slip velocity function in order to guarantee that not only the seismic moment but also the peak slip velocity is maintained. If we increase the running mean duration we might not fit the peak values of the slip velocity functions used to invert the data. In Figure 2 we give an example of effects of different T_{box} for Northridge slip model. We have chosen two points and we plot the two components of slip velocity using $T_{\text{box}}=0.2$ s ($f=5$ Hz) and $T_{\text{box}}=0.6$ s ($f=1.67$ Hz). We can see the effects of running mean on peak slip velocity, total rise time and shape. On the smoothest slip velocity evolution, the peak values are smaller and shifted in time. In our computation we have compared two different running means also for the Imperial Valley: $T_{\text{box}}=0.3$ s ($f=3.3$ Hz) and $T_{\text{box}}=0.5$ s ($f=2$ Hz). We will show the effects of the running mean on inferred traction evolutions.

6.3 Kinematic Models

We describe in this section the main characteristics of each model investigated in this study. The original kinematic model comes from distinct inversion techniques (multi-window as well as single window) and from many different authors. Details can be found in the respective papers.

Earthquake	Seismic Moment (Nm)	Fault dim. (L x W) km	Average slip (m)	Max slip (m)	Average rupture velocity (km/s)	Slip velocity function	Running mean (s)
Imperial Valley Hartzell and Heaton 1983	8.64e+18	42 x 10.5	0.6	2.194	2.6	1 triangle win. ($\tau_R=0.7$ s; $\tau_{V\text{peak}}=0.2$ s)	0.3 – 0.5

Earthquake fracture energy

Landers-WH Wald & Heaton 1994	9.26e+19	78 x 15	2.46	10.658	2.7	6 triang win. ($\tau_{R-1win}=1s$; $\tau_{delay}=1s$)	1 //
Landers-H Hernandez et al. 1999	1.02e+20	80 x 15	1.88	7.0202	2.6	Tanh funct. with variable τ_R	
Northridge Wald et al 1996	1.22e+19	18 x 24	0.985	3.297	~3	3 triangular win. overlap. ($\tau_{R-1win}=0.6s$; $\tau_{delay}=0.4s$)	0.2 – 0.6
Morgan Hill Beroza and Spudich 1988	2.62e+18	30 x 10	0.2462	2.732	~2	Truncated Kostrov function ($\tau_R=0.2s$)	0.16
Tottori Yagi	11e+18	24 x 14	0.992	2.1845	--	39 triangles ($\tau_{R-1win}=0.5s$; $\tau_{del.}=0.25s$)	
Sekiguchi	19e+18	28 x 17	1.1324	5.4278	~1.9	6 triangles ($\tau_{R-1win}=1s$; $\tau_{delay}=0.5s$)	//
Piatan.00	1.158e19	32 x 20	0.537	2.0862	~2.4		//
Piatan.01	1.1952e19	32 x 20	0.5543	2.6889	~2.7	Tanh (variable τ_R)	//
Vr=2.4km/s	1.1952e19	32 x 20	0.5543	2.6889	=2.0		//
Vr=2.km/s	1.1952e19	32 x 20	0.5543	2.6889	=2.4		
Kobe Wald 1996	2.44e+19	60 x 20	0.6196	3.831	2.8	6 triangles ($\tau_{R-1win}=0.7s$; $\tau_{delay}=0.4s$)	0.5
Colfiorito 0.33	4.381e+17	7.5 x 7.5	0.29	0.861	~2.2		//
Colfiorito 9.40	1.039e+18	12.5 x 7.5	0.415	1.777	~2.3	Tanh funct. ($\tau_R=1.s$)	
Colfiorito-ott Hernandez et al. 2004	6.478e+17	9. x 6.	0.4467	0.939	~1.8		
Synthetic tests (13 uniform models)	1.564e18	11.75 x 5	1	1	Constant on the fault. (from 1.5 to 3.0)	Smoothed Yoffe funct (τ_R constant on the fault; from 1.23s to 2.95s)	//

Table 1: Kinematic parameters of slip models here considered.

Landers Model (1992). We simplify the kinematic model given by Wald and Heaton [1994]. We incorporate the slip distribution on the overlapping parts of the three fault segments: Camp Rock/Emerson, CE (36 km long), Homestead Valley, HV (27 km long) and Johnson Valley, JV (30 km long). Between JV and HV there are 6 km overlapping and between HV and CE 9 km, so the resultant slip fault plane becomes 78 km long. We also simplify the Earth model to a uniform half space ($V_p=6.2$ km/s, $V_s=3.52$ km/s; density= 2.7 Mg/m³). The rupture time distribution is constant $V_r=2.6$ km/s. The slip velocity function (SVF) is represented by 6 isosceles triangles with a duration of 1s each (total rise time can reach at most 6 s). We use running mean $T_{\text{box}}=1$ s as Day et al. [1998] did. From the original 156 subfaults (considering the single fault) we interpolate with $dt=0.04$ s and $dx=0.4$ km obtaining 7448 subfaults. The kinematic model is a pure strike-slip mechanism.

To compare our inferred dynamic models, we also use the Hernandez et al.'s [1999] Landers model. They proposed a source model that consists of three distinct segments (30 km (CE), 25 km (HV) and 25 km (JV)), having small differences in strike directions. We simplify using a single plane 80 km long. In their single window approach they used a *tanh* function as SVF and they inverted for slip amplitude, rise time and rupture time. From their 48 square subfaults (16 along strike times 3 along dip, 5 km grid size) we obtain 19581 subfaults using 0.25 km grid spacing. Because the SVF is already smoothed, we do not apply the running mean.

Earthquake fracture energy

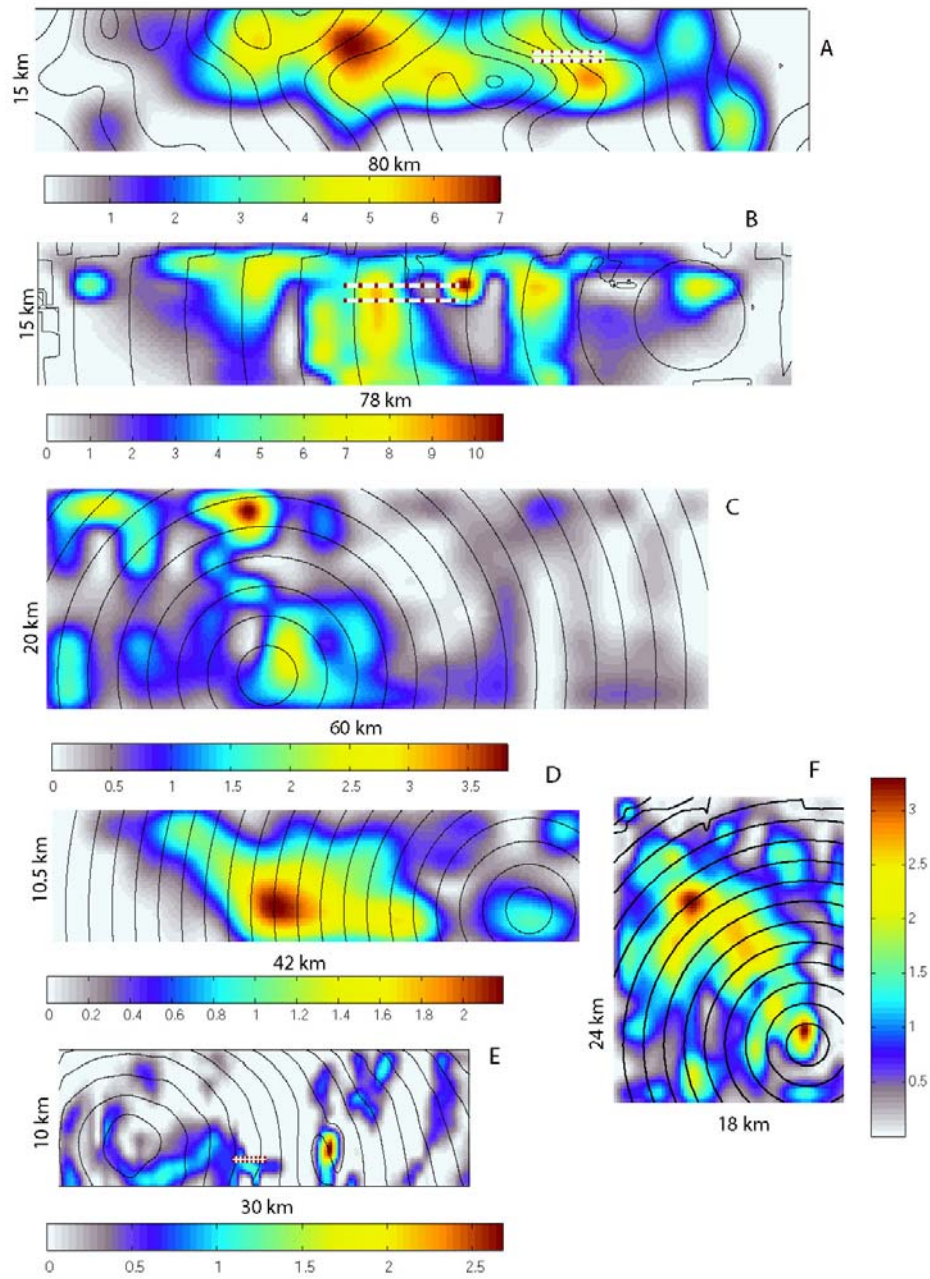


Figure 3a: The slip and rupture time distributions interpolated by bicubic interpolation of our models, A) 1992, Landers model by Hernandez et al. [1999]; B) 1992, Landers model by Wald and Heaton [1994]; C) 1995, Kobe model by Wald [1996] ; D) 1979, Imperial Valley model by Hartzell and Heaton [1983]; E) 1984, Morgan Hill model by Beroza and Spudich [1988]; F) 1994, Northridge model by Wald [1996]. The main features of these slip models are listed in Table 1. The red rectangles on panels A,B and E indicate the target points used for the plot shown in Figure 6. The color bar unit is meters.

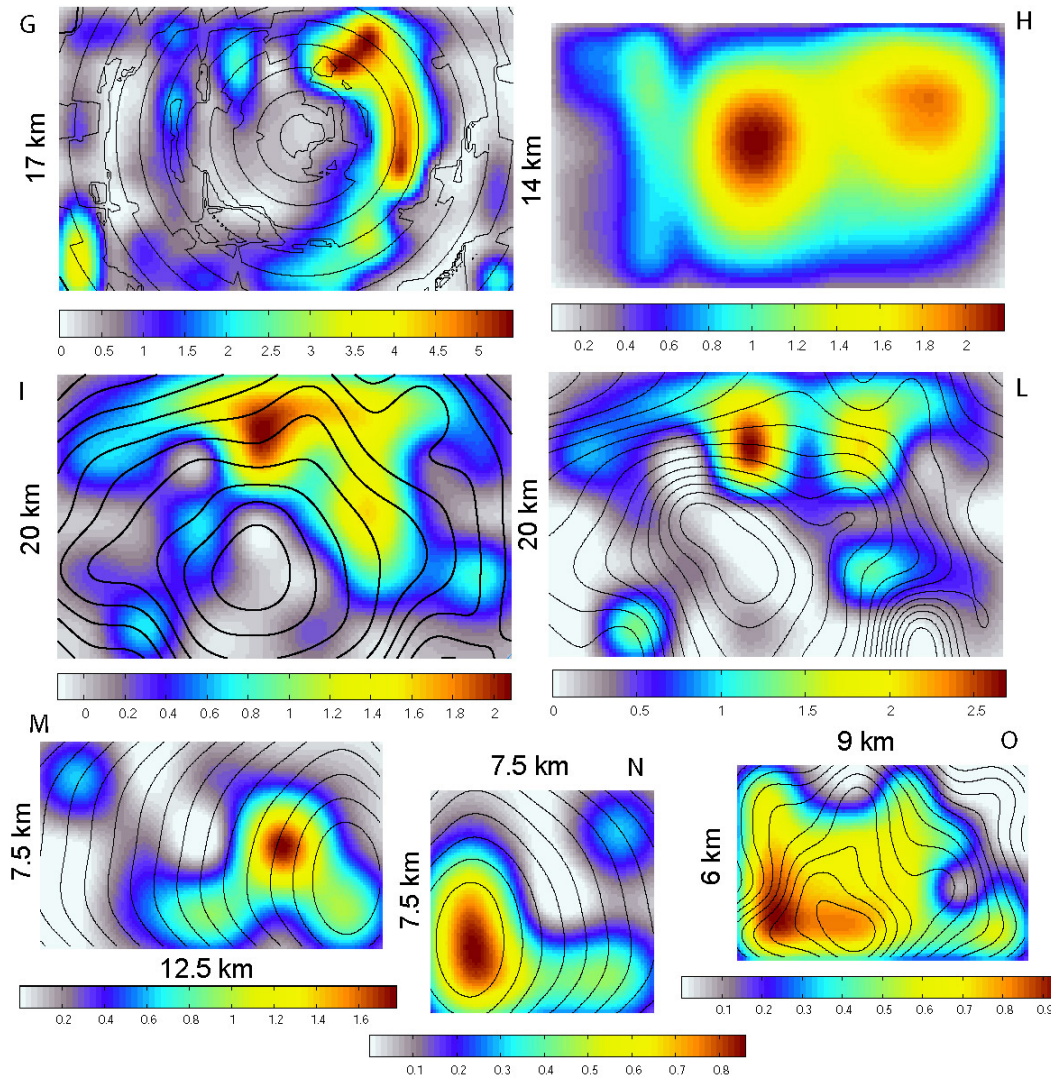


Figure 3b: G), H), I), L): 2000, Tottori model by Sekiguchi; by Yagi; by Piatanesi (model-00); by Piatanesi (model-01) ; M) N) O) 1997 Colfiorito models (three main shocks: September 26th 0940, September 26th 0033 and October 14th) by Hernandez et al. [2004]. The main features of these slip models are listed in Table 1. The color bar unit is meters.

Northridge Model (1994) We use the Wald et al. [1996] kinematic model. From 196 subfaults ($dx=1.2857$ km; $dy=1.7143$ km) we interpolate with a $dt=0.02$ s and $dx=0.25$ km obtaining 7081 subfaults. The SVF they used is represented by 3 isosceles triangles each having a duration of 0.6 s and having initiations separated by $\tau_{\text{delay}}=0.4$ s [i.e. they can provide a rise time lasting up to 1.4 s]. We rotate the original slip vector frame (155° and 45° components) into the strike and dip

components. This kinematic model contains temporal rake rotation and heterogeneous final slip direction. The average rake is 101° . The Earth model we employ is: $V_p=6.235$ km/s, $V_s=3.6$ km/s; density= 2.8 Mg/m³. We use running mean $T_{\text{box}}=0.6$ s (as Day et al. [1998]) and $T_{\text{box}}=0.2$ s to derive two different smoothed models [see Figure 2].

Imperial Valley Model (1979) We utilize the Hartzell and Heaton [1983] kinematic model. The SVF they used is an asymmetric triangular function having a rise time of 0.7 s and a time of peak slip velocity of 0.2 s. That is, the duration of positive slip acceleration is smaller than the duration of negative slip acceleration. We compare the effects of two different T_{box} : 0.3 s and 0.5 s. The Earth model we employ is: $V_p=5.6$ km/s, $V_s=3.14$ km/s; density= 2.7 Mg/m³. We have strike and dip components of slip velocity evolution. The kinematic slip model is divided into 56 subfaults, all 3 km long and 2.5 km width (excluded deepest subfaults, i.e. last row is 3 km width). In our model we obtain 7267 subfaults using 0.25 km grid size.

Morgan Hill Model (1984). Kinematic information is taken from Beroza and Spudich [1988]. The SVF they propose in their single window approach is the truncated Kostrov function. The rise time is constant everywhere and very small (0.2s). The Earth model we employ is: $V_p=6.0$ km/s, $V_s=3.469$ km/s; density= 2.7 Mg/m³. Our discretization interval is 0.08 km in space and 0.008 s in time. We are forced to use this small spatio-temporal discretization because of the rise time value.

Tottori Model (2000) We compare several different kinematic models from three different authors: (a) Yagi's model (reported in Mikumo et al. [2003]), (b) Sekiguchi's model (unpublished data, 2002) and (c) Piatanesi's models (unpublished data, 2004).

a) In their multi-window approach, they used 39 isosceles triangles with a duration $\tau_R=0.5$ s each, and with the initiations separated by $\tau_{\text{delay}}=0.025$ s. The first time window for each subfault initiated at the earthquake origin time, so no rupture

propagation was built into the slip model. We use running mean $T_{\text{box}}=0.5$ s. The Earth model we employ is: $V_p=6.05\text{km/s}$, $V_s=3.497\text{km/s}$; density= 2.7 Mg/m^3 .

b) In their multi-window approach, they used 6 non-overlapping isosceles triangles with a duration $\tau_R=1$ s each. The Earth model we employ is: $V_p=5.196\text{ km/s}$, $V_s=3.0\text{ km/s}$; density= 2.7Mg/m^3 .

c) Following Hernandez's single window approach, Piatanesi used a *tanh* function as the SVF and he inverted for slip amplitude, rise time and rupture time. The Earth model we employ is: $V_p=6.05\text{ km/s}$, $V_s=3.497\text{ km/s}$; density= 2.7 Mg/m^3 . Our discretization interval is 0.15km in space and 0.015s in time. Among many models he tested, we chose two models (model-00 and model-01) that equally fit the strong motion data. Further, we computed the dynamic model using the slip distribution of the model-01 with two different constant rupture velocity distributions ($V_r=2\text{ km/s}$ and $V_r=2.4\text{ km/s}$). The hypocenter is the same in the four Piatanesi models.

Colfiorito Model (1997) The kinematic information has been taken from Hernandez et al. [2004] model. Actually, under the name of Colfiorito 1997 we consider three main shocks: 00.33 September 26th, 09.40 September 26th and the 15.23 October 14th. The authors follow the single window technique and use the tanh analytical function, which corresponds to a smoothed ramp in slip evolution. They used a constant rise time, 1 s, for all three events. From their 9, 15, 24 subfaults for the three events we obtain 5776, 9576, 5551 subfaults using 0.1 km grid size. The Earth model we employ is: $V_p=5.5\text{ km/s}$, $V_s=3.055\text{ km/s}$; density= 2.8 Mg/m^3 .

Kobe Model (1995) Details of this model are in Wald [1996]. The original model is composed of two fault segments: Nojima (20 km long, strikes 45°) and Suwayama (40 km long, strikes 50°). We simplify it considering a single fault surface. His SVFs were 6 isosceles triangles. The duration of each triangle is 0.7 s and the time delay is 0.4 s. We use a 0.5 s running mean because he low-pass filtered the data at 2 s. The rupture velocity is constant at 2.8 km/s. The original model had 144 subfaults and after the interpolation we had 19521 node points,

using uniform 0.25 km grid spacing. The Earth model we employ is: $V_p=6.0$ km/s, $V_s=3.46$ km/s; density= 2.7 Mg/m^3 .

The most important kinematic parameters of all the models considered in this study are listed in Table 1. In Figure 3a and Figure 3b we show all the interpolated slip and rupture time distributions.

6.4 Breakdown work estimates

The traction evolutions we infer from kinematic models can be very complex as shown schematically in Figure 4b. Noisy seismic data, inadequate inversion techniques and possibly complicated friction mechanisms can cause this complexity. Depending on the assumptions in the kinematic models, the slip-stress relations can show either a linear weakening phase or extremely variable weakening behavior and sometimes, in subfaults with small slip, only a strengthening behavior. In particular, the identification of a kinetic frictional level [i.e., a nearly constant traction level for increasing slip, as shown in Figure 4a] is not straightforward for stress-slip curves derived from real data.

As we will explain in the following, the term “fracture energy” has been used with different definitions in different contexts; to avoid this ambiguity we define and compute three new quantities: breakdown work, restrengthening work and excess work. We define the excess work W_e to be the sum of breakdown work and restrengthening work (W_b and W_r , respectively, see Figure 4b). Breakdown work is taken to be the excess of work over the minimum magnitude $\bar{\tau}_{\min}$ of traction during slip. We compute breakdown work (W_b) as the integral of the traction versus slip curve from zero slip to the point where the traction drops to $\bar{\tau}_{\min}$.

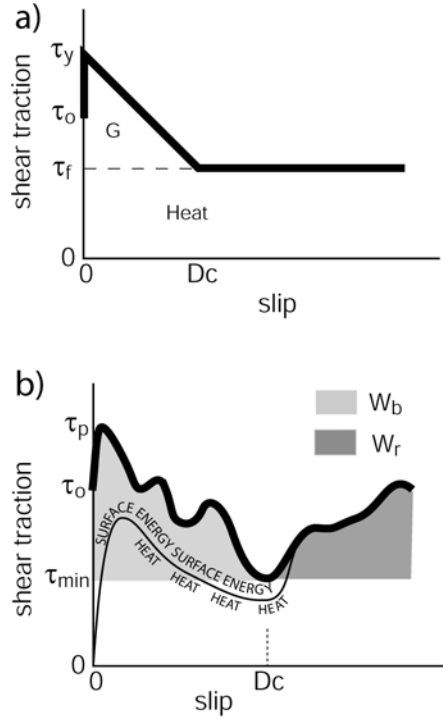


Figure 4: Theoretical traction versus slip curves (heavy black lines). The upper panel shows the “classic” slip weakening law with a linear slope (Ida, 1972 and Andrews, 1976). The dashed line represents the frictional level and the boundary between heat and surface energy. The lower panel shows a schematic, more complex weakening behavior we might infer from noisy real earthquake data. The dashed line represent the minimum level of the traction magnitude during slip. W_b and W_r are the breakdown and the restrengthening work. The thin black line shows that the actual balance between surface energy and heat might vary with slip and can lie above or below the minimum traction level.

Analytically we can write for each point on the fault

$$W_b = \int_0^{T_b} (\bar{\tau}(t) - \bar{\tau}_{min}) \cdot \bar{v}(t) dt \quad (6.1)$$

where $\bar{v}(t)$ is slip velocity; $\bar{\tau}(t)$ is shear traction; T_b is the time at which minimum traction $\bar{\tau}_{min}$ is reached at the point. (Strictly speaking, W_b is an energy density (J/m^2), but here we just call it breakdown work for simplicity.) The scalar form of (6.1) is G_c . For a classical slip-weakening model [e.g. Figure 4a], $\bar{\tau}_{min}$ is the kinetic friction level $\bar{\tau}_f$ and T_b is the breakdown time. We use the formulation with slip velocity (integrated in time), and not directly with slip, because in the finite difference code stress and slip velocity are computed at the same instants in

time. In this way we obtain the distribution of W_b on the fault. Moreover, we can also infer a slip weakening distance D_c , displayed in Figure 4b, as the slip at the time when minimum traction $\bar{\tau}_{\min}$ is reached. A similar equation defines a quantity we call restrengthening work,

$$W_r = \int_{t_b}^T (\bar{\tau}(t) - \bar{\tau}_{\min}) \cdot \bar{v}(t) dt \quad (6.2)$$

where T is the total duration of slip at the point, where W_r is again an energy density. The reason that we define the breakdown work W_b is relatively simple: the shaded area drawn in Figure 4b and computed through equation (1) is the energy density (or work) spent to allow the rupture to advance. For real earthquakes, it might contain an indefinite mixture of heat and surface energy as schematically illustrated in Figure 4b. In other words, the boundary between heat and surface energy probably does not lie along a horizontal line at $\bar{\tau}_{\min}$ (as in Figure 4a). Thus, our breakdown work probably contains an unknown mixture of heat and surface energy (energy that goes into fracture and gouge formation). This means that the breakdown work, or a large portion of excess work, may be expended in both heat and gouge formation/evolution during dynamic slip episodes.

For these reasons, we also believe that it might be misleading to call the quantity calculated in equation 6.1) “fracture energy”. As mentioned earlier, this term has different meanings in different contexts. In fracture mechanics, fracture energy is the energy consumed at the crack tip to create a surface without incurring any slip. Ida [1972] introduced the slip-weakening model of friction (Figure 4a) to remove the stress singularity at the crack tip, and the total energy under the linear weakening part of the curve and above the kinetic friction level τ_f was called the fracture energy because it played the same role as fracture energy in fracture mechanics, absorbing energy near the crack tip and controlling rupture speed [Andrews, 1976]. Olgaard and Brace [1983], Wilson et al. [2004], and Chester and Chester [2004] have estimated fracture energy for real faults by estimating the total surface area in gouge zones. Guatteri et al. [2001] and Ide [2003] estimated

fracture energy (similar to our breakdown work) by integrating the work under the weakening portion of a traction-slip curve determined seismologically. The ambiguity of terminology arises because it is not clear that all of our breakdown work controls the rupture speed, particularly at points where D_c approaches total slip, and thus breakdown work might not be equivalent to the Ida/Andrews fracture energy. In other words, when D_c is 8m, as in some models of Landers below, the breakdown work incurred going from the 7th to the 8th meter of slip might have no effect on the local rupture velocity. Moreover, the breakdown work (or “fracture energy” in the widely adopted meaning) that determines rupture velocity needs not to be surface energy, since heat generated in the vicinity of the rupture front contributes to controlling rupture propagation.

6.5 The choice of the initial stress

Because absolute initial traction $\bar{\tau}_0$ is part of the total traction $\bar{\tau}(t)$, it is necessary to choose an absolute initial traction in order to perform the above calculations. If slip rake did not rotate with time in the kinematic models, the initial traction could be chosen to be collinear with the slip vector, and the breakdown work and restrengthening work would be independent of the magnitude of the initial traction. However, traction and slip velocity are two-component vectors, and in some of our kinematic rupture models both slip velocity and traction rotate independently with time, in an uncorrelated, unphysical fashion due to inversion errors.

Consequently, it was necessary to choose an initial stress magnitude sufficiently large ($\bar{\tau}_0 = 5.e9$ Pa) to minimize the angle between the total traction and the slip velocity. We also assumed that the initial traction is collinear with the final slip. Among different choices for initial traction direction, this direction is the most physically meaningful. First, at points with no rake rotation, the initial traction and total traction during each time step are along the direction of slip. Second, if slip direction is heterogeneous on the fault our choice allows a

heterogeneous distribution of initial stress direction as well as traction evolution and final traction direction. Third, if there is temporal rake rotation, the huge initial magnitude prevents large rotations of traction vector, maintaining overall collinearity of slip and traction. Obviously, our assumption of initial stress controls only the coupling of traction components and not the absolute value of dynamic friction and heat contribution. The knowledge of the true magnitude of initial stress is only possible for kinematic slip models in which temporal rake rotation is well determined in the kinematic model, as in Spudich et al. [1998].

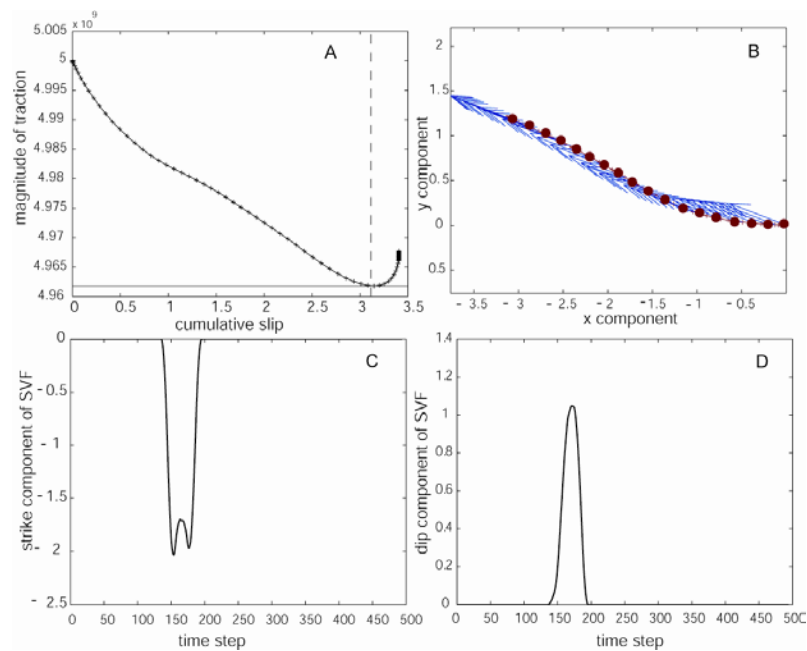


Figure 5: Example of a slipping point with rake rotation for the 1995, Kobe earthquake model. Panels C & D show the two components of slip velocity function at this point. Panel B shows the path covered by the slip (red dots) and the total traction evolution (blue arrows) at various time steps, assuming initial stress along final slip direction. The panel A shows the magnitude of traction versus cumulative slip, i.e. the inferred dynamic weakening behavior.

In Figure 5 we show how our choice of initial stress brings slip velocity and total traction into alignment for most of the temporal evolution. Panels C and D show the evolution of the two components of slip velocity at a point having rake rotation in the 1995 Kobe earthquake. The red dots in panel B represent the slip and the blue arrows are the total traction vector at various time steps (the axes represent the strike and dip components). When rake rotates, we calculate the cumulative

slip by integrating along the slip path. In panel A we show the inferred traction evolution that we discuss in the next section.

6.6 Results

We discuss in this section the inferred evolution of total dynamic traction as a function of time or slip for the different slip history models presented above [see Figure 3 and Table 1]. We also show several examples of dynamic traction and slip velocity that are useful for the discussion in the following sections.

6.6.1 The inferred constitutive behavior

Figure 6a, 6b and 6c show the examples of the inferred traction and slip velocity evolutions for the Morgan Hill and Landers earthquakes. We plot slip velocity evolutions (top two rows), traction change histories (middle two rows) and slip-stress relations (bottom two rows) for neighboring points on the fault (whose position on the plane is indicated on the figure). All quantities are the strike components because these models have a pure strike mechanism. These figures reveal a large variation in constitutive relations (i.e. the traction evolution) from model to model and even between neighboring points, but in general we observe a clear weakening behavior. We can see in Figure 6a that the breakdown process (middle two rows) for the Morgan Hill model is very fast due to the very short rise time of the assumed truncated Kostrov function. Although in those points having a large final slip the slip-stress relations show an evident weakening behavior, this is not guaranteed for all points on the fault. The D_c values are a large fraction of local final slip.

Figure 6b and 6c show the inferred dynamic traction evolution for Landers earthquake using two different kinematic models: Hernandez et al. [1999] and Wald and Heaton [1994]. Different parts of the fault are shown in Figures 6b and 6c. Apart from this, the great difference comes from the kinematic input: the Hernandez model has very smooth slip velocity histories while the Wald model shows very heterogeneous and variable slip velocities. The corresponding traction

evolutions follow the features of the kinematic input. In Figure 6c we can see that the dynamic traction drops during the slipping phase almost everywhere and grows in a small number of points showing a negative stress drop. The critical slip weakening distance D_c and breakdown work estimates are easily computed in the Hernandez model. On the contrary, the traction evolutions of the Wald and Heaton model are highly variable and sometimes difficult to interpret, particularly for estimates of D_c and $\bar{\tau}(t)$. This raises the question of what is believable in these models. The shapes of each model's traction evolutions are strongly controlled by the chosen SVF (in agreement with the results of previous chapter). The slip maxima are sometimes located in different places in different models, usually because there is a tradeoff between the spatial and temporal locations of the sources of observed ground motion pulses, so a detailed interpretation of the exact locations of slip maxima might not be warranted. The kinematic rupture models must have approximately correct amounts of breakdown work and slip in order to have the moments and rupture velocities necessary to model the waveforms. This is a first-order requirement. Thus, it is likely that these models have about the correct order of magnitude of breakdown work, despite variations in the details of the kinematic models.

Earthquake fracture energy

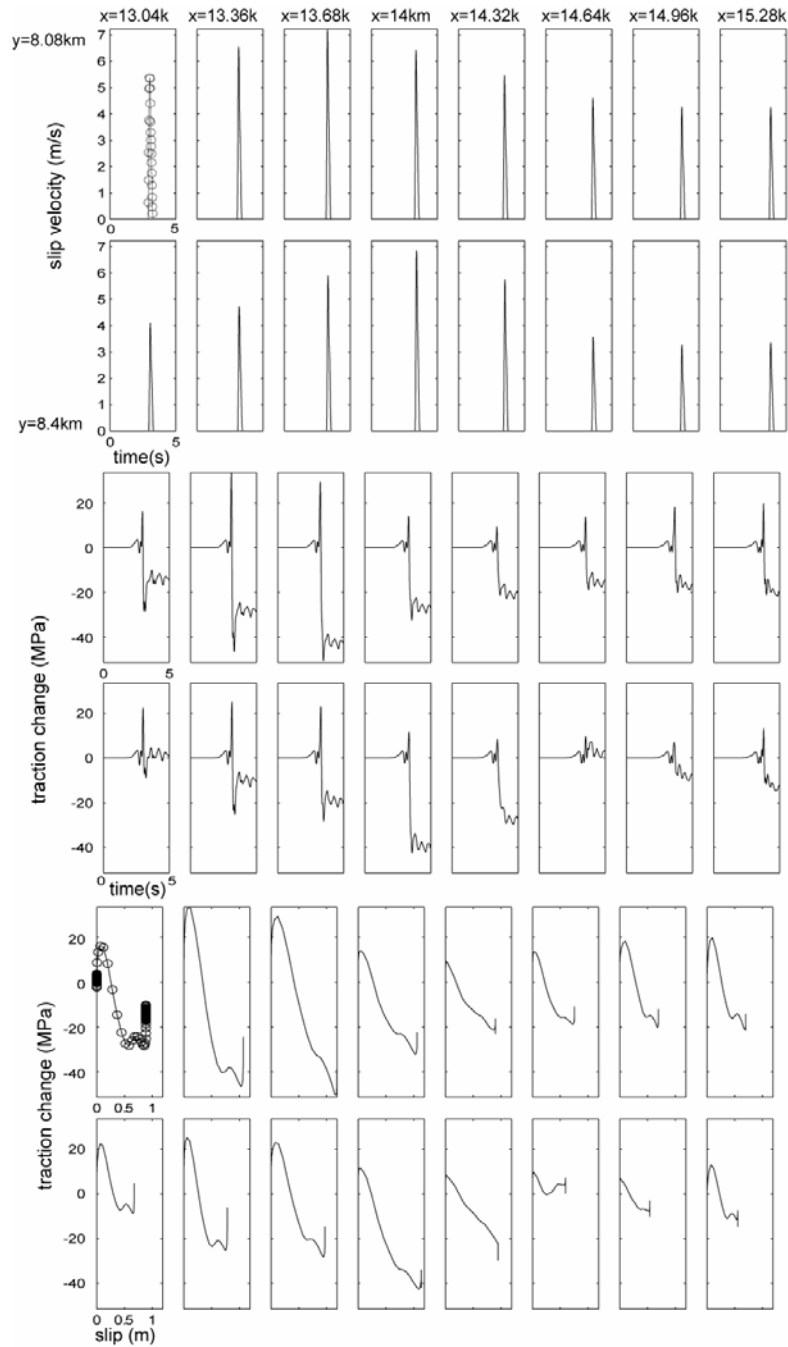


Figure 6a: The inferred dynamic model for 16 neighboring points (positions on the fault depicted in panel E of Figure 3a) of 1984 Morgan Hill model. Top two rows: slip velocity functions of the Beroza and Spudich [1988] kinematic model (they used a truncated Kostrov function). Central two rows: the inferred traction change time series for the same points. Bottom two rows: corresponding slip-stress relations. The circles on the first point represent the double time steps used on the dynamic procedure ($2dt=0.018$ s).

Earthquake fracture energy

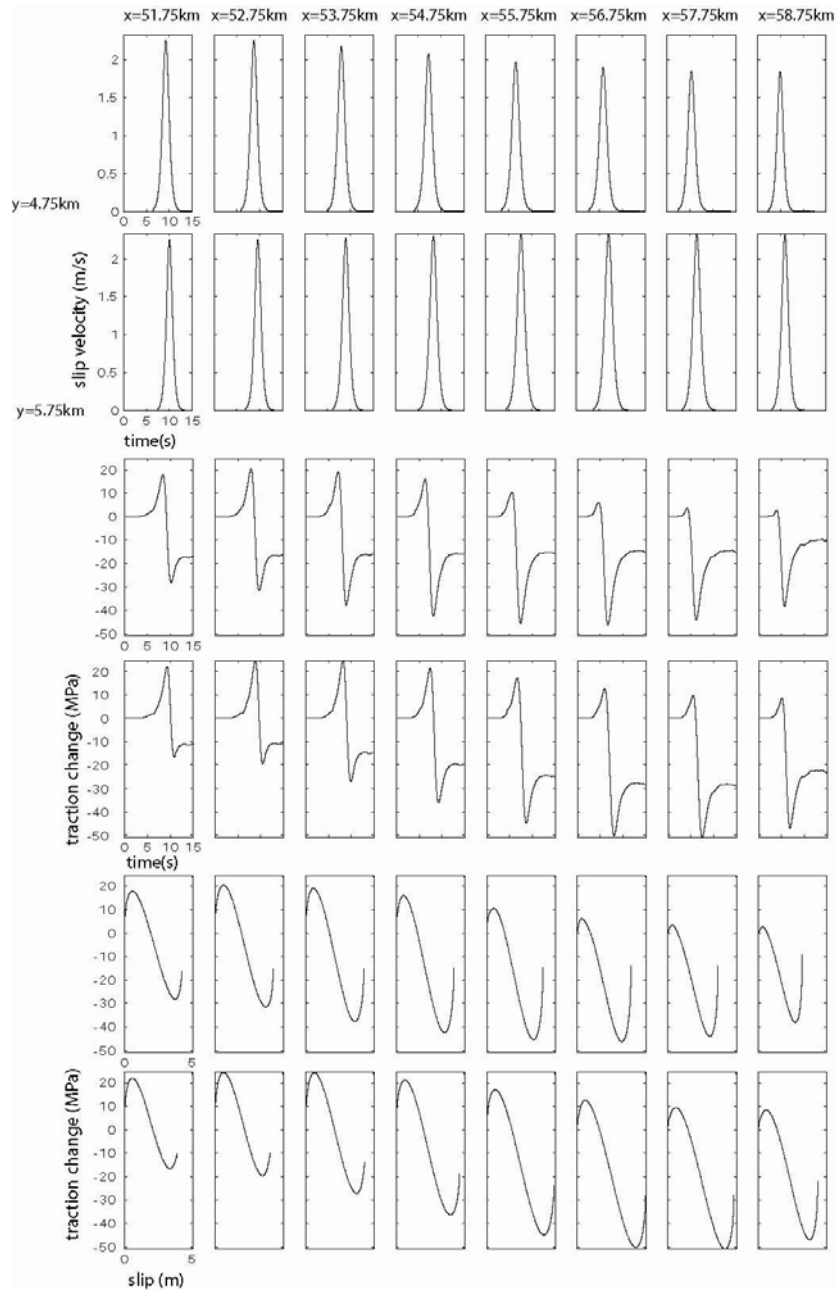


Figure 6b: The inferred dynamic model for 16 neighboring points (positions on the fault depicted in panel A of Figure 3a) of 1992, Landers model (Hernandez et al., 1999). Top two rows: slip velocity functions of the kinematic model (they used a tanh function). Central two rows: the inferred traction change time series for the same points. Bottom two rows: corresponding slip-stress relations.

Earthquake fracture energy

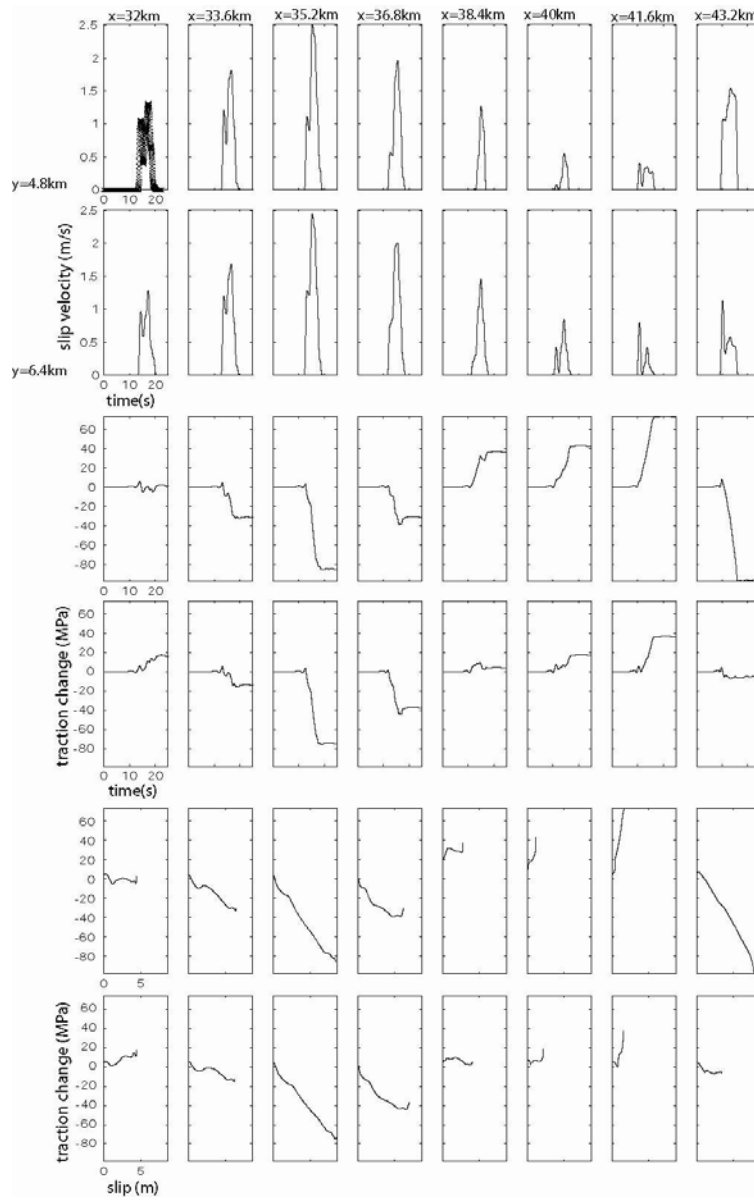


Figure 6c: The inferred dynamic model for 16 neighboring points (positions on the fault depicted in panel B of Figure 3a) of 1992, Landers model (Wald and Heaton, 1994). Top two rows: slip velocity functions of kinematic model (they used the multi-window approach with six triangular functions). Central two rows: the inferred traction change time series for the same points. Bottom two rows: the corresponding slip-stress relations. The circles on the first point represent the time steps used on the dynamic procedure ($dt=0.4$ s).

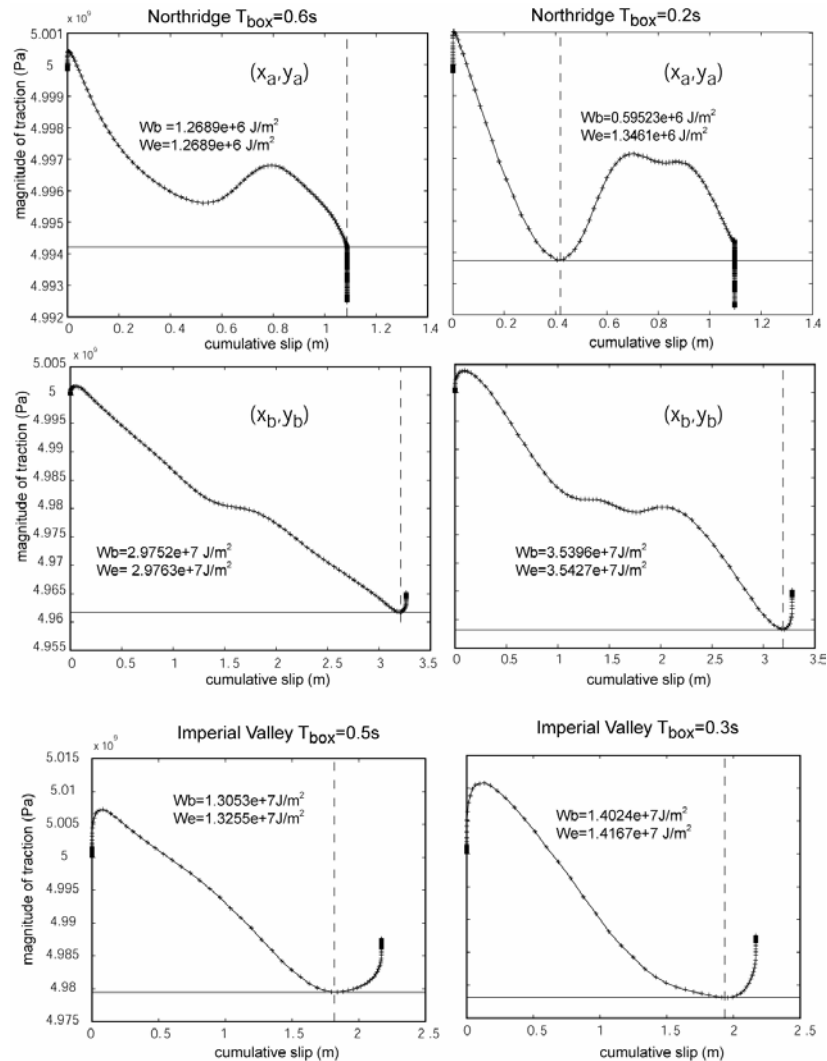


Figure 7: The inferred stress versus slip curves for the same points of Figure 2 (first and second rows) using two different running mean ($T_{\text{box}}=0.6$ s and $T_{\text{box}}=0.2$ s) of 1994, Northridge earthquake and for a target point of 1979, Imperial Valley model ($T_{\text{box}}=0.5$ s and $T_{\text{box}}=0.3$ s). The first two slipping points have rake rotation while the third does not. On each panel are annotated the local breakdown work density and the excess work density.

Figure 7 compares examples of constitutive behaviors for Northridge and Imperial Valley earthquakes using two different running means. Both earthquake models have two components of slip: Imperial Valley has only spatial variations of rake on the fault, while Northridge allows spatial and temporal rake rotation. On the top, for Northridge are points *a* and *b* whose slip velocities have been shown in Figure 2. On the bottom there is an example of Imperial Valley. We can see that

the total W_e estimates are less strongly affected by T_{box} than are the W_b estimates. The first example shows a point in which the variation of smoothing operator strongly changes the position of minimum traction. In point *a* the $T_{\text{box}}=0.6$ s allows the minimum traction to be reached at the end of slipping phase. The resulting ratios D_c/D_{tot} for the two choices of T_{box} are extremely different while the excess work estimates are still comparable. Like two of the three points in Figure 7, almost all the traction evolutions show a fast restrengthening after the weakening phase for the following reason. Because of the complexity of the kinematic slip history the traction is spatially very heterogeneous. In fact the temporal evolution of the traction on each subfault is strongly affected by the load of the neighboring subfaults, before, during and mainly after their slipping.

6.6.2 Breakdown work density distributions

Figure 8a and Figure 8b show the inferred W_b estimates for our fault models. The contours represent the slip distributions superposed on the W_b values. We observe that breakdown work densities W_b are strongly correlated with the correspondent slip distributions. In all models W_b is concentrated in high slip patches. The correlation between W_b and the slip distributions, first of all, is due primarily to the correlation of D_c with slip, but also secondarily to the correlation of stress drop with total slip. For each slip model we compute the average W_b over the fault, as well as the average of excess work density W_e to compare the results with those given in the literature. We calculate the integral contribution of excess work $E_e(\text{J})$ (excess energy) on the whole fault area, that is excess work density times the fault area. Table 2 summarizes the inferred W_e , W_b and E_e values for all earthquakes investigated in this study. In the fourth column we have written the same quantities relative only to the contribution of the part of fault having non-negligible slip, that is, slip larger than 20% of the average slip. The same quantities have been computed for the contribution of the asperities, that is patches of fault having slip larger than 90% of maximum slip. The corresponding areas are in the last column. Obviously the average slip and the maximum slip are different

Earthquake fracture energy

for each model and the ratio of these areas over the whole fault areas depends on the corresponding kinematic model.

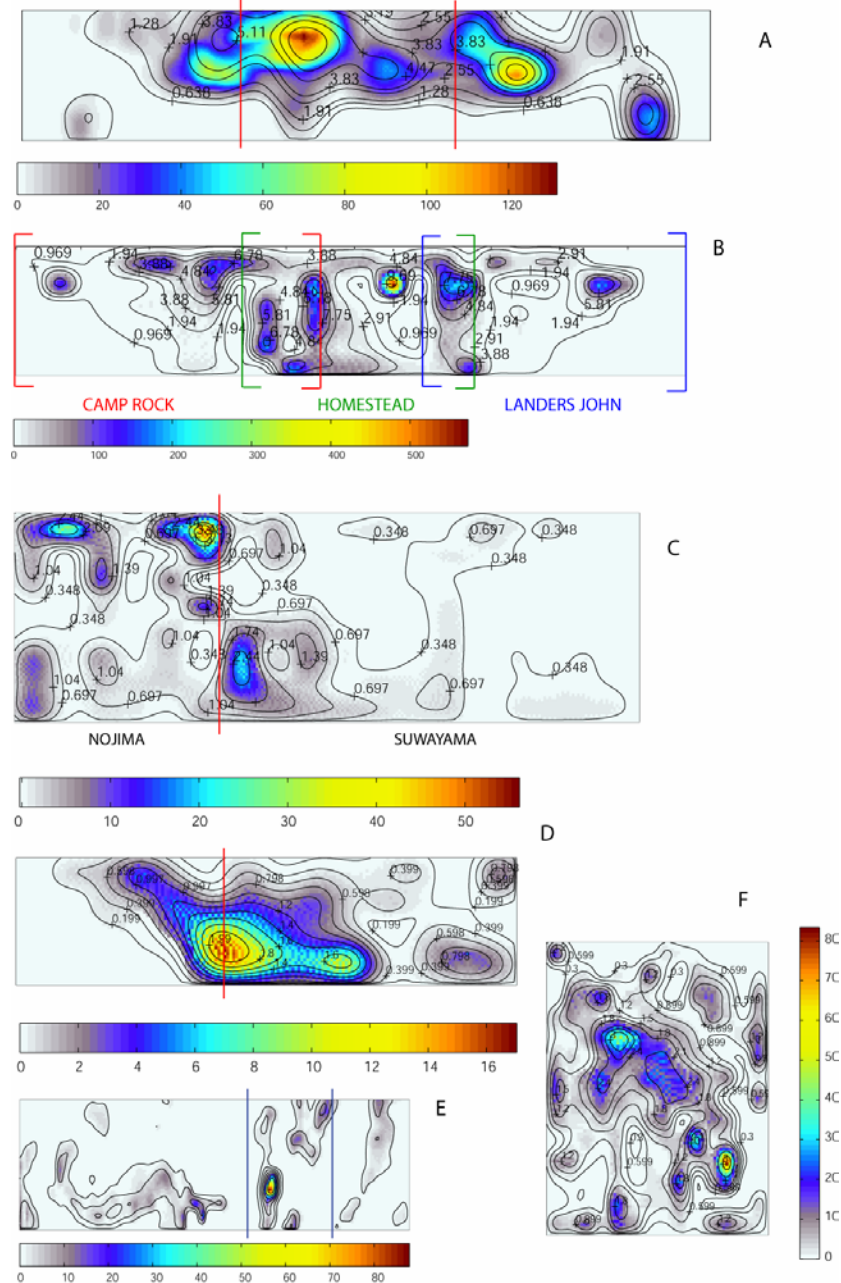


Figure 8a: Distributions of breakdown work densities (the color bar unit is MJ/m^2) for the same kinematic models shown in Figure 3a. Contour lines show the slip distribution and numbers indicate slip values. Vertical red lines show bends in the original kinematic fault models. Vertical blue lines in the Morgan Hill model show the segment of the fault for which the surface trace is quite complex. Matching color brackets indicate ends of fault planes in the Wald and Heaton model of Landers. Note areas of overlap.

Earthquake fracture energy

Earthquake	W_e (MJ/m ²)	W_b (MJ/m ²)	E_e (TJ)	>20% average slip		>90% maximum slip		Total	Area (km ²)	
				W_e (MJ/m ²)	E_e (TJ)	W_e (MJ/m ²)	E_e (TJ)		20%	90%
Imperial Valley										
T_{box}=0.3s	1.88	1.82	855.55	2.32	853.09	13.27	97.868	454.19	362.63	7.38
T_{box}=0.5s	1.80	1.73	818.5	2.25	816.04	12.60	92.914	454.19	362.63	7.38
Landers WH	21.53	20.26	25655	27.06	25593	473.88	606.56	1191.68	946.08	1.28
H	14.91	14.57	18245	21.50	18207	105.38	1547.8	1223.81	846.75	14.69
Northridge										
T_{box}=0.2s	6.15	5.75	2723.40	6.97	2709.4	48.15	129.4	442.56	388.94	2.69
T_{box}=0.6s	4.93	4.61	2179.90	5.57	2167.8	40.07	107.69	442.56	388.94	2.69
Morgan Hill	1.44	1.36	437.84	2.36	436.77	61.06	23.055	303.21	185.25	0.38
Tottori										
Yagi	1.88	1.69	650.98	1.99	650.24	5.34	55.43	335	345.56	10.37
Sekiguchi	7.66	7.13	3841.5	8.87	3829.5	8.06	483.62	476	501.44	6.
Piatan.00	3.15	3.02	2034.4	3.90	2031.0	12.21	107.7	653.06	525.38	8.75
Piatan.01	2.79	2.73	1801.9	3.52	1800.1	22.35	99.59	653.06	525.69	4.5
01-Vr=2.4km/s	2.59	2.51	1688.4	3.27	1685.7	17.19	77.331	653.06	525.69	4.5
01-Vr=2. km/s	3.39	3.30	2212.6	4.29	2210.1	20.70	93.162	653.06	525.69	4.5
Kobe	1.72	1.66	2100.6	2.03	2094.1	39.78	96.97	1220.06	1029.63	2.44
Colfiorito0.33ev	0.41	0.40	23.96	0.50	23.87	1.34	3.1398	57.76	48.06	2.35
Colfiorito9.40ev	1.02	0.97	97.99	1.27	97.60	9.62	10.77	95.76	76.76	1.12
Colfiorito-ott	1.14	1.11	63.46	1.32	63.27	4.47	8.80	55.51	48.01	1.97

Table 2. Inferred values of work density and total work.

It is useful to investigate the dependence of breakdown work on the running mean operation. Table 2 shows the results for the Imperial Valley and Northridge earthquakes using two different running means. Lowering the pass-band [i.e. lengthening the running mean duration: 0.5s for Imperial Valley and 0.6 s for Northridge] gives us smaller values of breakdown work. The main reason is the cut-off of high peak slip velocity values causes smaller strength excesses. This effect can be seen in Figure 7, and it differs from the observation of Spudich and Guatteri [2004] that low pass filtering might cause breakdown work estimates to

be biased upward. The downward bias we observe might explain some of the discrepancies in breakdown work we note below for the Landers earthquake.

6.7 Scaling relations between W_b and kinematic parameters

We can compare our estimates of breakdown work with fracture energies (G) inferred from recent works: Beroza and Spudich [1988] found $G \sim 2 \text{ MJ/m}^2$ for 1984 Morgan Hill earthquake; Guatteri et al. [2001] found $G \sim 1.5 \text{ MJ/m}^2$ for 1995 Kobe earthquake; Peyrat et al. [2001] found $G \sim 5 \text{ MJ/m}^2$ for 1992 Landers earthquake; Rice et al. [2004] found $G_{\min} \sim 0.88 \text{ MJ/m}^2$ for 1979 Imperial Valley earthquake, $G_{\min} \sim 1.3 \text{ MJ/m}^2$ for 1984 Morgan Hill earthquake; Ide [2003] found $G > 1.0 \text{ MJ/m}^2$ for 1995 Kobe earthquake. Our results are quantitatively consistent with these values, except for Landers earthquake. We obtain $W_e \sim 21.5 \text{ MJ/m}^2$ ($W_b \sim 20.3 \text{ MJ/m}^2$) and $W_e \sim 14.9 \text{ MJ/m}^2$ ($W_b \sim 14.6 \text{ MJ/m}^2$) for Wald and Heaton [1994] and Hernandez et al. [1999] models, which are respectively four and three times Peyrat's result. This is probably due to several factors; in particular, we observe strongly different D_c estimates between these models. A constant D_c of 0.8 m was imposed by Peyrat's model, while $D_c \sim 2\text{m}$ and $D_c \sim 1.6\text{m}$ are inferred from Wald and Heaton [1994] and Hernandez et al. [1999] models, respectively. The latter two values for D_c are only averaged on the fault plane but in these models D_c ranges widely, reaching as much as 10m. Probably these high values are due to the poor resolution of kinematic models, which prevent the weakening slope from being very steep. The discrepancies among the various breakdown work estimates for Landers might be indicating the limits of validity of Guatteri and Spudich's [2000] assertion that fracture energy can be stably estimated from ground motion data. They showed that two different rupture models, one with D_c of about 0.3 m and the other with D_c of about 0.8 m, having similar fracture energies, could produce nearly identical seismograms. The seismograms were very similar because breakdown work (i.e., fracture energy in Guatteri and

Spudich, 2000) controls rupture velocity, and rupture velocity strongly affects the ground motions. D_c in the models for Landers varies from 0.8 m to a maximum of 10 m, a factor of 12. The breakdown work expended far from the crack tip might have little influence on the rupture velocity, and thus have little effect on the ground motions. Thus, kinematic models with long D_c might tend to have systematically higher breakdown work than models with short D_c , even if both models match a ground motion data set. All of Peyrat's breakdown work is concentrated in the first 0.8 m of slip. That means that all of her breakdown work probably has a strong effect on her rupture velocity (in other words, it is fracture energy in the sense of Ida and Andrews). In Wald's model the breakdown work being expended in the last meter of slip might have no effect on the rupture velocity because the rupture tip is far from the healing front. A second factor might explain Peyrat's lower breakdown work. The shortest period Peyrat models is about 4s, so her model is a very low-frequency model. This corresponds to our observation that making the running mean longer lowers the breakdown work.

The dependence of W_b on rupture velocity is difficult to see because the slip distributions are strongly heterogeneous on the fault and they obscure the effects of V_r . Moreover the rupture velocity distributions of all models are almost constant [see Figure 3a and Figure 3b]. To test the relation between V_r and W_b we changed the original rupture velocity in the Piatanesi model-01.

Earthquake fracture energy

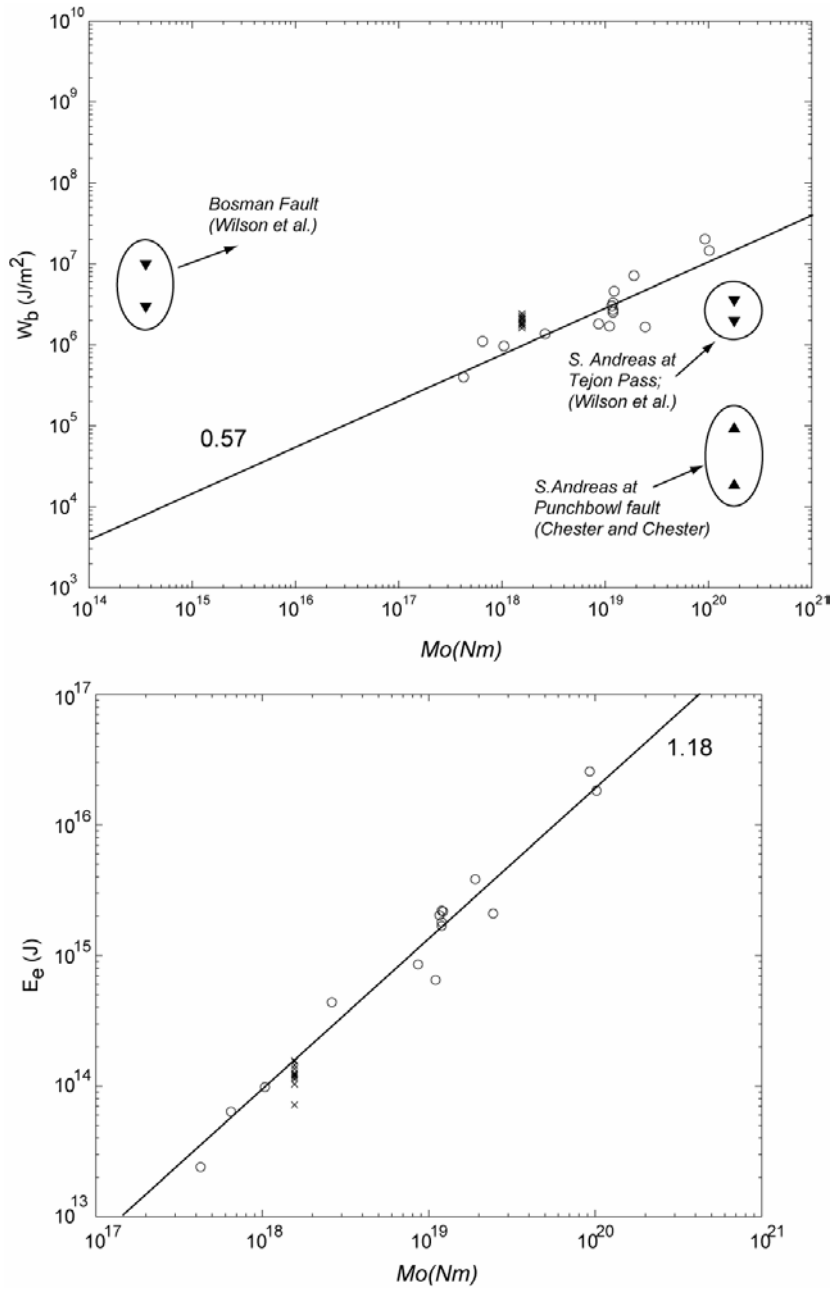


Figure 9: Breakdown work densities (top panel) and excess energies (bottom panel) versus seismic moment for all the earthquake modeled in this study. The open circles indicate W_b and E_e estimated for the set of real earthquake models, while the crosses represent the values inferred for a set of synthetic slip-pulse models. Solid triangles show the geological estimates of breakdown work densities proposed by *Wilson et al.* [2004] and *Chester and Chester* [2004]. The regression lines show power law scaling whose exponents are equal to 0.57 (on the top panel) and 1.18 (on the bottom). The latter exponent indicates almost a linear scaling.

We tried with two constant values: $V_r=2\text{km/s}$ and $V_r=2.4\text{km/s}$. The results in Table 2 confirm the theoretical expectation: the former has higher W_b values because each point has more time to break and to load the stress on each point on the fault. The yield stress distribution [i.e. strength excess] on the former is larger than the latter.

In the literature different scaling formulations have been proposed to compute fracture energy as a function of many dynamic and kinematic parameters [Husseini et al., 1975, Andrews, 1976; Nielsen and Madariaga, 2003; Rice et al., 2004]. Many of these estimates are global or average quantities that apply to point sources, while only few are referred to extended faults. The kinematic models used in this study are pulse-like rupture models, while many theoretical interpretations of scaling of G with V_r rely on crack models. Nielsen and Madariaga [2003] showed analytically the difference of G scaling relations between crack type and self-healing pulse. In Figure 9 we plot our W_b and E_e versus seismic moment M_0 . The crosses represent 12 synthetic models calculated in the previous chapter whose kinematic parameters are in the last row of Table 1. This set is composed of models having constant rupture velocity, constant rise time, constant slip and a self-healing SVF (a smoothed *Yoffe* function, see chapter 5). The lower panel shows almost a linear correlation between E_e and M_0 , while W_b values versus M_0 displayed in the upper panel follow a power law with slope equal to 0.57. An interesting feature emerging from this figure is that normal, thrust and strike slip earthquakes display the same scaling of breakdown work values with seismic moment.

The dependence of W_b on rupture velocity is well known in the literature (actually the literature shows G values depending on V_r in slip-weakening dynamic models), and thus the rupture velocity V_r should appear in the scaling relation. Rice et al. [2004] give a scaling relation for 2D slip weakening pulse models (steady state for the singular *Yoffe* solution, see also Nielsen and Madariaga [2003] and references therein), that we rewrite here for completeness:

$$G = \frac{\mu \Delta u^2}{\pi L} F(V_r) g(\theta) \quad (3)$$

where L is the spatial length of the pulse, $F(V_r)$ is a complicated function of V_r (different for Mode II and Mode III), and $g(\theta)$ is a function of R/L , where R is the length of the cohesive zone.

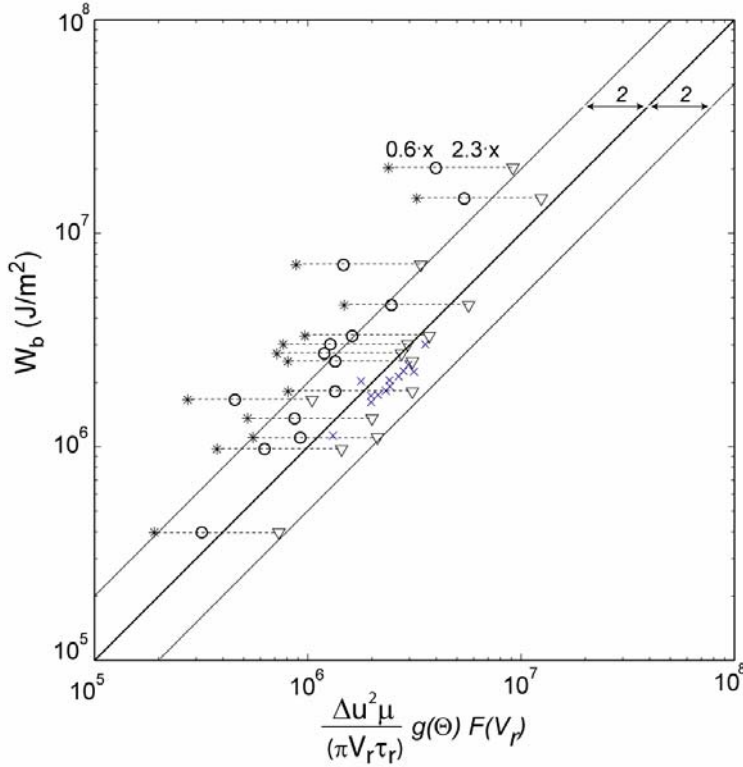


Figure 10: Breakdown work densities versus the right term of the Rice's equation (eq.3 in the text): the circles represent the real earthquake models, the crosses are the synthetic set models. The circles and crosses have the product $F(V_r) g(\theta)$ equal to unity. The triangles and the asterisks have the minimum and maximum value of $F(V_r) g(\theta)$ (0.6 and 2.3, respectively) when $0.6 < V_r/V_s < 0.8$. The solid lines represent the linear scaling between the plotted quantities.

We approximate $R \sim V_r T_b$, where T_b is the duration of the breakdown process, and $L \sim V_r \tau_R$, using the average values of V_r and τ_R on the fault. Thus θ depends on the observed quantity T_b/τ_R . Following the analytical solution of Rice et al. [2004] the product $F(V_r) g(\theta)$ can range from 0 to 2.6. Rice used this equation to infer average (i.e., global) values of G for each earthquake model.

The Rice et al. [2004] scaling relation describes our models well, which can be seen in a plot of our results for average quantities in Figure 10. The factors $F(Vr)$ and $g(\theta)$ are difficult to estimate for each kinematic model (especially for the multi-window models whose rise time can be strongly heterogeneous on the fault or for those models having variable rupture velocity). In Figure 10 the open circles have $F(Vr)g(\theta)$ equal to unity and represent the set of real earthquakes. We plot triangles and the asterisks corresponding to the minimum and maximum value of $F(Vr)g(\theta)$ (0.6 and 2.3, respectively) computed, according to Rice et al.[2004], for $0.6 < V_r/V_b < 0.8$ (which is a range including all kinematic models). The crosses represent the synthetic set. These models have been computed using the smoothed version of the *Yoffe* slip velocity solution from which Rice derived the equation; the inferred traction evolutions of these steady state pulse models have slip weakening behaviors (linear along spatial distance) with the assumed fast restrengthening due to the short duration of slip (self healing pulse, with constant rise time on the fault). The synthetic points are aligned close to the diagonal and we expect that the average value of the $F(Vr)g(\theta)$ product is very close to unity.

In order to further corroborate the agreement with the Rice scaling equation we compare our W_b estimates with the local slip values. Figure 11a shows the relation between the breakdown work and the total slip for each point on the dynamic fault model for the 1979 Imperial Valley earthquake model. The overplotted red function represents the quadratic dependence and the fit means $W_b \sim \Delta u^2$. The right panel of Figure 11a shows the relation between total slip and D_c . Many points are on the diagonal, [i.e., total slip is equal to D_c] while the most are just over the diagonal [i.e., D_c is a large fraction of total slip]. We tested this local dependence also for the 1995 Kobe and the 1997 October 14th Colfiorito earthquake models and we show the results on Figures 11b and Figure 11c. We also compute the Rice equation at the same depth of the hypocenter for Imperial Valley earthquake and we compare in Figure 12 the analytical predictions with our numerical calculations which show a very good agreement. These results confirm that our inferred values of breakdown work scales as the square of slip

($W_b \propto \Delta u^2$) and that the retrieved values of D_c are a large fraction of total slip suggesting a nearly linear scaling between these two parameters in lowpass filtered models. This might be an artifact of filtering.

We have checked for several earthquakes investigated in this study whether the W_b values shown in Figure 11 can be fitted also by the Andrews equation [see eq. 23 in Andrews 1976]. Our test demonstrated that this relation does not fit the inferred W_b values. In Andrews' equation fracture energy depends on the length of the crack from the nucleation point, which gives a poorer result than the use of the pulse length in Rice's relation. This might explain why our W_b data are better reproduced by the Rice's scaling relation.

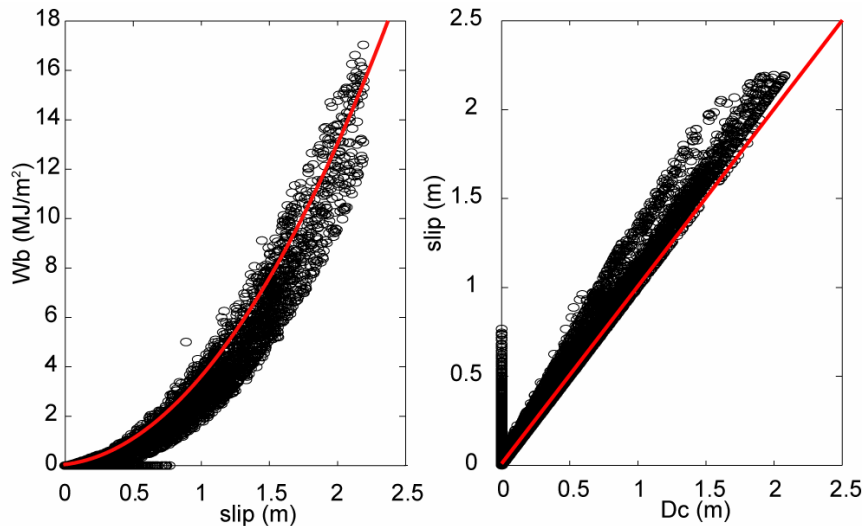


Figure 11a: Left panel: the breakdown work density versus total slip for each point on fault of the 1979, Imperial Valley earthquake model. The overplotted red line is a quadratic function. Right panel: the total slip versus the critical slip distance D_c [i.e., slip when the traction reaches its minimum value] for each point on the fault.

Earthquake fracture energy

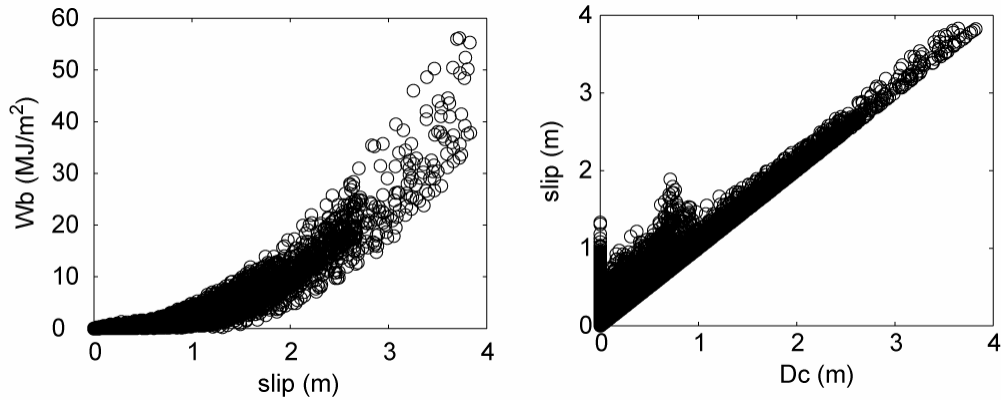


Figure 11b: Left panel: the breakdown work density versus total slip for each point on fault of the 1995 Kobe earthquake model. Right panel: the total slip versus the critical slip distance D_c for each point on the fault.

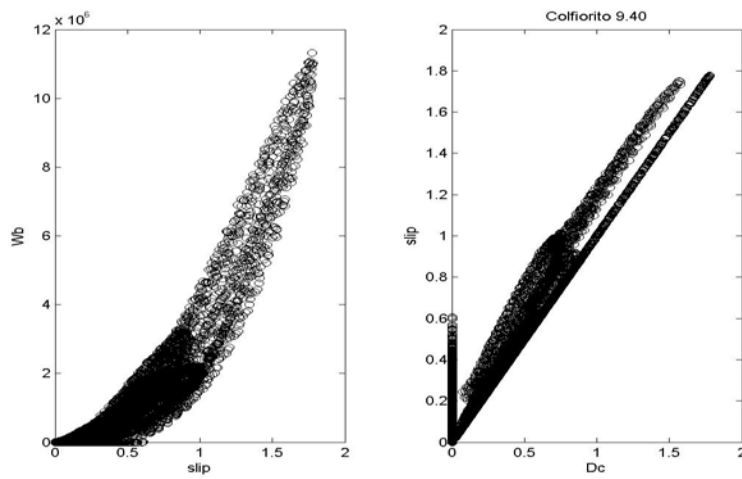


Figure 11c: Left panel: the breakdown work density versus total slip for each point on fault of the 1997, 14th October Colfiorito earthquake model. Right panel: the total slip versus the critical slip distance D_c for each point on the fault.

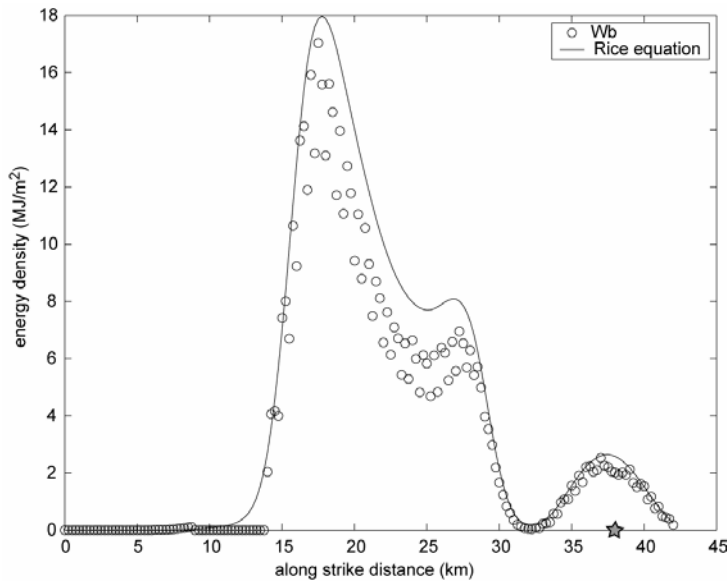


Figure 12: The circles are the inferred values of breakdown work along strike distance at the hypocenter depth of the 1979 Imperial Valley earthquake. The line represents the Rice equation computed for the points on the fault at the hypocenter depth, with the product $F(Vr)g(\theta)$ equal to unity.

6.8 Discussion

In this study we have estimated the breakdown work on extended faults for several real earthquakes. Our inferred values agree with previous seismological estimates of fracture energy G and fit a scaling relation recently proposed by Rice et al. [2004]. Our calculations reveal that work density and total work are spatially correlated with slip. We have treated breakdown work as being due totally to dynamic slip on an infinitesimally thin fault surface. Energy is absorbed within a zone a couple hundred meters wide in real faults. In a review paper Sibson [2003] gives a schematic representation of brittle fault zone: cataclastic damage zone (few m to 100m wide) containing a fault core of gouge or ultracataclasite (few cm to few m), within which there is a principal slip zone (1cm to 10cm). Our neglect of off-fault damage in our calculation does not bias our estimates of breakdown work; Andrews [2005] has shown that the energy absorbed in off-fault damage can be simulated by an equal amount of energy absorbed on the fault in a calculation lacking off-fault inelastic response.

Recent geological studies have estimated the surface energy dissipated both on and off the fault, considering the thickness of principal slip zone, off-fault damage, and the gouge grain size distribution. When we compare the geologic surface energies with our observed breakdown work, an interesting picture of fault mechanics arises. Chester and Chester [2004] estimated fracture and gouge surface area in the Punchbowl fault, an ancient trace of the San Andreas fault. They estimated that about 0.5 MJ/m^2 of surface energy would be used to create the 1 mm thick layer of ultracataclasites in the principal slip surface, and they estimated a single-earthquake surface energy to be about $0.02 - 0.1 \text{ MJ/m}^2$. This estimate results both from dividing the total surface energy of the entire Punchbowl fault zone by the tens of thousands of earthquakes thought to have created it, and by estimating the surface energy expended to refracture the 1-mm-thick principal slip surface. They pointed out that their single-event surface energy estimate is much smaller than the seismological estimates of breakdown work, implying that some of the seismological breakdown work must go into heat, i.e. the boundary between surface energy and heat must lie somewhere above the minimum traction level, as we have illustrated in Figure 4b. Studying the San Andreas fault at Tejon Pass, Wilson et al. [2004] estimate that 0.2 MJ/m^2 surface energy is needed to create a 1mm thick gouge zone (compared to the 0.5 MJ/m^2 estimated by Chester and Chester [2004]). They estimated that each major earthquake along the Tejon Pass section of the San Andreas generates 10mm of gouge, so that each event has a surface energy of $2.0-3.6 \text{ MJ/m}^2$, compared to Chester and Chester's [2004] $0.02 - 0.1 \text{ MJ/m}^2$. Interestingly, Wilson et al. [2004] estimated the surface energy of the M3.7 1997 Bosman earthquake, which ruptured unfaulted quartzitic layers, to be $3-10 \text{ MJ/m}^2$, greater than their surface energy estimate for a San Andreas event. We have included these geologic surface energy values in Figure 9a to help the comparison with our estimates of breakdown work.

The differences observed between the Punchbowl and the Fort Tejon fault segments may be consistent with our observations. First, it is very significant that the surface energy and gouge zone widths of the M 3.7 Bosman earthquake

are larger than those estimated for much larger San Andreas events. This observation is consistent with the idea that most of the gouge zone of faults is produced within the first km of slip [Chester and Chester, 1998] before the development of a thin principal slip surface. The Bosman surface energy is completely inconsistent with the linear $\log(M_0)$ vs. $\log(W_b)$ in our Figure 9a, where we plot breakdown work averaged over the fault. However, the Bosman fracture energies are comparable with our W_b values taken from areas of largest slip, suggesting that some of these high slip areas may be geometric complexities where fresh fracture and large stress drops occur. Second, the spectacular difference in the widths of the damage zones cited for the Punchbowl fault and the San Andreas at Tejon Pass suggests that the Tejon Pass section may be some exhumed geometric complexity or fault step-over zone [J. Chester, personal communication, 2004], where a single principal slip surface has not been formed and where large earthquake ruptures frequently branch into unfractured rock. Four of the earthquakes we have studied, the Morgan Hill, Kobe, Landers, and Imperial Valley earthquakes, ruptured through known geometric complexities, and all four show some zones of large breakdown work (and high slip) very near fault stepovers or fault junctions. The Kobe earthquake (Figure 8a) shows high breakdown work zones adjacent to the stepover from the Nojima to the Suma-Suwayama fault, the Wald and Heaton [1996] model of the Landers earthquake shows high breakdown work at the stepovers from the Camp Rock/Emerson to the Homestead Valley and from the Homestead Valley to the Johnson Valley faults (Figure 8a), although the Hernandez et al. [1999] model does not show this, and the Imperial Valley earthquake shows a large peak of breakdown work very near the junction of the Brawley and Imperial faults (Figure 8a). The large breakdown work zone in the Morgan Hill earthquake occurs at a geometric complexity in the Calaveras fault (Beroza and Spudich, 1988). The above picture is counter-intuitive, in that fault bends and junctions might be expected to act as low-slip barriers to rupture. However, fresh fracture and rupture on fault splays must

occasionally occur at such places [Andrews, 1989], and perhaps we see this in some of our rupture models.

6.9 Conclusive remarks

We have defined a quantity called breakdown work, which is the work per unit fault area expended in kinematic slip models during the weakening phase of the slip. We have also defined restrengthening work similarly, and excess work as the sum of the two. We have specified a way to calculate them when slip and traction rotate with time in the kinematic models. In this calculational method we have assumed that the initial traction is large and is directed at each point on the fault in the direction of the final slip. We have calculated the breakdown work and restrengthening work for kinematic slip models for earthquakes whose magnitudes range between 5.6 (October 14th Colfiorito earthquake) to 7.2 (for the 1992 Landers earthquake). Estimates of breakdown work are affected by the frequency band of the kinematic model. Spudich and Guatteri [2004] found that low-pass filtering slip models caused breakdown work to increase, whereas in our models it decreases. Breakdown work density and its integral over the fault, breakdown energy, scale with seismic moment according to a power law (with exponent 0.57 and 1.18, respectively). The spatial distribution of breakdown work in a single earthquake is strongly correlated with the slip distribution. Our observed breakdown work scaling agrees very well with that predicted by Rice et al. [2004] for a slip pulse model and does not agree with a crack-like model. We compared our breakdown works with geologically estimated fracture energies from the Bosman fault in South Africa and the San Andreas fault at Tejon Pass [Wilson et al., 2004], and with the Punchbowl fault [Chester and Chester, 2004]. The Bosman fault earthquake ruptured intact quartzitic rocks, and the surface energy for this M 3.7 event was comparable to the breakdown work we estimate for M6-7 events. Fracture energy estimated for the Tejon Pass portion of the San Andreas is also comparable to our M 6-7 breakdown works. However, surface energy estimated for the Punchbowl fault, where there is a very narrow principal slip

surface, are much smaller than our observed breakdown works. Our observed breakdown work for the Landers, Kobe, Morgan Hill, and Imperial Valley earthquakes is high at places on the faults that are geometrically complicated. These observations lead us to speculate that the Tejon Pass section of the San Andreas represents an exhumed fault stepover or other geometric complexity, and that rupture through this stepover was frequently accommodated by fresh fracture, producing the high observed geologic surface energy, comparable to the high breakdown work we observe at geometric complexities in the Landers, Kobe, and Imperial Valley earthquakes. In such places most or all of our observed breakdown work might be expended in creating geologic fractures, rather than in heat. In contrast, other regions of high breakdown work that we observe might be occurring on narrow principal fault surfaces, like that of the Punchbowl fault. In such places, where Chester and Chester [2004] measure low fracture energies, most of our observed breakdown work might be going into heat with only a small part going into producing fresh fracture [Chester and Chester, 2004].

Conclusions

Earthquakes are certainly one of the most important manifestations of faulting and the understanding of dynamic fault weakening during the nucleation and the propagation of a seismic rupture is a major task for seismologists. A main result that is relevant to characterize dynamic fault weakening during an earthquake is the traction evolution.

The slip on a fault is associated with a drop in shear stress and the evolution of rupture depends on the initial conditions and on the constitutive law.

Kinematic descriptions of the earthquake source specify the slip as a function of space and time without explicit consideration on the physical model of the rupture process. However, they can be helpful to constrain the stress histories and the dynamic parameters (as we have seen in Chapters 5 and 6).

The dynamic description of earthquake rupture assumes that traction evolution on the fault is governed by frictional processes. These latter can be described through constitutive laws that give us not only the critical conditions to initiate a dynamic instability but even the temporal evolution of stress release. By means of constitutive laws it is possible to depict the whole duration of co-seismic phase: from the nucleation phase to the arrest.

In the dynamic modeling, the fault weakening during a rupture propagation is represented by the traction drop associated with slip increase, resulting on the well known slip-weakening model. Different physical processes can yield a traction evolution consistent with this behavior.

In this thesis we see that the rate and state constitutive laws can be used to model the weakening mechanisms as well as the healing phase. We confirm the findings of previous studies that slip weakening is a characteristic behavior even of rate and state friction. Such a traction variation with slip must be common to any constitutive relation proposed to model rupture propagation. Our simulations show that the slip acceleration and the slip weakening behavior are controlled and driven by the state variable evolution.

We show that the classic slowness or slip laws do not yield fast restrengthening or self-healing, although they appropriately describe rupture initiation, propagation and the long-term restrengthening during the interseismic period. Self-healing rupture mode, yielding to short slip durations, is obtained for homogeneous faults by modifying the evolution law introducing a fast restrengthening of dynamic traction immediately after the weakening phase. However, these constitutive laws have never been tested to simulate the whole seismic cycle or the quasi-static earthquake nucleation. Therefore, we point out that the modeling of self-healing rupture mode, which implies a fast restrengthening, might not be appropriate to simulate the fault behavior during the interseismic period or the quasi-static nucleation. This raises the question on the reliability of these analytical modifications of lab-derived constitutive laws to explain short slip durations, even when motivated by physical arguments.

Certainly, the ambitious perspective of dynamic modeling investigations is the simulation of fault behavior during the entire seismic cycle. This requires us to describe the earthquake nucleation, the dynamic rupture propagation and arrest during individual earthquakes (accurately describing the breakdown processes and the healing of slip) and the long term restrengthening during the interseismic period, which yields to repeated dynamic failure episodes on the same fault. To this goal, it is important to look for a unified constitutive law describing most of these features.

Furthermore, we see that healing can be modelled through the heterogeneities of constitutive parameters (i.e., heterogeneous reology). Laboratory experiments show that the fault plane can be described with weakening regime ($a-b < 0$), i.e. potentially unstable, or with strengthening regime ($a-b > 0$), i.e. inherently stable. We verify that frictional heterogeneities can explain the observed complexity of slip distribution. Our simulations provide a picture of the complex interactions between fault patches having different frictional properties and illustrate how the traction and slip velocity evolutions are modified during propagation on heterogeneous faults. A velocity strengthening area can arrest a dynamic rupture and it can be driven to instability if suddenly loaded by the dynamic rupture front. Therefore, although appropriate

modification of the evolution law allows the modeling of self-healing ruptures and the propagation of slip velocity pulses, the heterogeneities of constitutive parameters and fault complexities can explain short slip durations without modifying the constitutive model. It has to be kept in mind that different competing natural mechanisms contribute to the understanding of earthquake mechanics. Actually, the healing phase could be the result of other mechanisms not involved in the constitutive description.

The use of constitutive laws is fundamental to have a complete dynamic description of a seismic event. Anyway, current constitutive laws still not describe all the competing mechanisms that contribute to the mechanics of earthquakes. The understanding of the spatial and temporal scale dependence of relevant processes (including thermal pressurization, gouge formation, local melting, flash heating...) is one of future goals of the dynamic description of seismic source. Despite the existing limitations to assemble and to describe all the competing processes affecting earthquake mechanics, efforts to propose a unified constitutive law are useful to achieve a reliable physical description of the dynamic rupture growth. We believe that rate and state formulation is a suitable tool to this purpose, although further investigations and laboratory experiments are needed to explain the friction behavior at high slip rates or to include the effects of normal stress variations in the constitutive model (see Linker and Dieterich, 1992). This necessarily requires new types of laboratory and natural fault observations, together with theory, for moving the conceptual background beyond what is now available.

Another important question on a fully dynamic modelling concerns the scaling of constitutive parameters. In particular, there are controversial discussions on the estimate of critical slip weakening distance. The latter is an important dynamic parameter because it affects the energy balance. The D_c values proposed in the recent literature span from microns to several meters. Several attempts have been made to infer the slip-weakening distance D_c for actual earthquakes. One of this consists to infer D_c from the computation of slip at the time of peak slip velocity (D_c'). We verify this method with a fully

Conclusions

dynamic models adopting the slip weakening law as well as the rate and state laws. We demonstrate that the adopted constitutive law and the constitutive parameters control the slip acceleration as well as the timing and the amplitude of peak slip velocity. The difference we find between D_c values and the inferred D'_c range between few percent up to 50%. The estimate of D'_c might be useful if we accept the idea that D_c can range over several order of magnitudes. These uncertainties have motivate the second part of our thesis.

In the second part of this thesis, we focus our attention on the estimate of actual values of dynamic parameters. Critical slip weakening distance, dynamic stress drop, fracture energy are some of the most significant parameters that play a critical role on the rupture process and hence on the strong ground motions. The rupture complexity inferred from the kinematic slip distributions has significant implications for the dynamics of seismic source. Studying the source properties of well documented past earthquakes offers the possibility to gain insight into the physics of the rupture process.

The reconstruction of traction evolution from kinematic rupture models is being common to supply with constraints for dynamic description. However we verify that source time functions, adopted in kinematic source models, affect the inferred dynamic parameters. We present the results of a sensitivity test using kinematic models whose difference consists only on the assumed slip-velocity time function: the corresponding dynamic models have different weakening behaviors even if the synthetic waveforms of the kinematic models are very similar in the band pass frequency between 0.1Hz and 1.5 Hz (typically used in kinematic strong motion inversion). Following this procedure we see that critical slip weakening distance ranges between 30% and 80% of the total slip. Our simulations show an evident correlation between the spatial distribution of D_c and the final slip over the fault plane, in agreement with previous studies. Moreover, the ratio between D_c and final slip value is nearly constant and controlled by the adopted source time function. These results raise doubts on the correlation between D_c and final slip values. Actually, further investigations are

needed to interpret the dependence of dynamic parameters on the kinematic assumptions.

These reasons have incited us to study more deeply the assumed source time function especially because not all source time functions adopted in kinematic modelling have physical meaning. That is, the estimates of dynamic parameters could be biased and not true. Besides, the variations in the slip-velocity function arising from rupture dynamics effects underline the importance of understanding the slip velocity behavior even for predicting strong ground motion.

We propose an innovative and original analytical expression of a source time function compatible with dynamic rupture simulations. This new slip velocity function, called new *Yoffe*, is described by three parameters: the final slip, D_{\max} , the slip duration (i.e. rise time), τ_R , and the duration of the positive slip acceleration (i.e. time to peak slip velocity), T_{acc} . This slip velocity function is very useful in kinematic modeling of ground motion and allows an easy implementation in numerical codes. By analyzing the results of our simulations we obtained scaling relations between V_{peak} and relevant dynamic parameters as well as the scaling between D_c and D_{\max} at each point on the fault. Our results are of relevance to both kinematic modeling of ground motion time histories and the parameterization of kinematic slip models. The usage of this slip function guarantees the estimation of the temporal evolution of dynamic parameters. The obtained scaling relations are consistent with those proposed by Ohnaka and Yamashita (1989) from laboratory experiments. This shows that the proposed source time function is suitable to represent the dynamic rupture propagation with finite slip-weakening distances.

The spatial variability in the slip velocity function is not usually considered in kinematic source characterizations, however, it is a reasonable and expected property of a complex rupture model. The parameterization we propose for the new source time function is very feasible and allows heterogeneities on kinematic models.

Conclusions

Finally we compute dynamic parameters from the kinematic models of recent earthquakes (available in the literature). For some of the earthquakes, multiple source models exist possibly obtained using different inversion strategies. The variability in these single-event source models provides a means to assess the unknown uncertainties of the imaged slip distributions. The kinematic models we use have been retrieved through different inversion procedures: single window as well as multi window approaches, fixed as well as inverted rise time; strong motion data as well as combined strong motion, GPS and teleseismic data. In particular we focus our attention on estimate of fracture energy. The latter is a fundamental parameter for describing earthquakes in terms of the physics and provides important insight into the rupture process.

To avoid any misleading concept, we define a new quantity, breakdown work W_b , still representing an energy density.

We show that breakdown work depends on the square of slip. The spatial distribution of breakdown work in a single earthquake is strongly correlated with the slip distribution. Breakdown work density and its integral over the fault, breakdown energy, scale with seismic moment according to a power law (with exponent 0.57 and 1.18, respectively). Our estimates of breakdown work range between $4 \cdot 10^5$ and $2 \cdot 10^7$ J/m² for earthquakes having moment magnitudes between 5.6 and 7.2. We compare our inferred values with geologic surface energies. This comparison might suggest the existence of large slip areas of fresh fracture during earthquake ruptures.

We have estimated fracture energies and traction evolutions for recent earthquakes. One of the possible interpretation of these results can be inferred by means of rate and state constitutive laws. These laws describe the dynamic slip episodes through the properties of the contact surface. However, there is now the awareness that frictional heating, thermal pressurization of pore fluids and mechanical lubrication can contribute to explain dynamic fault weakening and control the fault friction at high slip rates.

The definition of fault zone model and the understanding of the dominant physical processes are extremely important tasks of present and future scientific research.

Appendix

We compute the convolution of the original *Yoffe* function $Y(t, \tau_R)$ defined in Equation (5.4) with the triangular function $W(t, \tau_S)$ defined in Equation (5.5). The new analytical STF stated in Equation (5.6) can be expressed as

$$S(t) = D_{max} \int_{-\infty}^{+\infty} W(t-T; \tau_S) Y(T; \tau_R) dT = D_{max} (S1(t) + S2(t)) \quad (A1)$$

where

$$S1(t) = \int_{-\infty}^{+\infty} H(t-T) H(\tau_S - t + T) \frac{t-T}{\tau_S^2} \times \left[H(T) H(\tau_R - T) \frac{2}{\pi \tau_R} \sqrt{\frac{\tau_R - T}{T}} \right] dT \quad (A2)$$

$$S2(t) = \int_{-\infty}^{+\infty} H(t-T-\tau_S) H(2\tau_S - t + T) \frac{2\tau_S - t + T}{\tau_S^2} \times \left[H(T) H(\tau_R - T) \frac{2}{\pi \tau_R} \sqrt{\frac{\tau_R - T}{T}} \right] dT \quad (A3)$$

There are some different intervals to define the solution. The *Yoffe* function $Y(t)$ is defined in $0 < t < \tau_R$. The triangular function ($W(t)$) has the following two ranges:

1. $t - 2\tau_S < T < t - \tau_S$
2. $t - \tau_S < T < t$

These ranges are represented by the Heaviside functions. Then we compute the integration taking into account the above ranges. When we substitute the integration intervals we have also to consider the *Yoffe* function ranges ($0 < t < \tau_R$). We use the known integral solution:

$$\int x \sqrt{\frac{x}{a-x}} dx = -\frac{2x+3a}{4} \sqrt{ax-x^2} + \arctan \sqrt{\frac{x}{a-x}} \quad (A4)$$

$$\int \sqrt{\frac{x+b}{x+a}} dx = \sqrt{-(x+a)(x+b)} + (a-b) \arcsin \sqrt{\frac{x+a}{a-b}} \quad (a > b) \quad (A5)$$

For the first range ($t - 2\tau_S < T < t - \tau_S$),

$$S1 = \int_n^m \frac{1}{\tau_S^2} (2\tau_S - t + T) \frac{2}{\pi \tau_R} \sqrt{\frac{\tau_R - T}{T}} dT$$

$$\begin{aligned}
&= \int_n^m \frac{1}{\tau_S^2} (2\tau_S - t) \frac{2}{\pi\tau_R} \sqrt{\frac{\tau_R - T}{T}} dT + \int_n^m \frac{1}{\tau_S^2} T \frac{2}{\pi\tau_R} \sqrt{\frac{\tau_R - T}{T}} dT \\
&= K(2\tau_S - t) \left[\sqrt{(\tau_R - T)T} + \tau_R \arcsin \sqrt{\frac{T}{\tau_R}} \right]_n^m \\
&\quad + K \left[\frac{(2T + 3\tau_R)}{4} \sqrt{(\tau_R - T)T} - \frac{3\tau_R^2}{4} \arctan \sqrt{\frac{T}{\tau_R - T}} \right]_{\tau_R - m}^{\tau_R - n} \tag{A6}
\end{aligned}$$

where

$$K = \frac{2}{\pi\tau_R\tau_S^2} \tag{A7}$$

and

$$m = \begin{cases} t - \tau_S & \text{for } \tau_S < t < \tau_R + \tau_S \\ \tau_R & \text{for } \tau_R + \tau_S < t < 2\tau_S \end{cases} \tag{A8}$$

$$n = \begin{cases} 0 & \text{for } t < 2\tau_S \\ t - 2\tau_S & \text{for } 2\tau_S < t < \tau_R + 2\tau_S \end{cases} \tag{A9}$$

For the second range ($t - \tau_S < T < t$),

$$\begin{aligned}
S2 &= \int_{n'}^{m'} \frac{1}{\tau_S^2} (t - T) \frac{2}{\pi\tau_R} \sqrt{\frac{\tau_R - T}{T}} dT \\
&= Kt \left[\sqrt{(\tau_R - T)T} + \tau_R \arcsin \sqrt{\frac{T}{\tau_R}} \right]_{n'}^{m'} \\
&\quad - K \left[\frac{(2T + 3\tau_R)}{4} \sqrt{(\tau_R - T)T} - \frac{3\tau_R^2}{4} \arctan \sqrt{\frac{T}{\tau_R - T}} \right]_{\tau_R - m'}^{\tau_R - n'} \tag{A10}
\end{aligned}$$

where

$$m' = \begin{cases} t & \text{for } 0 < t < \tau_R \\ \tau_R & \text{for } \tau_R < t < \tau_R + \tau_S \end{cases} \tag{A11}$$

$$n' = \begin{cases} 0 & \text{for } t < \tau_S \\ t - \tau_S & \text{for } \tau_S < t < \tau_R + \tau_S \end{cases} \tag{A12}$$

Therefore, the final integrations are as follows: If $\tau_R > 2\tau_S$,

$$S(t) = K \begin{cases} 0 & \text{for } t < 0 \\ (C1 + C2) & \text{for } 0 < t < \tau_S \\ (C1 - C2 + C3) & \text{for } \tau_S < t < 2\tau_S \\ (C1 + C3 + C4) & \text{for } 2\tau_S < t < \tau_R \\ (C5 + C3 + C4) & \text{for } \tau_R < t < \tau_R + \tau_S \\ (C4 + C6) & \text{for } \tau_R + \tau_S < t < \tau_R + 2\tau_S \\ 0 & \text{for } \tau_R + 2\tau_S < t \end{cases} \quad (\text{A13})$$

And if $\tau_S < \tau_R < 2\tau_S$,

$$S(t) = K \begin{cases} 0 & \text{for } t < 0 \\ (C1 + C2) & \text{for } 0 < t < \tau_S \\ (C1 - C2 + C3) & \text{for } \tau_S < t < \tau_R \\ (C5 + C3 - C2) & \text{for } \tau_R < t < 2\tau_S \\ (C5 + C3 + C4) & \text{for } 2\tau_S < t < \tau_R + \tau_S \\ (C4 + C6) & \text{for } \tau_R + \tau_S < t < \tau_R + 2\tau_S \\ 0 & \text{for } \tau_R + 2\tau_S < t \end{cases} \quad (\text{A14})$$

where

$$C1 = \left(\frac{1}{2}t + \frac{1}{4}\tau_R\right)\sqrt{t(\tau_R - t)} + (t\tau_R - \tau_R^2)\arcsin\sqrt{\frac{t}{\tau_R}} - \frac{3}{4}\tau_R^2\arctan\sqrt{\frac{\tau_R - t}{t}} \quad (\text{A15})$$

$$C2 = \frac{3}{8}\pi\tau_R^2 \quad (\text{A16})$$

$$C3 = \left(\tau_S - t - \frac{1}{2}\tau_R\right)\sqrt{(t - \tau_S)(\tau_R - t + \tau_S)} + \tau_R(2\tau_R - 2t + 2\tau_S)\arcsin\sqrt{\frac{t - \tau_S}{\tau_R}} + \frac{3}{2}\tau_R^2\arctan\sqrt{\frac{\tau_R - t + \tau_S}{t - \tau_S}} \quad (\text{A17})$$

$$C4 = \left(-\tau_S + \frac{1}{2}t + \frac{1}{4}\tau_R\right)\sqrt{(t - 2\tau_S)(\tau_R - t + 2\tau_S)} + \tau_R(-\tau_R + t - 2\tau_S)\arcsin\sqrt{\frac{t - 2\tau_S}{\tau_R}} - \frac{3}{4}\tau_R^2\arctan\sqrt{\frac{\tau_R - t + 2\tau_S}{t - 2\tau_S}} \quad (\text{A18})$$

$$C5 = \frac{\pi}{2}\tau_R(t - \tau_R) \quad (\text{A19})$$

$$C6 = \frac{\pi}{2}\tau_R(2\tau_S - t + \tau_R) \quad (\text{A20})$$

According to these equations the proposed source time functions $S(t)$ is parameterized through the following parameters: D_{max} , τ_S and τ_R . Using Equation (5.9) we can easily substitute τ_S with T_{acc} in the proposed analytical relations. Moreover, Equation (5.7) relates the duration of the original Yoffe function (τ_R) to the effective duration of the smoothed Yoffe (τ_R^{eff}). These relations define the dependence of the STF on the parameters D_{max} , T_{acc} and τ_R^{eff} , even if the resulting expressions are analytically complicated.

References

Aki, K., and P.G. Richards, 2002, *Quantitative Seismology* (second edition). University Science Books.

Andrews, D. J., 1973, A numerical study of tectonic stress release by underground explosions, *Bull. Seism. Soc. Am.*, 63.

Andrews, D. J., 1976a, Rupture propagation with finite stress in antiplane strain. *J. Geophys. Res.* 81, No. 20, 3575 – 3582.

Andrews, D. J., 1976b, Rupture velocity of plane strain shear cracks. *J. Geophys. Res.* 81, No. 32, 5679 – 5687

Andrews, D. J., 1989, Mechanics of fault junctions, *J. Geophys. Res.*, 94, 9389-9397.

Andrews, D.J., 1999, Test of two methods for faulting in finite-difference calculations, *Seismol. Soc. Am. Bull.*, 89, 4, 931-937.

Andrews, D. J., 2002, A fault constitutive relation accounting for thermal pressurization of pore fluid. *J. Geophys. Res.* 107, (B12) 2363.

Andrews, D. J. 2005, Rupture dynamics with energy loss outside the slip zone, *J. Geophys. Res.*, accepted, doi:10.1029/2004JB003191

Andrews, D. J., Ben-Zion Y., 1997, Wrinkle-like slip pulse on a fault between different materials. *J. Geophys. Res.* 102, No. B1, 553 – 571.

Aochi, H., Fukuyama, E., 2002, Three-dimensional nonplanar simulation of the 1992 Landers earthquake, *J. Geophys. Res.*, 107, (B2),2035, 10.1029/2000JB000061.

Barenblatt, G. I., 1959, The formation of brittle cracks during brittle fracture. General ideas and hypotheses. Axially-symmetric cracks. *Appl. Math. Mech.* 23, 1273 - 1282.

References

Barenblatt G. I., 1959b, Concerning equilibrium crack forming during brittle fracture. The stability of isolated cracks. Relationship with energetic theories, *Appl. Math. Mech.*, 23, 1273–1282

Beeler, N. M., Tullis T. E., Weeks J. D., 1994, The roles of time and displacement in the evolution effect in rock friction. *Geophys. Res. Lett.* 21, No. 18, 1987 -1990

Beeler, N. M., Tullis T. E., 1996, Self-healing slip pulses in dynamic rupture models due to velocity-dependent strength. *Bull. Seism. Soc. Am.* 86, No. 4, 1130 – 1148

Beresnev I.A., 2003, Uncertainties in finite-fault slip inversions: To what extent to believe? (A critical review), *Bull. Seismol. Soc. Am.*, 93,2445-2458.

Beroza, G., Mikumo, T., 1996, Short slip duration in dynamic rupture in the presence of heterogeneous fault properties, *J. Geophys. Res.*, 101, 22449-22460

Beroza, G.C., and P. Spudich, 1988, Linearized inversion for fault rupture behavior; application to the 1984 Morgan Hill, California, earthquake, *J. of Geophys. Res.*, B, Solid Earth and Planets, 93 (6), 6275-6296.

Bizzarri, A. and Cocco M., 2003, Slip-weakening behavior during the propagation of dynamic ruptures obeying rate- and state- dependent friction laws, *J. Geophys. Res.*, B8, No. 2373.

Bizzarri, A., M. Cocco, D. J. Andrews, and E. Boschi, 2001, Solving the dynamic rupture problem with different approaches and constitutive laws, *Geophys. J. Int.*, 144, 656-678.

Blanpied M. L., Lockner D. A., Byerlee J. D. 1991, Fault stability inferred from granite sliding experiments at hydrothermal conditions, *Geophys. Res. Lett.*, 18, 609–612

Blanpied M. L., Lockner D. A., Byerlee J. D. 1995, Frictional slip of granite at hydrothermal conditions, *J. Geophys. Res.*, 100, No. B7, 13045–13064

Boatwright, J., Cocco M., 1996, Frictional constraints on crustal faulting. *J. Geophys. Res.* 101, No. B6, 13895 – 13909

References

Bouchon, M., 1997, The state of stress on some faults of the San Andreas system as inferred from near-field strong motion data, *J. Geophys. Res.*, 102, B6, 11731-1744.

Bouchon, M., Campillo M and Cotton F., 1998, Stress field associated with the rupture of the 1992 Landers, California, earthquake and its implications concerning the fault strength at the onset of the earthquake, *J. Geophys. Res.*, 103, B9, 21091-21097.

Bouchon, M., N. Toksoz, H. Karabulut, M.-P. Bouin, M. Dietrich, M. Akter, M. Edie, 2000, Seismic imaging of the 1999 Izumit (Turkey) rupture inferred from the near-fault recordings, *Geophys. Res. Lett.*, 27, 3013-3016.

Broberg, K., 1978, On transient sliding motion, *Geophys. J. Roy. astr. Soc.*, 52, 397-432.

Broberg, K., 1999, *Cracks and Fracture*, Academic Press, New York.

Brodsky, E. E., Kanamori, H., 2001, Elastohydrodynamic lubrication of faults. *J. Geophys. Res.*, 106, 16357-16374.

Brune J. N., 1970, Tectonic stress and the spectra of seismic shear waves from earthquakes, *J. Geophys. Res.*, 75, No. 26, 4997–5009

Chester, F., and Chester, J., 1998, Ultracataclasite structure and friction processes of the Punchbowl fault, San Andreas system, California, *Tectonophys.*, 295, 199-221.

Chester, J. S., and F. M. Chester, 2004, Fracture surface energy of mature fault zones from structural observations of the Punchbowl fault, California Annual Meeting of the Southern California Earthquake Center, Abstracts with Program, Palm Springs, CA, Sept. 20-22.

Cocco, M., and A. Bizzarri, 2002, On the slip-weakening behavior of rate- and state dependent constitutive laws, *Geophys. Res. Lett.*, 29, 11, doi:10.1029/2001GL013999.

Cocco M., Bizzarri A., Tinti E., 2004, Physical interpretation of the breakdown process using a rate- and state-dependent friction law, *Tectonophys. “ Physics of Active Faults “*, 378, 241–262

References

- Cochard, A., R. Madariaga, 1994, Dynamic faulting under rate-dependent friction, *Pure Appl. Geophys.*, 142, 419-445.
- Cochard, A., Madariaga, R., 1996, Complexity of seismicity due to highly rate-dependent friction. *J. Geophys. Res.*, 101, 25321-25336.
- Cochard, A., Rice, J. R., 2000, Fault rupture between dissimilar materials: ill-posedness, regularization, and slip pulse response, *J. Geophys. Res.* 105, 891–907.
- Cohee, B. P. and G. C. Beroza, 1994, A comparison of two methods for earthquake source inversion using strong motion seismograms, *Ann. Geophys.*, 37, 1515-1538.
- Cotton, F. and Campillo M., 1995, Frequency domain inversion of strong motions : application to the 1992 Landers earthquake, *J. Geophys. Res.*, 100, 3961-3975.
- Dalguer, L.A., Irikura K., Zhang W., Riera J.D., 2002, Distribution of dynamic and static stress changes during 2000 Tottori (Japan) earthquake: brief interpretation of the earthquake sequences; foreshocks, mainshock and aftershocks, *Geophys. Res. Lett.*, 29, 16, doi:10.1029/2001GL014333.
- Das, S, and K. Aki, 1977, A numerical study of two-dimensional spontaneous rupture propagation, *Geophys. J. Roy. Astr. Soc.*, 50, 643-668.
- Day, S. M., 1982, Three-dimensional finite difference simulation of fault dynamics: Rectangular faults with fixed rupture velocity, *Bull. Seism. Soc. Am.*, 72, 705-727.
- Day, S.M., G. Yu and D.J. Wald, 1998, Dynamic stress changes during earthquake rupture, *Seismol. Soc. Am. Bull.*, 88, 2, 512-522.
- Dieterich, J. H., 1979, Modeling of rock friction - 1. Experimental results and constitutive equations, *J. Geophys. Res.*, 84, 2161-2168.
- Dieterich, J. H., 1986, A model for the nucleation of earthquake slip. *Earthquake Source Mechanics, Geophysical Monograph. 37. Maurice Ewing Series, 6*, edited by S. Das, J. Boatwright and C. H. Scholz. *Am. Geophys. Union. Washington D. C.*, 37 – 47

References

- Dieterich. J. H., 1992, Earthquake nucleation on faults with rate- and state-dependent strength. *Tectonophysics*, 211, 115 – 134
- Dieterich. J. H., 1994, A constitutive law for rate of earthquake production and its application to earthquake clustering, *J. Geoph. Res.*, 99, 2601-2618
- Dieterich. J. H., B. Kilgore, 1994, Direct observations of frictional contacts: new insights for state-dependent properties, *Pure Appl. Geophys.*, 143, 283-302
- Dalguer, L.A., Irikura K., Zhang W., Riera J.D., 2002, Distribution of dynamic and static stress changes during 2000 Tottori (Japan) earthquake: brief interpretation of the earthquake sequences; foreshocks, mainshock and aftershocks, *Geophys. Res. Lett.*, 29, 16, doi:10.1029/2001GL014333.
- Favreau, P. and Archuleta R.J., 2003, Direct seismic energy modeling and application to the 1979 Imperial Valley earthquake, *Geophys. Res. Lett.*, 30, 5, doi:10.1029/2002GL015968.
- Fialko Y. A., 2004, Temperature fields generated by the elastodynamic propagation of shear cracks in the Earth, *J. Geophys. Res.*, 109, No. B01303, doi: 10.1029 / 2003JB002497, 1–14
- Freund, L. B., 1979, The mechanics of dynamic shear crack propagation, *J. Geophys. Res.*, 84, 2199-2209.
- Fukuyama, E., Ellsworth W.L, Waldhauser F. and Kubo A., 2003, Detailed fault structure of the 2000 Western Tottori, Japan, earthquake sequence, *Bull. Seismol Soc. Am.*, 93(4), 1468-1478.
- Fukuyama, E. and K. Irikura, 1986, Rupture process of the 1983 Japan Sea (Akita-Oki) earthquake using a waveform inversion method, *Bull. Seismol. Soc. Am.*, 76,1623-1649.
- Fukuyama, E., and R. Madariaga, 1998, Rupture dynamics of a planar fault in a 3-D elastic medium: rate- and slip-weakening friction, *Bull. Seism. Soc. Am.*, 88, 1-17.
- Fukuyama, E., T. Mikumo, and K. B. Olsen, 2003, Estimation of the critical slip-weakening distance: theoretical background, *Bull. Seism. Soc. Am.*, 93, 1835-1840.

References

Fukuyama, E. and T. Mikumo, 1993, Dynamic rupture analysis: Inversion for the source process of the 1990 Izu-Oshima, Japan, earthquake (M=6.5), *J. Geophys. Res.*, 98, 6529-6542.

Gu, J. C., 1984, Frictional resistance to accelerating slip, *Pure and Appl. Geophys*, 122, 662-679

Gu J. C., Rice J. R., Ruina A. L., Tse S. T., 1984, Slip motion and stability of a single degree of freedom elastic system with rate and state dependent friction, *J. Mech. Phys. Solids*, 32, No. 3, 167-196

Gu, Y., T.F. Wong, 1991, Effects of loading velocity, stiffness, and inertia on the dynamics of a single degree of freedom spring slider system, *J. Geoph. Res.*, 96, 21677 - 21691

Guatteri, M. and Spudich P., 2000, What can strong-motion data tell us about slip-weakening fault-friction laws?, *Seismol. Soc. Am. Bull.*, 90 (1), 98-116.

Guatteri, M., Spudich P. and Beroza G., 2001, Inferring rate and state friction parameters from a rupture model of the 1995 Hygo-ken Nanbu (Kobe) Japan earthquake, *J. Geophys. Res.*, 106, B11, 26511-26521.

Guatteri, M., Mai P.M., Beroza G.C., Boatwright J. 2003, Strong ground motion prediction from stochastic-dynamic source models, *Bull. Seism. Soc. Am.*, 93, No. 1, 301-313.

Hartzell S. H. and Heaton T. H., 1983, Inversion of strong ground motion and teleseismic waveform data for the fault rupture history of the 1979 Imperial Valley, California, earthquake, *Seismol. Soc. Am. Bull.*, 73, 1553-1583.

Heaton, T. H., 1990, Evidence for and implications of self-healing pulses of slip in earthquake rupture, *Phys. Earth. Planet. Inter.*, 64, 1-20.

Hernandez, B., Cotton F., Campillo M., Courboulex F., Cocco M. And Stramondo S., 2005, Rupture history of the 1997 Umbria Marche (Central Italy) earthquakes from the inversion of GPS, SAR and strong motion data, *Annals of Geophys.*, in press.

Hernandez, B., F. Cotton, and M. Campillo, 1999, Contribution of radar interferometry to a two-step inversion of the kinematic process of the 1992 Landers earthquake, *J. Geophys. Res.*, 104 (B6), 13083-13099.

References

Hisada, Y., 2000, A theoretical omega-square model considering the spatial variation on slip and rupture velocity, *Bull. Seismol. Soc. Am.*, 90, 387-400.

Hisada, Y., 2001, A theoretical omega-square model considering the spatial variation on slip and rupture velocity. II. Case for a two-dimensional source model, *Bull. Seismol. Soc. Am.*, 91, 651-666.

Husseini M.I., B.J. Dushan, M.J. Randall and L.B. Freund, 1975, On the fracture energy, *Geophys. J. R. astr. Soc.* (43), 367-385.

Ida, Y., 1972, Cohesive force across the tip of a longitudinal-shear crack and Griffith's specific surface energy. *J. Geophys. Res.* 77, 3796-3805.

Ide, S. and Takeo M., 1997, Determination of constitutive relations of fault slip based on seismic wave analysis, *J. Geophys. Res.*, 102, B12, 27379-27391.

Ide, S., 2003, On fracture surface energy of natural earthquakes from viewpoint of seismic observations, *Bulletin of Earthquake Research Institute*, 78, 1-120.

Iwata, T. and Sekiguchi H., 2001, Inferences of earthquake rupture process from strong-motion records, presented at the Symposium from Strong-Motion Network.

Kaverina, A., D. Dreger and E. Price, 2002, The combined inversion of seismic and geodetic data for the source process of the 16 October 1999 Mw 7.1 Hector Mine, California, earthquake, *Bull. Seismol. Soc. Am.*, 92, 1266-1280.

Kostrov, B. V., 1964, Self-similar problems of propagation of shear cracks, *J. Appl. Math. Mech.*, 28, 1077-1087.

Kostrov, B.V., and S. Das, 1988, *Principles of Earthquake source mechanics*, Cambridge University Press.

Lapusta, N., Rice, J.R., 2003, Nucleation and early seismic propagation of small and large events in a crustal earthquake model. *J. Geophys. Res.* 108 (B4), 2205. (doi:10.1029/2001JB000793)

Lapusta N., Rice J. R., Ben – Zion Y., Zheng G., 2000, Elastodynamic analysis for slow tectonic loading with spontaneous rupture episodes on faults with rate- and state-dependent friction, *J. Geophys. Res.*, 105, No. B10, 23765–23789

References

Lavallée, D., and R.J. Archuleta, 2003, Stochastic modeling of slip spatial complexities for the 1979 Imperial Valley, California, earthquake, *Geophys. Res. Lett.*, 30,5, doi:10.1029/2002GL015839.

Linker, M.F., Dieterich, J.H., 1992, Effects of variable normal stress on rock friction: observations and constitutive equations. *J. Geophys. Res.*, 97, 4923-4940.

Liu, P. and R.J. Archuleta, 2004, A new nonlinear finite fault inversion with three dimensional Green's functions: Application to the 1989 Loma Prieta, California, earthquake, *J. Geophys. Res.*, 109, 2318, doi:10.1029/2003JB002625.

Mai, P.M. and Beroza G.C., 2002, A spatial random field model to characterize complexity in earthquake slip, *J. Geophys. Res.*, 107, B11, 2308, doi:10.1029/2001JB000588.

Mair, K., Marone C. J., 1999, Friction of simulated fault gauge for a wide range of velocities and normal stresses. *J. Geophys. Res.*, 104, 28899 – 28914

Marone, C. J., 1998, Laboratory-derived friction laws and their application to seismic faulting. *Annu. Rev. Earth Planet Sci.* 26, 643 – 696

Marone C., Scholz C. H., Bilham R., 1991, On the mechanics of earthquake afterslip, *J. Geophys. Res.*, 96, No. B5, 8441–8452

Marone, C. J., Kilgore B., 1993, Scaling of the critical slip distance for seismic faulting with shear strain in fault zones. *Nature.* 362, 618 – 621

Mikumo, T. and Miyatake T., 1995, Heterogeneous distribution of dynamic stress drop and relative fault strength recovered from the results of wave-form inversion – the 1984 Morgan-Hill, California earthquake, *Seismol. Soc. Am. Bull.*, 85 (1), 178-193.

Mikumo, T., Olsen K.B., Fukuyama E. and Yagi Y., 2003, Stress-breakdown time and slip-weakening distance inferred from slip-velocity functions on earthquake faults, *Seismol. Soc. Am. Bull.*, 93, 1, 264-282.

Nakamura, H., and T. Miyatake, 2000, An approximate expression of slip velocity time functions for simulation of near-eld strong ground motion, *Zishin(J. Seism. Soc. Jpn.)*, 53, 1-9 (in Japanese with English abstract).

References

Nakatani, M., 2001, Conceptual and physical clarification of rate and state friction: frictional sliding as a thermally activated rheology, *J. Geophys. Res.*, 106, B7, 13347 – 13380

Nielsen, S., Carlson, J. M., 2000, Rupture pulse characterization: self-healing, self-similar, expanding solutions in a continuum model of fault dynamics, *Bull. Seism. Soc. Am.*, 90, 1480-1497.

Nielsen, S., Carlson, J. M., Olsen, K. B., 2000, Influence of friction and fault geometry on earthquake rupture, *J. Geophys. Res.*, 105, 6069 – 6088.

Nielsen, S., and R. Madariaga, 2003, On the self-healing fracture mode, *Seismol. Soc. Am. Bull.*, 93 (6), 2375-2388.

Olgaard, D.L. and Brace, W.F., 1983, The microstructure of gouge from a mining-induced seismic shear zone, *Int. J. Rock Mech. Min. Sci. Geomech. Abstr.* 20, 11-10.

Ohnaka, M., 2003, constitutive scaling law and a unified comprehension for frictional slip failure, shear fracture of intact rock, and earthquake rupture, *J. Geophys. Res.*, 108, 2080, doi:10.1029/2002JB000123.

Ohnaka, M., Y. Kuwahara, and K. Yamamoto, 1987, Constitutive relations between dynamic physical parameters near a tip of the propagation slip zone during stick-slip shear failure, *Tectonophysics*, 144, 109-125.

Ohnaka, M. and Yamashita T., 1989, A cohesive zone model for dynamic shear faulting based on experimentally inferred constitutive relation and strong motion source parameters, *J. Geophys. Res.*, 94, 4089-4104.

Ohnaka, M., 1996, Nonuniformity of the constitutive law parameters for shear rupture and quasi static nucleation to dynamic rupture: a physical model of earthquake generation processes. *Proc. Natl. Acad. Sci. USA.* 93, 3795 – 3802

Ohnaka, M., Shen L. F., 1999, Scaling of the shear rupture process from nucleation to dynamic propagation: implications of geometric irregularity of the rupturing surfaces. *J. Geophys. Res.* 104, 817 – 844

Okubo, P. G., 1989, Dynamic rupture modeling with laboratory-derived constitutive relations. *J. Geophys. Res.* 94, No. B9, 12321 – 12335

References

Okubo, P. G., and J. H. Dieterich, 1984, Effects of physical fault properties on frictional instabilities produced on simulated faults, *J. Geophys. Res.*, 89, 5817-5827.

Olsen, K. B., R. Madariaga, and R. J. Archuleta, 1987, Three-dimensional dynamic simulation of the 1992 Landers earthquake, *Science*, 278 (5339), 834-838.

Palmer, A. C., Rice J. R., 1973, The growth of slip surfaces in the progressive failure of over- consolidated clay. *Proc. R. Soc. London Ser. A* 332, 527 – 548

Perrin, G., Rice, J. R., Zheng, G., 1995, Self-healing slip pulse on a frictional surface, *J. Mech. Phys. Solids*, 43, 1461-1495.

Peyrat, S., Olsen K and Madariaga R., 2001, Dynamic modeling of the Landers earthquake, *J. Geophys. Res.*, 106, B11, 26467-26482.

Piatanesi, A., E. Tinti, M. Cocco and E. Fukuyama, 2004, The dependence of traction evolution on the earthquake source time function adopted in kinematic rupture models, *Geophys. Res. Lett.*, 31, doi:10.1029/2003GL019225.

Pulido, N and Irikura K., 2000, Estimation of dynamic rupture parameters from the radiated seismic energy and apparent stress, *Geophys. Res. Lett.*, 27, 23, 3945-3948.

Quin, H., 1990, Dynamic stress drop and rupture dynamics of the October 15, 1979 Imperial Valley, California, earthquake, *Tectonophys.*, 175, 93-117.

Rice J. R., 1993, Spatio-temporal complexity of slip on a fault, *J. Geophys. Res.*, 98, 9885–9907.

Rice, J.R., and M., Cocco, 2005, Seismic fault rheology and earthquake dynamics, Dahlem Workshop on *The Dynamics of Fault Zones*.

Rice, J.R., C.G. Sammis and R. Parsons, 2004, Off-fault secondary failure induced by a dynamic slip-pulse, , submitted to *Seismol. Soc. Am. Bull.*

Roy, M., Marone C. J., 1996, Earthquake nucleation on model faults with rate- and state-dependent friction: effects of inertia. *J. Geoph. Res.* 101, 13919 – 13932

References

Ruina, A. L., 1980, Friction laws and instabilities: a quasistatic analysis of some dry frictional behavior, Ph. D. Thesis in Engineering at Brown University, Providence, RI

Ruina, A. L., 1983, Slip instability and state variable friction laws, *J. Geophys. Res.* 88, No. B12, 10359 – 10370

Scholz, C. H., 1990, *The mechanics of earthquake and faulting*, Cambridge Univ. Press

Scholz, C. H., 1998, Earthquakes and friction laws, *Nature*, 391, 37 – 42

Segall, P., Rice, J. R., 1995, Dilatancy, compaction and slip instability on a fluid infiltrated fault, *J. Geophys. Res.*, 100, 22155-22171.

Sekiguchi, H. and T. Iwata, 2002, Rupture process of the 1999 Kocaeli, Turkey, earthquake estimated from strong-motion waveforms, *Bull. Seismol. Soc. Am.*, 92, 300-311.

Sibson, R.H., 2003, Thickness of seismic slip zone, *Seismol. Soc. Am. Bull.*, 93,3,1169-1178.

Sleep, N. H., 1997, Application of a unified rate and state friction theory to the mechanics of a fault zones with strain locations, *J. Geophys. Res.*, 102, 2875-2895.

Spudich, P., Guatteri, M., Otsuki, K., and Minagawa, J., 1998, Use of fault striations and dislocation models to infer tectonic shear stress during the 1995 Hyogo-ken Nanbu (Kobe) earthquake, *Seismol. Soc. Am. Bull.*, 88, 413-427.

Spudich, P., and M.Guatteri, 2004, The effect of bandwidth limitations on the inference of earthquake slip-weakening distance from seismograms, *Seismol. Soc. Am. Bull.*, 94 (6), 2028-2036.

Spudich, P. and Xu L., 2002, Software for calculating earthquake ground motions from finite faults in vertically varying media, CD accompanying *International Handbook of Earthq. and Eng. Seismol.*, V.2.

Takeo, M., 1987, An inversion method to analyse the rupture process of earthquakes using near-field seismograms, *Bull. Seismol. Soc. Am.*, 77, 490-513.

References

Tinti, E., A. Bizzarri, A. Piatanesi, and M. Cocco, 2004, Estimates of slip weakening distance for different dynamic rupture models, *Geophys. Res. Lett.*, 31, L02611, doi: 10.1029 / 2003GL018811

Tinti E., A. Bizzarri, and M. Cocco, 2005a, Modeling the dynamic rupture propagation on heterogeneous faults with rate- and state- dependent friction, submitted to *Annals of Geophys.*

Tinti, E., E. Fukuyama, A. Piatanesi and M. Cocco, 2005b, A kinematic source time function compatible with earthquake dynamics, submitted to *Seismol. Soc. Am. Bull.*

Tinti E., P. Spudich, M. Cocco 2005c, Earthquake fracture energy inferred from kinematic rupture models, submitted to *J. Geophys. Res.*

Tse, S. T., and J. R. Rice, 1986, Crustal earthquake instability in relation to the depth variation of frictional slip properties, *J. Geophys. Res.*, 91, No. B9, 9452–9472

Wald, D.J., 1996, Slip history of the 1995 Kobe, Japan, earthquake determined from strong motion, teleseismic, and geodetic data, *Journal of Physics of the Earth*, 44 (5), 489-503.

Wald, D.J., and T.H. Heaton, 1994, Spatial and temporal distribution of slip for the 1992 Landers, California, earthquake, *Seismol. Soc. Am. Bull.*, 84 (3), 668-691.

Wald, D.J., T.H. Heaton, and K.W. Hudnut, 1996, The slip history of the 1994 Northridge, California, earthquake determined from strong-motion, teleseismic, GPS, and leveling data, *Seismol. Soc. Am. Bull.*, 86 (1, Part B Suppl.), 49-70.

Weeks, J., 1993, Constitutive laws for high-velocity frictional sliding and their influence on stress drop during unstable slip, *J. Geophys. Res.*, 98(B10), 17,637-17,648.

Weertman, J., 1980, Unstable slippage across a fault that separates elastic media of different elastic constants. *J. Geoph. Res.*, 85, 1455 – 1461.

Wilson, B., T. Dewers, Z. Reches, and J.N. Brune, 2004, Surface area and surface energy of fault gouge: observations of the San Andreas gouge in Tejon Pass area, California (abstract), SSA meeting in 2004.

References

Yagi, Y. and M. Kikuchi, 2000, Source rupture process of the Kocaeli, Turkey, earthquake of August 17, 1999, obtained by joint inversion of near-field data and teleseismic data, *Geophys. Res. Lett.*, 27, 1969-1972.

Yoffe, E., 1951, The moving Griffith crack, *Phil. Mag.*, 42, 739-750.

Yoshida, S. and K. Koketsu, 1990, Simultaneous inversion of waveform and geodetic data for the rupture process of the 1984 Naganoken-Seibu, Japan, earthquake, *Geophys. J. Int.*, 103, 355-362.

Yoshida, S., K. Koketsu, B. Shibasaki, T. Sagiya, T. Kato, Y. Yoshida, 1996, Joint inversion of near-and far-field waveforms and geodetic data for the rupture process of the 1995 Kobe earthquake, *J. Phys. Earth*, 44, 437-454.

Zhang, W. Iwata T., Irikura K., Sekiguchi H. and Bouchon M., 2003, Heterogeneous distribution of the dynamic source parameters of the 1999 Chi-Chi, Taiwan, earthquake, *J. Geophys. Res.*, 108, B5, 2232, doi:10.1029/2002JB001889.

Zheng, G., Rice, J. R., 1998, Conditions under which velocity-weakening friction allows a self-healing versus a crack like mode of rupture. *Bull. Seism. Soc. Am.*, 88, 1466-1483.

Acknowledgements

I would like to thank all the people have contributed to this work, each one for a specific good reason (that I do not want to write explicitly here).

Thanks to Massimo Cocco, Alessio Piatanesi, Eiichi Fukuyama, Paul Spudich, Andrea Bizzarri, Stefan Nielsen and Maria Elina Belardinelli.

Thanks to Lauro, Betz, Anto, Gaia, Laura, Mimi and Eli.

Other friends have been important even if far from this topic. Thanks to:

my Angel.

My parents, my sisters Alice and Ivonne, my grandfather Dario,

Don Fabio, PV and Comboni's friends.

my friends of Senigallia.

My friends in Kivuli and in Amani,

...and thanks to my Father.